DEUTSCHES ELEKTRONEN-SYNCHROTRON DESY

DESY 77/21
March 1977

Recent Experimental Results from DESY

by

D. Cords and G. Weber

NOTKESTRASSE 85 · 2 HAMBURG 52

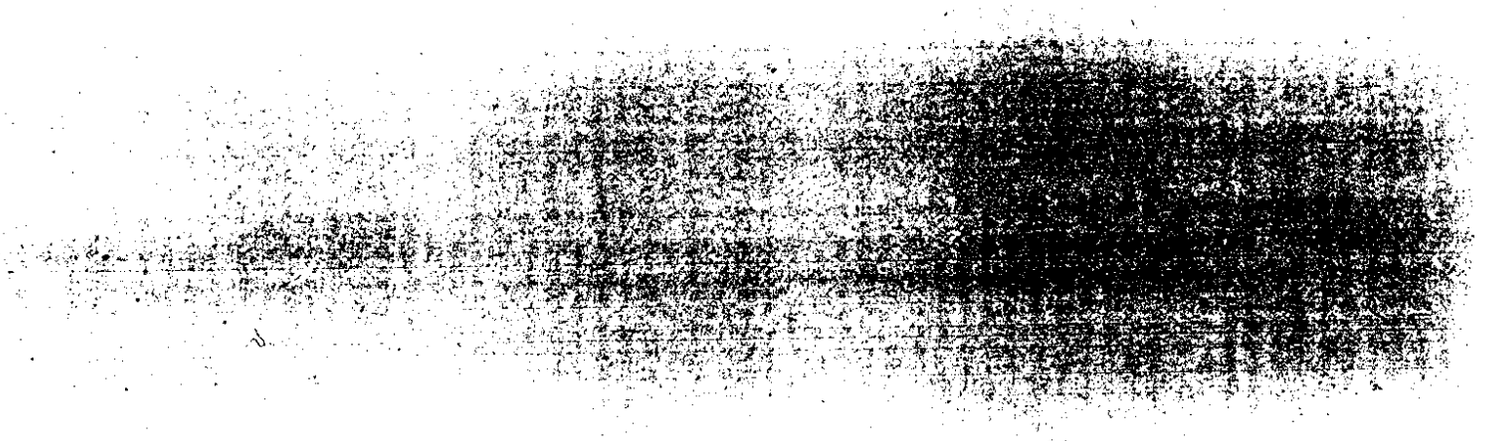

To be sure that your preprints are promptly included in the
HIGH ENERGY PHYSICS INDEX ,
send them to the following address (if possible by air mail) :

DESY
Bibliothek
Notkestraße 85
2 Hamburg 52
Germany

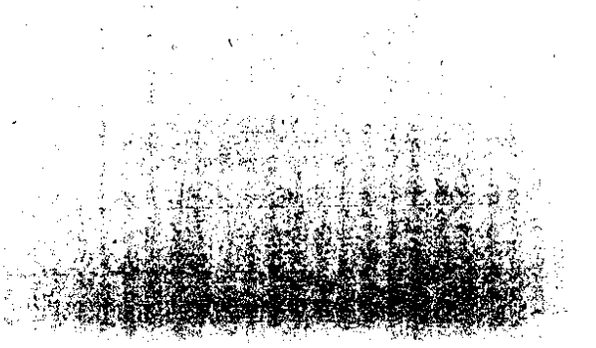

Recent Experimental Results from DESY

by D. Cords and G. Weber
Deutsches Elektronen-Synchrotron DESY, Hamburg

Recent Experimental Results from DESY

This report is based on a talk by G. Weber presented at a session of the Wissenschaftlicher Rat (Aug. 31, 1976) and on a series of lectures by D. Cords given at the 1976 Basko Polje International School of Elementary Particle Physics (Sept. 19 - Oct. 3, 1976). It includes a brief review of some recent results obtained at the DESY 7.5 GeV electron synchrotron and the e^+e^--storage ring DORIS. Although the report touches on results of other laboratories, it is by no means exhaustive. The reader interested in a complete review of the field of photon-hadron interactions is referred[1] to the Proceedings of the 1975 Lepton Photon Symposium at Stanford and to a recent report on e^+e^- physics by Wiik and Wolf.

The report is grouped into three parts. In part 1 the quantities used in part 2 and 3 are defined, and some general results recollected. No attempt is made to give an introduction to electromagnetic interaction theory, and it is assumed that the reader has some acquaintance with the field. Part 2 contains some recent experimental results on photo- and electroproduction from the 7.5 GeV electron synchrotron, and part 3 describes a number of results on particle production in e^+e^--annihilation obtained at DORIS.

1. Introduction

Photon and lepton induced reactions have proved very useful means of investigating elementary particles and their interactions. This is due to the rather weak coupling of the photon to other particles characterized by the elementary charge $e = \sqrt{\alpha} = \frac{1}{\sqrt{137}}$, and to the existence of a theory, namely quantum electro-dynamics (abbreviated in the following as QED), capable of describing processes involving photons and electric charges to any desired precision. Because of the smallness of the fine structure constant α the amplitude for any electromagnetic process is rather well approximated by the lowest order diagram alone[2].

Take for example the production of hadrons by inelastic scattering of electrons off the proton, the electroproduction process $e + p \to e' + X$. This process is well described by the one photon exchange diagram:

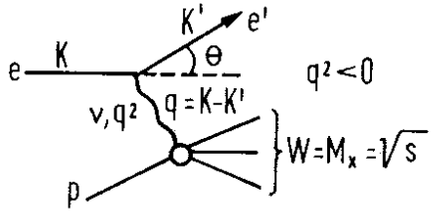

K, K' and p denote the four-momenta of the incident and scattered electron and the incident (target) proton and the metric is chosen such that for any two 4-vectors $a = (a_o, \vec{a})$ and $b = (b_o, \vec{b})$ the scalar product is given by $ab = a_o b_o - \vec{a}\vec{b}$. If the incident beam has the direction of the positive x-axis, these quantities are defined as follows:

$k = (E, E, 0, 0)$, since $K_x = \sqrt{E^2 - m_e^2} \simeq E$ for $m_e \ll E$

$p = (M, 0, 0, 0)$

$k' = (E', E' \cos\theta, 0, E' \sin\theta)$

$q^2 = -4E \cdot E' \cdot \sin^2 \frac{\theta}{2} = -Q^2$

$\nu = \frac{p \cdot q}{M} = E - E'$

$W^2 = (p + q)^2 = 2M\nu + M^2 + q^2$

The one-photon exchange diagram illustrates the above remark regarding the investigation of hadrons by using the known electromagnetic photon-lepton coupling. The kinematics of the incident and the scattered electron completely determine the properties (4-momentum, polarization) of the virtual photon. The virtual photon has a mass square $q^2 < 0$, i.e. is "space-like". The above electroproduction process may be looked at as the photoproduction process $\gamma_v + p \to$ hadrons with incident virtual photons ($q^2 < 0$) instead of real photons ($q^2 = 0$). Inelastic electron scattering experiments therefore may be used to study photoproduction processes as a function of the square of the mass of the photon.

Contrary to real photons the polarization vector of a virtual photon has both transverse and longitudinal components. The cross section is a sum of two terms[3] corresponding to photoproduction by transverse and by longitudinal photons:

$$\frac{d\sigma}{d\Omega\, dE'} = \Gamma(\sigma_T + \varepsilon \cdot \sigma_L) \qquad (1)$$

$\Gamma = \frac{e^2}{4\pi^2} \cdot \frac{(W^2 - M^2)\, E'}{Q^2 \cdot M \cdot E \cdot (1-\varepsilon)}$ = flux of incident transverse photons.

$\varepsilon = \left[1 + 2 \cdot \frac{\vec{q}^2}{Q^2} \cdot \mathrm{tg}^2 \frac{\theta}{2}\right]^{-1}$ = polarization parameter, giving the degree of linear transverse polarization of the virtual photon.

σ_T = total cross section for photoproduction by transverse photons.

σ_L = total cross section for photoproduction by longitudinal photons ($\Gamma\varepsilon$ being the flux of longitudinal photons).

σ_T and σ_L are both functions of q^2 and of W. To separate σ_T and σ_L, one needs to vary ε, i.e. to change the angle θ and the energies E and E' such as to keep q^2 and W fixed. Because of the strong dependence of ε on the angle, separation is difficult to achieve in practice. Some of the few examples where this has been achieved for particular reaction channels will be given in chapter 2.3.

Hadron production in e^+e^- annihilation is described by the following diagram:

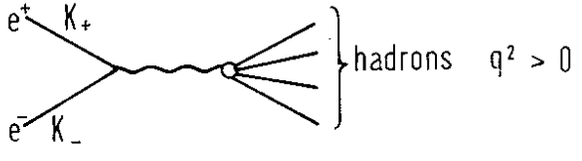

This diagram is obtained by rotating the space-like diagram such as to have the photon in the direction of the time axis. The photon has $q_o^2 > \vec{q}^2$, i.e. the square of its mass is $q^2 = (k_+ + k_-)^2 > 0$; it is "time-like".

If considered in the cms of e^+e^-, we have

$$q^2 = s = W^2 = 4E^2,$$

and the photon has no momentum, only energy. An important feature of hadron production via time-like photons is the fact that the quantum numbers of the final state must be equal to those of the intermediate photon, i.e. $J^{PC} = 1^{--}$. Compared to other reactions, where all angular momenta compatible with $J < \sqrt{s}/m_\pi$ may occur, this is a very useful simplification. We shall come back to this process in more detail in part 3.

2. Photo- and Electroproduction

The experimental program at the DESY synchrotron may be grouped into four categories[4], namely

- investigation of known and search for new vector mesons
- deep inelastic scattering
- electroproduction of η- and π-mesons in the resonance region
- photoproduction of π-mesons on polarized nucleons.

This report covers only some examples of experimental research in the first two categories and does not aim at a complete discussion of the experimental program. The third category is competently described in a recent report[5] by J. Gaylor. Although data on both inclusive and exclusive production of pions off polarized nucleons (fourth category) existed at the time of the school, the data analysis had not yet been finished.

2.1 Investigation of Known and Search for New Vector Mesons.

What is the interest in photoproduction of vector mesons? There is first of all the question of how many particles like the ρ, ω, Φ etc., all of which have the quantum numbers of the photon, exist. Already long before the discovery of the new J/ψ particles both experimental and theoretical

arguments called for more of these particles. Experimentally there was evidence [6),7)] for ρ' resonances at 1600 and 1250 MeV, and theoretically many models suggested the existence of particles similar to ρ, ω and φ at higher masses. The discovery of the new heavy particles [8),9)] has justified these speculations, but the large masses of the J/ψ and ψ' particles preclude investigating them at our synchrotron.

The most important reason for studying vector meson production is the phenomenon of vector dominance [10)], the ability of a high energy photon to undergo quantum fluctuations into a vector meson v, and therefore, in its interaction with a nucleon, to behave like a strongly interacting particle:

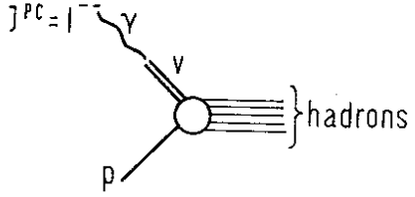

In this picture, photoproduction of a vector meson appears as the scattering of a virtual vector meson transforming into a real vector meson. Since at high energies hadron hadron scattering is known to be predominantly diffractive [11)], we expect photoproduction of vector mesons to be described by the following diagram:

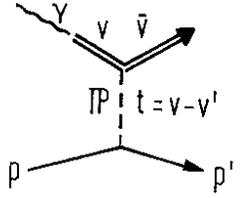

where $I\!P$ stands for the Pomeranchuk trajectory.

We can use the uncertainty principle to estimate [12)] at what distance Δx ahead of the proton the photon may convert into a vector meson: The transformation of the γ into a meson of mass m_V implies a violation of energy conservation by the amount

$$\Delta E = \sqrt{E_\gamma^2 + m_V^2} - E_\gamma \approx \frac{m_V^2}{2E_\gamma}$$

(assuming $E_\gamma \gg m_V$). This violation of energy conservation may last a time span Δt such as to satisfy $\Delta E \Delta t \leq 1$. (We are using units such that $\hbar = c = 1$). For the distance Δx at which the photon may convert we have:

$$\Delta x = c\Delta t \approx \frac{2E_\gamma}{m_V^2} .$$

For $E_\gamma \geq 7$ GeV and $m_V^2 = m_\rho^2$ this gives $\Delta x \geq 5$ fm. The same argument applied to a space-like photon of mass $-Q^2 > 0$ yields

$$\Delta E \geq \frac{m_V^2 + Q^2}{2\nu} \qquad (\nu = E - E' = E_\gamma)$$

and

$$\Delta x \leq \frac{2\nu}{m_V^2 + Q^2} . \qquad (2)$$

For $Q^2 = 1\ \mathrm{GeV}^2$, $m_V = m_\rho$ and $\nu = 7$ GeV, we would have $\Delta x \sim 1.8$ fm. As we would expect, it is "more difficult" for a space-like photon to transform into a vector meson than for a real photon.

a) Elastic and Inelastic Photoproduction of φ Mesons

$\gamma p \to \phi x \quad E_\gamma = 3 - 7$ GeV

The idea, that photoproduction of vector mesons is dominated by diffraction, is supported by the observation [7)] that the differential cross section $d\sigma/dt$ at high energies is roughly energy independent, has a peak at small t, and is well approximated by an exponential fall-off in t. This is a feature the above processes have in common with purely hadronic processes such as e.g. elastic pp, πp, Kp and pp scattering. [11)]

For both classes of reactions one has the difficulty of uniquely separating diffractive processes from competing processes. In the language of the Regge formalism [13)], the amplitude for a purely diffractive process would be described by the exchange of a single

trajectory, the so called Pomeranchuk trajectory, which carries the quantum numbers of the vacuum:

$$\alpha_{I\!P}(t) \approx 1 + \alpha'_{I\!P} \cdot t$$

It yields a differential cross section

$$\frac{d\sigma}{dt} \sim \beta^2(t) \cdot e^{2\alpha'_{I\!P} \cdot \ln\left(\frac{s}{s_o}\right) \cdot t} = e^{B \cdot t}$$

of approximately exponential t-dependence with a slope parameter B that increases with increasing energy ("shrinking of diffraction peak"):

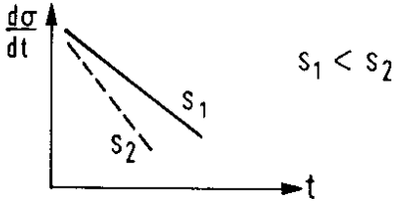

Experimentally the shrinking effect is difficult to observe for most of the reactions, because the trajectories corresponding to other particles can also contribute to the amplitude except at very high energies. Photoproduction of Φ-mesons is an exception in that respect. The reaction

$$\gamma\, p \to \Phi\, X \quad (\Phi \to K^+K^-)$$

should be a purely diffractive process even at rather low energies. This follows from vector dominance and the unique quark structure[13] of the Φ, namely $s\bar{s}$. If the incident photon transforms into $\Phi = s\bar{s}$, any non-zero quantum numbers for the t-channel exchange would involve exotic intermediate states. Therefore only Pomeron exchange (see page 7),

i.e. diffraction scattering, should be possible. Recent results from a DESY-Karlsruhe-Collaboration[14] on both elastic and inelastic production are in good agreement with this picture. This experiment is based on the detection of kaon pairs using a tagged photon beam (Fig. 2.1). For incident energies between 3 and 7 GeV and momentum transfers $|t| \leq 0.4$ GeV^2 (Fig. 2.2) they find $d\sigma/dt \approx \left(\frac{d\sigma}{dt}\right)_{t=0} \cdot \exp\{Bt\}$ with $B \approx 5.5$ GeV^{-2}. Fig. 2.3 shows the slope parameter as a function of s derived from the DESY-Karlsruhe data and from the results of other experiments on $\gamma\, p \to \Phi\, p$. A least square fit to these data yields a value for the derivative of the Pomeron trajectory $\alpha'_{I\!P} = 0.19 \pm 0.28$. Although the error is still too large as to exclude a definite statement about shrinkage, it is nevertheless interesting that it agrees with the value 0.278 ± 0.24 derived from high energy pp scattering[15]. Fig. 2.4 gives a comparison of the slope parameter B for the inclusive reaction $\gamma\, p \to \Phi\, X$ with the parameter for $K^+\, p \to K^+\, X$, a reaction[16] also expected to proceed via diffraction only. The good agreement between the B values found for the two reactions strongly supports the quark picture. Because of the strong decrease of B with the missing mass, the inelastic cross section at higher t-values exceeds the elastic cross section (Fig. 2.5).

b) Search for New Vector Mesons in Mass Range Between 1 and 2 GeV^2

This experiment is carried out by a DESY-Frascati-Collaboration[17]. It is based on the detection of electronpairs from the reaction:

$$\gamma\, p \to V\, X \quad (V \to e^+e^-)$$

The amplitude for pair production is a sum of the Bethe-Heitler-amplitudes and the compton amplitude:

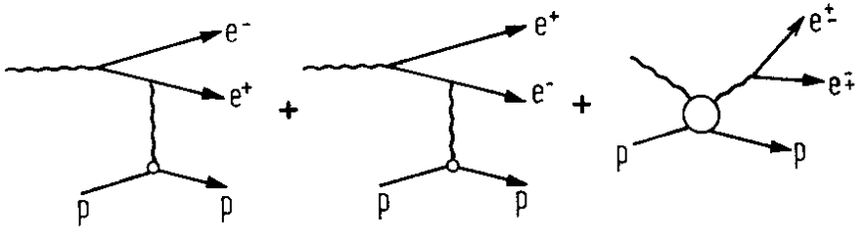

For large opening-angles the compton amplitude is usually small compared to the B.H.-amplitudes, but will become large if the mass of time-like photon, from which the pair is materialized, corresponds to the mass of a vector meson. In any case, the cross section is a sum of the B.H. cross section, the compton cross section and an interference term. When the B.H. amplitude is much larger than the compton amplitude, the compton cross section will be negligible, but the interference effect may still be visible. Since the e^+e^- final state is formed out of two gammas in the B.H. graphs and out of one photon in the compton graph, it has charge conjugation quantum number C = +1 in the first case, C = -1 in the second. The interference term therefore has C = -1 and is antisymmetric in the two leptons. It therefore vanishes for completely symmetric pairs. Using a symmetric set-up of finite angular acceptance one can obtain an invariant mass plot of the interference term alone, if each event is multiplied by the weight factor

$$\text{sign}\{|\vec{p}_+|\theta_+ - |\vec{p}_-|\theta_-\};$$

$\vec{p}_+$ and $\vec{p}_-$ are the three momenta of e^+ and e^- respectively, and θ_+ and θ_- the corresponding polar angles with respect to the photon direction.

Fig.2.6 shows a sketch of the experiment set-up. A bremsstrahlung beam produced by the 7.5 GeV electron synchrotron passes through a 1 m long liquid H_2 target. The electron and the positron are detected simultaneously by a two arm magnetic spectrometer, each pivoting independently about the target. Discrimination between electrons and other particles is provided by Cerenkov, shower and time-of-flight counters. Each spectrometer arm is adjusted to an average momentum of 2.7 GeV and an angle between 10^o and 20^o.

Since directions and momenta of the leptons are known, one can calculate the invariant mass of each e^+e^- pair:

$$M^2_{e^+e^-} = 2(E_+E_- - |\vec{p}_+||\vec{p}_-|\cos\theta_\pm) + 2m_e^2$$

where $\theta_\pm$ is the opening angle of the pair. Fig. 2.7 shows a plot of the invariant mass at an angle of 13^o. There are peaks corresponding to the known $\rho + \omega$ and Φ, superimposed on a rather large B.H.-background. Fig. 2.8 shows the mass plot for an angle of 15^o. Since the acceptance

no longer covers the $\rho + \omega$ region, only the Φ peak and the B.H.-background are visible. Fig. 2.9 shows the same plot for 16^o. The Φ peak is already smaller, and at 19^o (Fig. 2.10) the Φ peak has disappeared completely.

To find out whether there is an excess over the B.H.-background, one can look at the plots with the B.H.-background subtracted. This is seen in Fig. 2.11 for 13^o. Again one sees the peaks due to the $\rho + \omega$ and the Φ. Similar plots are obtained at the other angles, e.g. at 19^o (Fig. 2.12), no peak due to the Φ is visible, but the indication of an excess over B.H., which cannot be accounted for by the $\rho'(1600)$. To find out what goes on in the region above the Φ mass, let us look at the interference term.

Fig. 2.13 shows the interference term at 13^o. One can see the peaks due to the $\rho + \omega$ and Φ, the ρ peak having a rather long tail. There is an excess of events at masses between 1100 - 1700 MeV. At 15^o (Fig. 2.14) one still sees the Φ peak. The solid line always represents the contribution of the ρ, ω and Φ. The dotted line indicates a possible contribution from the $\rho'(1600)$. The data points are not reproduced by this ρ' peak. In addition, there is an indication of a peak near 1100 MeV. At 16^o (Fig. 2.15) the pattern is similar, except that the Φ peak is already much weaker. There is still a spike near 1100 and an excess over the ρ' curve at higher masses. Fig. 2.16 shows the same plot at 19^o. The structure at 1100 MeV is no longer visible, but there still seems to be an excess of events at the higher masses.

The authors conclude that they have indications of a resonance-like structure at a mass of 1100 MeV and with a width consistent with the experimental resolution (~20 MeV). They also conclude that there is evidence for additional structures at higher masses. The dash-dotted curve called "exercise" assumes, in addition to the 1100 MeV peak, four more resonances[17]. Assuming a slope parameter of 6 GeV^{-2}, they find a value for the branching ratio times the cross section of 4.9×10^{-5} $\mu b \cdot GeV^{-2}$, which is comparable with the ρ' value[18] and roughly a factor 100 below the one for the ρ.

Evidently this experiment needs more statistics and therefore it has been assigned a lot of additional running time. It will probably take a year, perhaps longer, before one can definitely tell whether there is a long lived vector meson at 1100 MeV, and whether there are more states between 1300 and 1700 MeV. There have been speculations by Pati and Salam[19] that the structure at 1100 MeV could be a vector gluon, others have suggested an excited state of the Φ meson. Irrespective of these specific models, there is little doubt, that the discovery of a long lived vector meson at 1100 MeV would have quite an impact on hadron spectroscopy.

2.2 Deep Inelastic Electron Scattering

The interest in this field is due to the fact that for $Q^2 >> M^2$ and $W>>M$ the cross section given by Eq.(1) on page 5 for inelastic scattering of electrons on protons shows much less dependence on Q^2 than the elastic scattering cross section[20]. This is usually expressed as "approximate Bjorken scaling" of the structure functions[21]. In terms of σ_L and σ_T the structure functions are defined as follows:

$$W_1 = \frac{W^2 - M^2}{8\pi^2 M}\,\sigma_T$$

$$(1 + \frac{\nu}{Q^2})W_2 - W_1 = \frac{W^2 - M^2}{8\pi^2 M}\,\sigma_L$$

The postulate of Bjorken was, that in the limit $M_x \to \infty, Q^2 \to \infty$ the quantities νW_2 and W_1 should no longer depend on Q^2 and W separately, but only on the "scaling" variable $x = \frac{Q^2}{2M\nu}$. Experimentally this has been found to be approximately true, even at relatively low values of M_x and Q^2, i.e. for M_x slightly above the resonance region, and $Q^2 > 1\ GeV^2$. This fact enables one to investigate questions connected with scaling at accelerators of relatively small maximum energy, such as the DESY synchrotron (E < 7.5 GeV). What do we want to investigate? There is first of all the behaviour of the individual channels. Does the cross section for a particular reaction behave in the same way as the total cross section or differently? Does the ratio $R = \sigma_L/\sigma_T$ approach zero as Q^2 becomes large or does it remain finite[22]? Is there a smooth transition from photo- to electroproduction or is there a discontinuity at small Q^2 values, as some data [6)23)] seem to indicate? To investigate particular reaction channels, it is important, to detect the final state hadrons in coincidence with the scattered electron. An electron synchrotron such as the DESY machine with its large duty cycle (~ 10%) is very well suited for this kind of experiments.

a) Electroproduction of Charged Pions

$e\,p \to e'\,\pi^+\,n$	$W = 2.19$ GeV
$e\,n \to e'\,\pi^-\,p$	$Q^2 \leq 1.35\ GeV^2$
	$\lvert t\rvert \leq 1$ GeV

These two reactions[24)25)] were studied by a joint group of DESY and the University of Hamburg. The aim was to investigate the behaviour of the cross sections over a rather large range of Q^2, including the transition region $Q^2 \sim 0$ from photo- to electroproduction. Another aim was to separate the contributions to the cross section from different polarization states of the virtual photon. If p_π denotes the four-momentum of the produced pion, the cross section is studied as a function of $t = (q-p_\pi)^2$, Q^2, W and ε (see (1)):

$$\frac{d^4\sigma}{dQ^2\,dW^2\,dt\,d\Phi} = \Gamma\,2\pi\,\frac{d^2\sigma}{dt d\Phi} \qquad (3)$$

$$2\pi\,\frac{d^2\sigma}{dt\,d\Phi} = \frac{d\sigma_U}{dt} + \varepsilon\,\frac{d\sigma_L}{dt} + \varepsilon\cos 2\Phi\,\frac{d\sigma_p}{dt} + \sqrt{2\varepsilon(\varepsilon+1)}\,\cos\Phi\,\frac{d\sigma_I}{dt}$$

$\frac{d\sigma_U}{dt} = \frac{1}{2}\left(\frac{d\sigma_{//}}{dt} + \frac{d\sigma_\perp}{dt}\right)$ = unpolarized transverse cross section

$\frac{d\sigma_L}{dt}$ = longitudinal cross section

$\frac{d\sigma_P}{dt} = \frac{1}{2}\left(\frac{d\sigma_{II}}{dt} - \frac{d\sigma_{\perp}}{dt}\right)$ = polarized transverse cross section

$\frac{d\sigma_I}{dt}$ = interference cross section

All terms are functions of Q^2, W and $t = (q - p_\pi)^2$. Γ and ε are the same as in (1).

We start with π^+ production:

$\gamma_v p \to \pi^+ n$

Fig. 2.17 shows the experimental arrangement[24]. An external beam from DESY is focussed on to a 10 cm long target cell, which is either filled with liquid H_2 or with D_2, depending on whether one wants to study pion production on protons alone or on both protons and neutrons. The beam intensity was measured using a secondary emission monitor and a Faraday cup downstream of the target. The scattered electrons and the produced pions were detected in coincidence using two magnetic spectrometers. Each spectrometer consists out of 3 quadrupole magnets, followed by a vertically deflecting bending magnet and 4 multiwire proportional chambers. Particle identification is provided by time-of-flight, shower and Cerenkov counter techniques.

The $(\pi^+ n)$-channel was separated from other final states by a cut in the missing mass spectrum. Fig. 2.18 shows the missing mass spectrum for π^+ production on protons. M_x is the calculated invariant mass of the undetected particles. The neutron peak which has a width of about 50 MeV, is very well separated from the continuum. Fig. 2.19 shows the measured t-distributions of the cross section for four different values of Q^2. The shaded areas indicate photoproduction data[26]. There are three striking observations:

α) The low Q^2 data merge with the photoproduction results.

β) At $Q^2 = 0.28$ and 0.7 GeV^2 and small $|t|$, the electroproduction data are above the photoproduction cross sections, indicating large longitudinal contributions from one-pion-exchange. For $|t|$ larger than about 0.2 the electroproduction points are below the photoproduction results.

γ) This difference between photo- and electroproduction does not persist in the large $|t|$ region. For $|t| \geq 0.8$ GeV^2 all points are compatible with the photoproduction values. Within the errors the cross section in that region does not seem to depend on Q^2.

For the $(\pi^+ n)$-channel there are data at large Q^2 and $|t|$ from the Cornell-Harvard group[27]. To put them on the same graph (Fig. 2.20), the Cornell-Harvard data were scaled in energy ($\sim (s - M^2)^{-2}$) to two central values ($s = 4.8$ and 7.5 GeV^2) and converted from $\frac{d\sigma}{d\Omega}$ to $\frac{d\sigma}{dt}$. At the lower energy the data of the two experiments fit very well together. The striking feature is that for $|t| > 0.2$ GeV^2 and $Q^2 > 0.7$ GeV^2 the cross section is roughly independent of Q^2. Qualitatively the same behaviour is shown at the higher energy by the Cornell-Harvard data[27] alone. The shaded areas indicate photoproduction. The elliptical areas correspond to backward pion photoproduction. (In comparing photo- and electroproduction at large $|t|$ one must keep in mind that the position of the backward (u-channel) peak depends on Q^2, because $|t|_{max}$ increases with Q^2. The higher photoproduction cross section in that region is probably due to this kinematic effect).

Integrating the cross section over t, one finds, that the cross section for π^+ production for $Q^2 > 0.7$ GeV^2 has a Q^2 dependence roughly equal to that of the total cross section for virtual photons on the proton:

$$\sigma_{\gamma_v p \to \pi^+ n}(Q^2)/\sigma_{\gamma_v p \to X}(Q^2) \sim \text{const.}$$

For $Q^2 = 0.7$ GeV^2 and $Q^2 = 1.35$ GeV^2 separation of the Φ-dependent terms of the cross section was carried out with the result shown in Fig. 2.21. The important features are:

α) The interference term between longitudinal and transverse amplitudes is consistent with zero.

β) $\sigma_U + \varepsilon\sigma_L$ strongly decreases with t, indicating the contribution of the longitudinal part to decrease rapidly with t.

γ) σ_P is negative, indicating that $\sigma_\perp$ is larger than $\sigma_{//}$.

To separate $\frac{d\sigma_U}{dt}$ and $\frac{d\sigma_L}{dt}$, measurements for different values of ε are required. Data for different values of ε exist already, but the analysis is not yet finished. It is nevertheless possible to derive an upper bound for $\frac{d\sigma_L}{dt}$, using the results obtained for $\frac{d\sigma_U}{dt} + \varepsilon \frac{d\sigma_L}{dt}$ and for $\frac{d\sigma_P}{dt}$. For $|t| > 0.3$ one finds $\frac{d\sigma_L}{dt} < \frac{d\sigma_\perp}{dt}$.

Next let us look at the results[25] for π^- production:

$\gamma_v n \to \pi^- p$

Using the same technique as described above, π^- and π^+ production of neutrons and protons bound in deuterium was studied at $Q^2 = 0.7$ GeV^2 and $Q^2 = 1.35$ GeV^2 and for $|t| \leq 1.0$ GeV^2. The spectator model assumes high energy electron-deuteron scattering to take place at one of the nucleons in the deuteron, while the other one acts as a spectator. Corrections due to nuclear binding and to radiative effects should largely cancel in the ratio of π^- and π^+ production in deuterium and the cross section ratio should in fact measure the cross section ratio on the free neutron and proton:

$$\frac{d\sigma(ed \to e'\pi^- pp)}{d\sigma(ed \to e'\pi^+ nn)} = \frac{d\sigma(ed \to e'\pi^- p)}{d\sigma(ep \to e'\pi^+ n)}$$

Using the proton cross section measurement[24] just described the cross section on the free neutron is calculated from the above ratio:

$$\frac{d\sigma}{dt\, d\Phi}(en \to e'\pi^- p) = \frac{d\sigma(ed \to e'\pi^- pp)}{d\sigma(ed \to e'\pi^+ nn)} \cdot \frac{d\sigma}{dt\, d\Phi}(ep \to e'\pi^+ n) \qquad (4)$$

The π^+ and π^- mesons were measured in coincidence with the scattered electron and again a cut was applied in the missing mass spectrum. As shown in Fig. 2.22 the missing mass peaks of the nucleons are somewhat

wider than in the case of the free proton because of the Fermi motion. Nevertheless, the nucleon is well separable from the continuum.

The measured ratios of the cross sections from deuterium are shown in Fig. 2.23 for $Q^2 = 0.70$ GeV^2 and $Q^2 = 1.35$. There are two important points to notice: α) for $|t|$-values up to 0.1 GeV^2 the ratio is consistent with unity, as expected from gauge invariance, β) the simple quark model[21] predicts R to remain above 0.25 for all values t. The data are consistent with this limit within the errors. The neutron cross sections calculated from the data are shown in Fig. 2.24. For small $|t|$ and $Q^2 = 0.7$ GeV^2 the electroproduction cross section exceeds the photoproduction values, again indicating the strong contribution of longitudinal terms. From $t = 0.3$ GeV^2 on upwards the electroproduction cross section is smaller than the photoproduction cross sections, but the difference is smaller than in the case of the proton. Fig. 2.25 shows the decomposition of the cross section into its different terms. The result is quite similar to that obtained for π^+ production on the proton:

α) $\sigma_U + \varepsilon\sigma_L$ decreases rapidly with t.

β) σ_I is compatible with zero.

γ) σ_P tends to be negative at both values of Q^2, although it is consistent with zero at $Q^2 = 1.35$ GeV^2 implying $\sigma_\perp > \sigma_{//}$ at $Q^2 = 0.7$ GeV and $\sigma_\perp \approx \sigma_{//}$ at $Q^2 = 1.35$ GeV^2.

Summarizing the results on charged pion electron production we find:

i) Low Q^2 date merge with photoproduction results.

ii) $\frac{d\sigma}{dt}$ independent of Q^2 for $|t| > 0.2$ GeV^2 and $Q^2 > 0.7$ GeV^2.

iii) $\frac{\sigma_{\gamma_v p \to \pi^+ n}(Q^2)}{\sigma_{\gamma_v p \to x}(Q^2)}$ const. for $Q^2 > 0.7$ GeV^2.

iv) $\frac{d\sigma_I}{dt}$ and $\frac{d\sigma_P}{dt}$ small,

v) $\frac{d\sigma_U}{dt} + \varepsilon \frac{d\sigma_L}{dt}$ decreases rapidly with increasing $|t|$.

vi) $R = \frac{d\sigma(\gamma_v n \to \pi^- p)}{d\sigma(\gamma_v p \to \pi^+ n)} \geq 1/4$ in agreement with quark model.

b) Inclusive Production of Protons

$$\gamma_v p \to px$$

The reaction ep → e'px was studied at c.m. energies of the final hadrons between 2.0 and 2.8 GeV for Q^2 between 0.08 and 0.64 GeV^2 by a DESY-Marburg-Wuppertal collaboration[28]. The experimental set-up used is shown in Fig. 2.26. It uses two large solid angle deflection magnets, backed by optical spark chambers to measure directions and momenta, and time-of-flight, Cerenkov and shower counters to measure the scattered electrons and the forward hadrons in coincidence. Some preliminary results of this experiment have been reported at the Bonn Conference[29] in 1973. In the meantime the number of events has been increased by a factor of more than 50.

The results are expressed in terms of the invariant cross section, devided by the total cross section σ for photoproduction by virtual photons.

$$\frac{E_p}{\sigma_{tot}} \frac{d^3\sigma}{d^3\vec{p}} = f$$

E_p is the energy of outgoing proton, $\vec{p}$ its 3-momentum. f is studied as a function of Q^2, W, Φ, $p_\perp^2$, x_F. $p_\perp^2$ is the square of the transverse momentum of the outgoing proton. $x = p^*_{//}/p^*_{max}$ is Feynman's longitudinal variable, $p^*_{//}$ being the longitudinal momentum of the outgoing proton, p^*_{max} its maximum momentum for a given W; both momenta refer to the cms of the target proton and the photon. The indices for "parallel" and "transverse" refer to the direction of the virtual photon.

As in exclusive electroproduction, the cross section is split into the contributions of different photon polarizations. Fig. 2.27 shows the ratio $f_I/(f_U+\varepsilon f_L)$ for two different values of W and for four values of Q^2, where the indices U, L, I and P have the same meaning as in formula (3). In the whole range covered this ratio is zero within the errors. The same

is true for $f_P/(f_U + \varepsilon f_L)$ as shown in Fig. 2.28. So we see that both f_I and f_P are at least an order of magnitude smaller than $f_U + \varepsilon f_L$. Therefore the Φ dependence of f will be neglected in the further discussion. The x dependence of f for different values of Q^2 at W = 2.62 GeV is shown in Fig. 2.29. The solid curves represent Q^2 independent distributions $\exp\{a + bx + cx^2\}$. The data are rather well approximated by these curves. The same is true for the data from the purely hadronic process[30] $\pi^- p \to pX$. Similar results have been found at three other values of W. The outstanding feature of these data is that the cross section decreases by roughly an order of magnitude in going form x = 0 to x = 1.

The dependence on the square of the transverse momentum for W = 2.62 GeV is shown in Fig. 2.30. The cross section decreases with increasing $p_\perp^2$. The data are rather well represented by $A \cdot \exp(a\, p_\perp^2)$. No systematic dependence of the slope parameter a on Q^2 is visible. Fig. 2.31 shows the slope parameter a, averaged over Q^2 as a function of x. One observes a monotonous decrease of |a| as x increases. There is some similarity with the results obtained in electroproduction of π^- at comparable energies[31], and with the hadronic reactions $\pi^\pm p \to \pi^\pm X$ at higher values[32] of W. A smaller decrease of |a| with x was observed[33] in the photoproduction reaction $\gamma p \to pX$ at W = 3.5 GeV. In comparing the results of this and the present experiment, one must, however, keep in mind, that different portions of the $p_\perp^2$-distributions were used to derive a.

The W-dependence of the invariant cross section was studied at different Q^2-values. For all values of x, there is a monotonous decrease with W. For $Q^2 = 0.31$ GeV^2 this is shown in Fig. 2.32. The W-dependence may be expressed as $B \cdot (W^2 - M_p^2)^{-b}$, as shown by the solid curves. The exponent b does not show any Q^2 dependence, but it strongly depends on x, as shown in Fig. 2.33. There is good agreement with the results of Bebek et al[34]. The results[32] of an inclusive $\pi^+ p$ scattering experiment, exhibiting an x-dependence of b similar to the one of the electroproduction data are also shown. On the other hand photoproduction results[33] at 2.62 and 3.5 GeV yield $b \simeq 1.5$ independent of x.

Having studied the dependence of f on x, $p_\perp^2$ and W, how about the Q^2 dependence? Since f is the ratio of the differential to the total cross section and this ratio has been found to be roughly Q^2 independent in the case of an exclusive channel, we would expect f to show rather little Q^2 dependence. Fig. 2.34 shows the results for W = 2.62. There is indeed very little dependence on Q^2, and similar results are found at the other energies, except for W = 2.09, where some dependence on Q^2 is indicated, probably due to the proximity to the resonance region.

Summarizing the results on proton inclusive production we find:

i) f_p and $f_I \ll f_U + \varepsilon f_L$, i.e. the Φ dependence is negligible.

ii) f decreases rapidly with increasing x.

iii) The dependence on the transverse momentum is given by $A \cdot \exp(a\, p_\perp^2)$ with $|a|$ a decreasing function of x.

iv) The energy dependence is given by $B \cdot (W^2 - M_p^2)^{-b}$, where b increases proportional to x.

v) No significant dependence of f on Q^2 is observed (except at W = 2.09 GeV).

c) Rho Production by Virtual Photons

$\gamma_v p \to \rho^o p$ $\quad W = 1.3 - 2.0$ GeV, $Q^2 = 0.3 - 1.4$ GeV^2

This reaction we could have discussed in the previous chapter 2.1 on photoproduction of vector mesons. On the other it gets contributions from both longitudinal and transverse photons and therefore also fits into this chapter. The experimental results we report have been obtained in an experiment on electroproduction of multiparticle final states using a streamer chamber[35]. In fact, ρ^o electroproduction is only one of the channels that contribute to the reaction $\gamma_v p \to p\pi^+\pi^o$, though the most important one for W > 2 GeV. For smaller values of W the channel $\gamma_v p \to \Delta^{++}\pi^-$ appears to be the dominant one. The latter process has been used[36] to derive the axial transition form factor of the nucleon to the Δ resonance $G_A(q^2)$, a quantity we do

not expect to differ drastically from the elastic axial form factor of the nucleon $G_A(q^2)$. Although limitation of time did not permit this subject to be included in the lectures, it is worth pointing out that the results of this experiment fit very well with those derived for $G_A(q^2)$ from the reaction $\gamma_v p \to \pi^+ n$ near threshold[37]. Assuming a dipole dependence on q^2, the mass values in G_A derived from the electroproduction experiments agree very well among each other (Fig. 2.35), but are somewhat higher than those found in the neutrino experiment[38].

Turning to electroproduction of ρ-mesons, we recall that photoproduction of ρ mesons shows the characteristics of a diffraction process: For W > 2 GeV the cross section is roughly energy independent, has a t-dependence given by $\exp\{At\}$ with A = 6-8 GeV^{-2} and is dominated by natural parity exchange[39]. We are interested in knowing to what extend this is also true for ρ production by space-like photons. According to the vector dominance model[10] we expect the cross section to drop with increasing Q^2 like $\sim[Q^2 + m_\rho^2]^{-2}$. In addition, there will be modifications of the cross sections due to changes in the kinematics such as the variation of the minimum momentum transfer $t_{min}(Q^2)$ to the nucleon, a possible t dependence of the slope parameter $A = A(Q^2)$, and variable contributions from longitudinal photons (parametrized in the following as $\varepsilon \cdot \xi^2\, Q^2/m_\rho^2$, where ξ^2 is an empirical parameter). Vector dominance[10] predicts the following behaviour of the cross section with Q^2 and W:

$$\sigma_{\gamma_v p \to \rho^o p}(Q^2,W)/\sigma_{\gamma p \to \rho^o p}(Q^2 = 0,W) = \tag{5}$$

$$= \frac{(W^2-M^2)\cdot\{1+\varepsilon\,\xi^2\,\frac{Q^2}{m_\rho^2}\}}{\{(W^2-M^2-Q^2)^2+4W^2Q^2\}^{1/2}}\ \exp\{A(Q^2)t_{min}(Q^2)-A(0)t_{min}(0)\}\{\frac{m_\rho^2}{m_\rho^2+Q^2}\}$$

To make a comparison of the data with this formula, one has to separate the ρ^o production channel from other processes contributing to $\gamma_v p \to \pi^+\pi^- p$.

Fig. 2.36 shows the $M_{p\pi^+}$, $M_{\pi^+\pi^-}$ and $M_{p\pi^-}$ mass distributions for $2.0 < W < 2.2$ GeV for the reaction $\gamma_v p \to \pi^+\pi^- p$. The ρ production channel

is seen to dominate the reaction. The ρ-signal gets even stronger when small momentum transfer events are selected, indicating that ρ production predominantly proceeds via diffraction. Fig. 2.37 shows the ρ production cross section as a function of W for different intervals of Q^2. The electroproduction cross section is seen to be quite similar to the photoproduction cross section[40] (open circles): A sharp rise above threshold, a maximum near 1.9 GeV and very little energy dependence above 2.2 GeV. The Q^2 dependence of the cross section is shown in Fig. 2.38 for different values of W. There is good agreement with the vector dominance prediction(5) represented by the solid curves. The dominating feature, the strong decrease of the cross section with increasing Q^2, is due to the square of the ρ propagator $[m_\rho^2 + Q^2]^{-2}$.

For W > 2 GeV the angular distributions of ρ's with respect to the direction of the photons indicate the process to be predominantly peripheral (a strong peak in the forward direction superimposed on a flat background). The peripheral part of the cross section as a function of t is shown in Fig. 2.39 for W > 2.2 GeV. For comparison existing photoproduction results[41] are also shown. The slope parameter A derived from these results is shown as a function of Q^2 in Fig. 2.40a. There is a good agreement with the photoproduction result $A = 6.5 \pm 0.3$ GeV^{-2}. In an optical model one would interpret the slope parameter[12] as the square of the interaction radii $A_{\rho p} = \frac{1}{4}(R_\gamma^2 + R_p^2)$. According to our introductory remarks on vector dominance (see (2)) we would expect $R_\gamma \simeq \Delta x$ to decrease with Q^2. In the limit of very large Q^2 we would get $R_\gamma = 0$, i.e. $A_{\rho p} = \frac{1}{4} R_p^2 = \frac{1}{2} A_{pp} \approx 3.5$ GeV^{-2}. The present data do not give an indication of "shrinking of the photon" for $Q^2 \leq 1$ GeV^2 and W ≈ 2.5 GeV. Fig. 2.40b shows the slope parameters for longitudinal and transverse ρ mesons separately. Separation of the longitudinal and the transverse polarized rhos is possible, because the decay angular distribution of the ρ can be used as an analyzer of the spin of the ρ. For a detailed account of these techniques of analysis, we refer to the original paper[35]. Fig. 2.40b shows that there is no statistically significant difference in the slope parameters for the transverse and the longitudinal ρ's. Further results derived from the

decay angular distributions of the ρ we quote without going into the details:

α) For $0.3 < Q^2 < 1.4$ GeV^2 and $2.2 < W < 2.8$ GeV natural parity exchange dominates the production of ρ's by transverse photons as expected for a diffractive process.

β) In the above energy range the helicity flip amplitudes are at most of the order of 15 - 20% of the non-flip amplitudes for $|t| < 0.5$ GeV^2, i.e. electroproduction of ρ's obeys s-channel helicity conservation (SCHC).

γ) Assuming SCHC, longitudinal rhos are produced by longitudinal photons only and transverse rhos by transverse photons. The ratio $R = \sigma_L/\sigma_T$ of the cross sections as derived from the density matrix is shown in diagrams a) and b) of Fig. 2.41 for different values of energy as a function of Q^2. R is seen to rise linearly with Q^2 for W > 2 GeV (for W ≦ 2 GeV the R values shown must be regarded with caution, since SCHC might not be valid in that range). The dashed line in diagram b) gives R for the total electroproduction cross section, showing the longitudinal part to be more important in ρ production than in the average for other processes. Diagram c) indicates that the data are well represented by $R = \xi^2 \frac{Q^2}{m_\rho^2}$ as used in (5) with $\xi^2 \approx 0.5$ for W > 2 GeV.

δ) Another quantity derived from the density matrix assuming SCHC and natural parity exchange is the phase δ between the longitudinal and transverse amplitudes (Fig. 2.42). At W ≤ 2 GeV the two amplitudes are roughly 90° out of phase, but with increasing energy the phase difference becomes smaller.
This is in agreement with the expectation that both amplitudes should become diffractive at high energies.

Summarizing the results on electroproduction of ρ's we have

i) For W > 2 GeV rho production is predominantly peripheral.

ii) The peripheral part of the rho production cross section drops rapidly with increasing Q^2 as predicted by the vector dominance model.

iii) The slope parameter of dσ/dt at $Q^2 = 0.4$ and 0.8 GeV^2 agrees within errors with the photoproduction value. There is no indication of "photon shrinkage".

iv) Production of transversely polarized ρ mesons proceeds via natural parity exchange.

v) Rho production approximately preserves s-channel helicity.

vi) $R = \sigma_L/\sigma_T$ is a linear function of Q^2.

vii) The phase δ between the longitudinal and transverse amplitudes decreases monotoneously with increasing W consistent with the diffraction picture for which both amplitudes should become purely imaginary.

d) Shadowing in Inelastic Electron Scattering on ^{12}C and ^{27}Al

The high energy photon-nucleon cross section is ~120 nb. In the absence of vector dominance, this would correspond to an absorption length of the photon in nuclei of about 500 fm, i.e. a nuclear mean free path much larger than the nucleus. In that case the total gamma-nucleus cross section would be proportional to the mass number A and the cross section for Compton scattering in the forward direction would be proportional to A^2. For real high energy photons a slower rise of the cross section with A has been observed[45]. This is shown in Fig. 2.43 which gives a comparison[46] of total photon nucleus cross sections derived from various experiments with a cross section behaviour proportional to A. The data are consistently below the dashed line. This effect, called shadowing, is due to the coupling of the photon to the strongly interacting vector mesons with their short nuclear free paths (see first diagram on page 7). For virtual photons of a given energy, shadowing is expected to become weaker with increasing Q^2. Experimentally the situation is less clear than in the case of real photons. A group of physicists of Bonn, Karlsruhe and DESY[47] has investigated this effect in ^{12}C and ^{27}Al. Fig. 2.44 shows the ratio $\sigma(\gamma_v A)/(\sigma(\gamma_v N)\cdot A) \equiv A_{eff}/A$ for ^{27}Al as a function of $x = Q^2/2M\nu$. The diagram also shows the results of the SLAC group[49]. The ratio is clearly below unity. The same is found for ^{12}C. Although their result seems to imply positive evidence for shadowing in both nuclei, a quantitative interpretation of such measurements depends on a precise knowledge of the radiative corrections, which are very difficult to calculate for complex nuclei.

Fig.2.45 shows the ratio A_{eff}/A derived for ^{12}C as a function of the proton energy, with the radiative corrections calculated in three different ways. The results are quite different in each case, and the radiative corrections are obviously a serious problem. To tackle this problem, the group proposes to measure the effect in ^{28}Si, a nucleus quite similar in size to ^{27}Al, but with a different proton content. They also want to study the cross section for small Q^2 in ^{9}Be for comparison with existing real photon results.

e) Electron and Muon Induced Reactions at Higher Values of Q^2 and W

The maximum energy of the DESY synchrotron of 7.5 GeV precludes the extension of electroproduction measurements to values higher than W ~ 3 GeV and Q^2 ~ 3 GeV^2, although, the extensions of the measurements into the truly deep inelastic region is extremely desirable. For this reason physicists at DESY have proposed experiments at other accelerators, namely at the 12 GeV electron synchrotron at Cornell, and at the SPS at CERN. The DESY-Cornell experiment uses a DESY streamer chamber to assure full detection of complicated multiparticle states. About 100 000 good events have been collected during the first two runs in spring and autumn 1976, but the data analysis, which is largely carried out at DESY, is not yet finished. Another run is planned for early next year in order to bring the total number of events up to $1.5 \cdot 10^5$.

The European Muon Collaboration, which includes physicists from France, Italy, the United Kingdom, CERN, DESY and the German Universities, wants to test scaling in deep inelastic scattering at cm energies up to 20 GeV and $Q^2 \leq 150$ GeV^2. They also plan a systematic study of multiparticle production, including multimuonproduction. This experiment, which will use muon beams at least 10 times more intensive than those available at NAL, will probably start in the spring of 1978.

3. Particle Production in e^+e^- Annihilation

This chapter is divided into five parts. We discuss some of the fundamental properties of e^+e^- annihilation (part 1), present the basic parameters of the storage ring DORIS (part 2), and introduce the three detectors (part 3) which so far have yielded physics results at DORIS. The results on the properties of the J/ψ and ψ' particles and the investigation of charm states are reported in detail in part 4. The complementary information on results from SPEAR is contained in a parallel series of Basko Polje lectures[51] by F. Pierre. Finally, in part 5 we present some future prospects with the next-generation storage ring PETRA.

3.1 e^+e^- Annihilation Physics

After having introduced the basic idea of one photon exchange in chapter 1, let us now discuss some of the characteristics of e^+e^- annihilation.

a) Electromagnetic Processes

The cross sections for electromagnetic processes of leptons can be calculated from the well established theory[2] of quantum electrodynamics (QED). The simplest process for e^+e^- collisions is muon pair production. Its integrated cross section is given by:

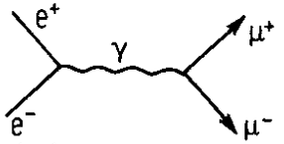

$$\sigma_{\mu\mu} = \frac{\pi}{3}\frac{\alpha^2}{E^2} = \frac{22\text{nb}}{E^2}\,, \quad \alpha = \frac{e^2}{\hbar c} = \frac{1}{137}$$

where the beam energy E is given in GeV and $1\text{nb} = 10^{-33}\ \text{cm}^2$.

For elastic electron-positron scattering (Bhabha scattering) one has in addition to the time-like diagram a space-like contribution:

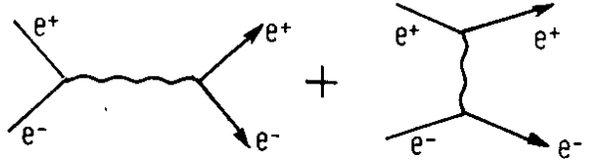

Since the cross section is large for forward scattering and QED is a safe theory in this region, small angle Bhabha scattering is taken for luminosity measurements, i.e. all measured e^+e^- event rates are referred to the e^+e^- elastic cross section.

A QED process of the same order of magnitude as Bhabha scattering is the annihilation into two photons:

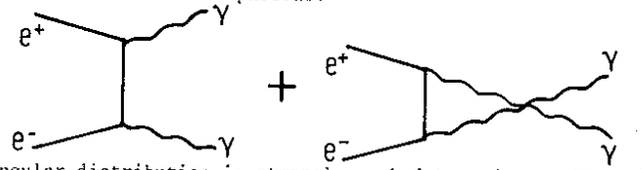

Its angular distribution is strongly peaked towards the directions of the incident leptons.

b) Hadron Production

We shall consider here hadron production via one photon annihilation and neglect higher order terms[52].

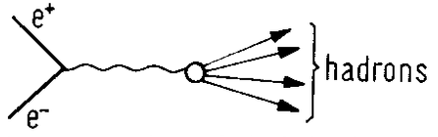

If conserved, the quantum numbers of the hadronic system should be those of the photon. Therefore, spin-parity and C-parity are given by $J^{PC} = 1^{--}$ and one can ask: Which consequences do arise for the cross section and the angular distribution?

Due to $J^P = 1^-$ the orbital angular momenta of the e^+e^- system are limited to L = 0 and 2. Using the classical definition $L = p \cdot r \simeq E \cdot r$, where $p \simeq E$ is the electron momentum (energy) and r the interaction radius, one obtains $r \sim \frac{1}{E}$ since L is limited. Inserting this and the electromagnetic coupling α into the geometrial cross section $\sigma = \pi r^2$ and remembering the above μ-pair cross section, one has for the total hadronic cross section

$$\sigma(e^+e^- \to \text{hadrons}) \sim \alpha^2 \pi r^2 = \frac{\alpha^2\pi}{E^2} = R \cdot \sigma_{\mu\mu}$$

Therefore it is expected that the hadronic cross section decreases as $1/E^2$. This is in strong contrast with purely hadronic interactions where the cross section becomes constant or even increases at high

energies because higher and higher partial waves can contribute to hadron collisions[13].

Another characteristic of hadron scattering is the strongly forward peaked angular distribution of the final state particles. The hadrons from e^+e^- collisions, on the other hand, have a relatively flat angular distribution. Since the total angular momentum is limited to one, the most general angular distribution for the inclusive hadron production process $e^+e^- \to h + X$ is

$$\frac{d\sigma_h}{d\cos\theta} = a + b\cos^2\theta$$

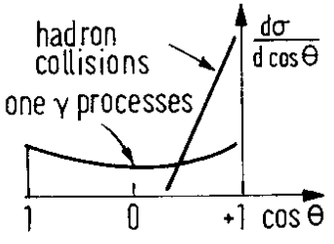

c) Vector Meson Production

One of the dominant features of hadron production is the formation and consecutive decay of vector mesons:

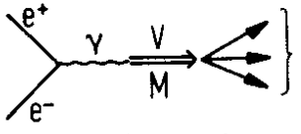

$$\sigma_f = \frac{3\pi}{s} \cdot \frac{\Gamma_{ee} \cdot \Gamma_f}{(M-\sqrt{s})^2 + \frac{\Gamma^2}{4}}$$

In the expression for the cross section Γ_{ee}, Γ_f, and Γ are the respective partial and total widths, M is the mass of the vector meson V and $\sqrt{s} = 2E$ is the center of mass energy. Some of the known vector mesons are given in the following table[53]:

V	M MeV	Γ MeV	Γ_{ee} keV
ρ	773 ± 3	152 ± 3	6.4 ± 0.8
ω	783 ± 1	10 ± 1	0.8 ± 0.2
φ	1020 ± 1	4 ± 1	1.1 ± 0.2
J/ψ	3096 ± 1	0.067 ± 0.012	4.8 ± 0.6
ψ'	3687 ± 1	0.228 ± 0.056	2.2 ± 0.3

As one can see from columns three and four, the electronic width has approximately the same value for all the vector mesons, whereas

the total widths of the J/ψ and ψ' mesons are several orders of magnitude smaller than for their low mass partners. This has been the first indication of a new quantum number, called charm, which will be discussed later.

d) Quark Parton Model

In the quark parton model[21,54] the total e^+e^- hadronic cross section at high energies is visualized as the production of quark pairs which in turn burst into hadrons.

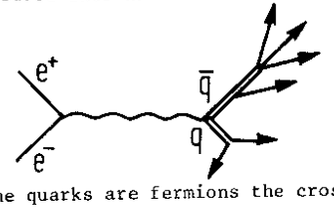

$$\sigma(e^+e^- \to q\bar{q}) = Q^2 \cdot \sigma_{\mu\mu}$$

Since the quarks are fermions the cross section is the same as for μ-pairs, only the quark charge Q modifies the $q\bar{q}$ coupling. To obtain the total cross section one has to sum over all quark pairs:

$$\sigma(e^+e^- \to \text{hadrons}) = \sum_i Q_i^2 \cdot \sigma_{\mu\mu} = R \cdot \sigma_{\mu\mu} \quad .$$

For various models the theoretical values of R are given in the following table where u, d, s denote the conventional quarks, c the charm quark and the index "col." means colour model.

model	u, d, s	$(u, d, s)_{col.}$	u, d, s, c	$(u, d, s, c)_{col.}$	Han-Nambu
$R = \sum_i Q_i^2$	$\frac{2}{3}$	2	$\frac{10}{9}$	$\frac{10}{3}$	4

How these phenomenological considerations match the experimental facts is shown in Fig.3.1 where the dominant vector mesons are shown schematically and the ratio R outside the resonance varies between two and five[55,56]. This was the status in e^+e^- physics when the detectors at DORIS were set up and ready to start the investigations.

3.2 The Storage Ring DORIS

The e^+e^- colliding beam facility at DESY is a double ring structure (DORIS) with separate magnetic guiding fields for e^+ and e^-. This concept

allows a higher luminosity than a single ring machine for beam energies below 2 GeV and it can provide e^-e^- colliding beams.

A schematic view of the storage ring with its two interaction regions W is shown in Fig.3.2. Positrons and electrons are injected at 400 MeV from a linear accelerator into the DESY-synchrotron, where they are accelerated to the final energy and transferred to the storage rings. Until the fall of 1976 DORIS has been operated at total cms energies between 3.0 and 4.8 GeV. The maximum luminosity achieved has been $2 \cdot 10^{30} cm^{-2} sec^{-1}$ at machine currents of 150 mA. The time between fillings is normally between 2 and 5 hours. The storage rings are equipped with sufficient power to run up to energies of 8.6 GeV. Measurements at these highest energies are scheduled for the period 1977/1978.

3.3. Detectors at DORIS

What were the main objectives when designing e^+e^- colliding beam experiments? It has already been known in 1972 from experiments at the Frascati National Laboratory[56] that the hadron production was governed by many-body final states (average charged particle multiplicity of 3.5 at 3 GeV cms energy). In order to completely analyse high multiplicity hadronic events, the ideal detector should cover as much as possible of the full solid angle and identify the long-lived charged particles (e, μ, π, k, p) as well as photons. The detector has to determine the directions of the particles and, if possible, their momenta. Up to four unmeasured quantities can be obtained from energy and momentum conservation. The background from cosmic rays and beam gas interactions is reduced by requiring that some tracks of an event originate from the interaction region. Exclusive final states are best separated from the background if they are measured so well that they are kinematically overconstrained.

It is difficult and expensive to combine all the ideal requirements in a single detector. Therefore, different aspects have been emphasized by three experimental teams working at DORIS. These detectors are: the non-magnetic detector of the DESY-Heidelberg group, the double arm spectrometer of the DASP-collaboration and the solenoid detector of the PLUTO group. These will be discussed in the following:

a) Non-Magnetic Detector (DESY and Univ. Heidelberg)
In this set-up (Fig. 3.3) the beam pipe is surrounded by cylindrical drift chambers, followed by NaI and lead glass counters, cosmic

ray counters, an iron shield and the muon chambers. A mercury converter of two radiation lengths thickness in front of the last drift chamber can be filled or emptied between runs. A view along the beam pipe is shown in Fig. 3.4. The fraction of the full solid angle subtended for μ detection is 32%, for electron and photon detection 45% and for charged particles 95%. The energy resolution $\Delta E/E$ is $\pm$ 2% x $E^{-1/4}$ for NaI and $\pm$ 6% x $E^{-1/2}$ for lead glass (E in GeV). An event trigger is defined by:

0 track in drift chamber and deposited energy $\geq$ 1.5 GeV or
1 track " " " and " " $\geq$ 0.9 GeV or
2 tracks " " " and " " $\geq$ 0.4 GeV etc.

With this type of detector one can measure the directions of charged particles and photons and distinguish leptons and photons from hadrons. Events with less than 5 tracks can be kinematically reconstructed from the particle directions.

b) Double Arm Spectrometer DASP (T.H. Aachen, DESY, Univ. Hamburg, M.P.I. München, Univ. Tokyo)
The experimental arrangement consists of two detectors:
The double arm spectrometer with limited acceptance (8% of 4π) and a nonmagnetic inner detector covering a large fraction of the solid angle (~70%). Each spectrometer arm (top view shown in Fig. 3.5) has three wire chambers in front of the magnet and five chambers behind the magnet followed by a time of flight counter, a shower counter, and a range counter with a scintillator array after 70 cm of iron and additional slots to insert wire chambers. The maximum field length of each magnet is 18 kGm which corrsponds to a momentum resolution of $\Delta p/p = \pm 0.7\% \times p$ (GeV). The time of flight counter separates pions from kaons up to 1.6 GeV/c and kaons from protons up to 3 GeV/c. The lead-scintillator shower counter for electrons and photons has an energy resolution of $\Delta E/E \approx 30\% \times E^{-1/2}$ (E in GeV). All counters are segmented in various ways to allow multiple hits.

The inner detector is located between the two magnets and a view along the beam pipe is shown in Fig. 3.6. In addition to the six wire chambers mentioned above there are four layers of sandwiches consisting of scintillator, lead and proportional tubes to measure the conversion points of photons. On the outside the inner detector is surrounded by lead-scintillator shower counters.

The double arme spectrometer is triggered purely inclusively on a single track traversing one of the beam pipe counters as well as the time of flight and shower counter. The inner detector is triggered on e^+e^- or $\gamma\gamma$ due to the energy deposited or on more than two tracks or photons.

This detector provides complete particle separation and momentum determination in a limited solid angle and measures the direction of charged particles and photons in the inner detector.

c) Magnetic Solenoid Detector PLUTO (DESY, Univ. Hamburg, Univ. Siegen and Univ. Wuppertal)

The superconducting magnetic detector PLUTO has a usable volume of 1.4 m in diameter by 1.05 m in length filled with 14 cylindrical proportional chambers (Fig. 3.7). Two lead converters at radii of 37.5 and 59.4 cm have a thickness of 0.44 and 1.7 radiation lengths respectively. The maximum field is 20 kG corresponding to a momentum resolution of $\Delta p/p = \pm 2\% \times p$ (GeV). The event trigger requires two or more tracks and covers 86% of the solid angle. The muon chambers outside the iron return yoke subtend 55% of the solid angle.

This solenoid detector measures the momenta of charged particles in a large solid angle and provides some information on converted electrons and photons. It is therefore well suited for few and multibody analysis.

More details on these detectors and the names of the members of the respective groups are given in various publications quoted in the physics sections.

3.4 Results from DORIS

When the particles J/ψ and ψ' were discovered, the detectors DASP and PLUTO just entered the phase of final checkout. In this situation the experimental equipment was committed immediately to measuring the quantum numbers and other properties of the new particles.

3.4.1 Properties of J/ψ and ψ'

The quantum numbers are discussed first and some more general properties at the end of this chapter.

a) Spin, Parity and C-Parity

Anticipating that the new particles are produced via one-photon-annihilation, we expect the spin-parity quantum numbers to be $J^{PC} = 1^{--}$. This has been confirmed by the observation that the two photon final state is completely explained by the QED process $e^+e^- \to \gamma\gamma$ (Fig. 3.8) and there is no evidence for the particles at 3.1 and 3.7 GeV to decay directly into two photons[57]. This excludes $J^P = 0^+$ and 2^+. The symmetry of the $\mu^+\mu^-$ decay angular distribution of J/ψ (Fig. 3.9) excludes 1^+ and its compatibility with $1 + \cos^2\theta$ makes the assignment of 0^- or 2^- unlikely[58].

The C-parity $C = -1$ follows from the parity, since CP invariance is expected to hold for the μ-pair final state

$$(\mu^+\mu^-) = CP(\mu^+\mu^-) = -C(\mu^+\mu^-)$$

b) G-Parity and Isospin

Odd G-parity forbids all strong decays into even numbers of pions. For the J/ψ the following branching ratio or decay width into $\pi^+\pi^-$ is observed[59]:

$$\frac{\Gamma_{\pi^+\pi^-}}{\Gamma_{all}} = (1 \pm 0.7) \cdot 10^{-4} \quad \text{or} \quad \Gamma_{\pi^+\pi^-} = 7 \pm 5 \text{ eV}$$

In order to see whether this fraction of $\pi\pi$ final states can be explained by the ρ-tail, let us look at the following diagrams:

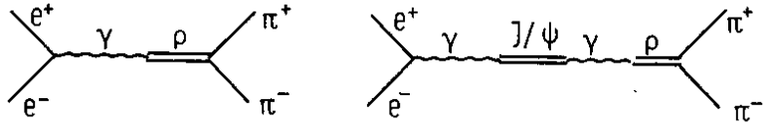

The contribution from the first graph at a center of mass energy of 3.1 GeV can be obtained from the Orsay measurement of 1.6 μb at the ρ-peak and the ρ-pole formula[60]:

$$\sigma_{\pi^+\pi^-,\mathrm{off}} = 1.6\ \mu b \cdot \frac{m_\rho^2}{s} \cdot \frac{m_\rho^2\,\Gamma_\rho^2}{(m_\rho^2 - s)^2 + m_\rho^2\,\Gamma_\rho^2} \approx 5 pb$$

In this context "off" means off-resonance or non-resonance production. From this number we can get the contribution of the second graph. By using the μ-pair cross section from section 3.1.a and the measured μ-pair decay width ($\Gamma_{\mu\mu} \simeq \Gamma_{ee}$ in section 3.1.c) for J/ψ we obtain for its $\pi^+\pi^-$ decay width

$$\Gamma_{\pi^+\pi^-} = \frac{\sigma_{\pi^+\pi^-}}{\sigma_{\mu^+\mu^-}}\Bigg|_{\mathrm{off}} \times \Gamma_{\mu^+\mu^-} \simeq 10\ \mathrm{eV}$$

which agrees with the measured number. Since there is no evidence for a direct $\pi\pi$ decay we conclude that the G-parity of J/ψ is -1. The $\pi\pi$ rate will be discussed in greater detail in a later section on meson form factors.

Inserting $G = -1$ and $C = -1$ into $G = C \times (-1)^I$, we see that only even values of isospin are possible. The observation of the direct decay into $p\bar{p}$ selects $I = 0$ for the J/ψ[59]:

$$\frac{\Gamma_{p\bar{p}}}{\Gamma} = (2.3 \pm 0.3) \times 10^{-3} \quad \text{or} \quad \Gamma_{p\bar{p}} = 160 \pm 20\ \mathrm{eV}$$

The $p\bar{p}$ fraction expected from ρ-ω-ϕ dominance calculations does not exceed 40 eV[61].

Since the ψ' is the heavier partner of the J/ψ, does it also have the same $I^G = 0^-$ assignment as the J/ψ? Let us look at the cascade decay $\psi' \to J/\psi + X$ in order to see which isospin and G-parity are carried away by X. Wiht $C = -1$ as the only restriction the whole unnatural series 0^-, 1^+, 2^-, ... would be possible. What is the experimental situation? The data and the expected numbers are compared in the following table[62]:

X	$B_X = \frac{P(\psi' \to J/\psi + X)}{\Gamma(\psi' \to J/\psi + \mathrm{all})}$	relative B_X expected for $I^G = 0^-$,	1^+,	2^-
$\pi^+\pi^-$	0.63 ± 0.10	2	1	1
$\pi^o\pi^o$	0.32 ± 0.10	1	0	2
η	0.065± 0.026	allowed	0	0

These cascade decays account for roughly 60% of all the ψ' decays. From the ratio of $\pi^+\pi^-$ and $\pi^o\pi^o$ for X in the final state and from the occurence of η we conclude that $I^G = 0^-$ is the only choice for the ψ'.

c) SU(3) Assignment

It is well established that the pseudoscalar mesons can be grouped into a SU(3) nonet in the following way:

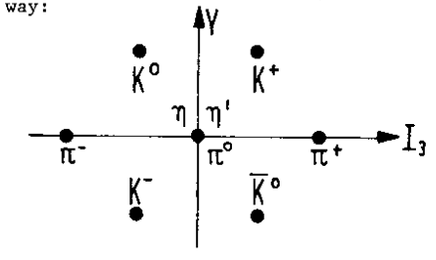

where the η' is predominantly a singlet state[13] and the remaining particles form an octet. What may we infer from not observing a direct decay of J/ψ into $\pi^+\pi^-$, as discussed in the previous section? Is the J/ψ a SU(3) singlet state? This conclusion is correct if none of the decay final states form an octet state. Therefore, not only the decay into $\pi^+\pi^-$ but also the K^+K^- decay must be forbidden. The experimental

branching ratios are given by[56]:

$$J/\psi \to \pi^+\pi^- \qquad \Gamma_f/\Gamma = (1.0 \pm 0.7) \times 10^{-4}$$
$$\to K^+K^- \qquad = (1.4 \pm 1.4) \times 10^{-4}$$
$$\psi' \to \pi^+\pi^- \qquad < 3.7 \times 10^{-4}$$
$$\to K^+K^- \qquad < 1.4 \times 10^{-3}$$

These values definitely favour the singlet assignment for J/ψ and ψ'. The two ratios for J/ψ are compared in the following section to form factor measurements at lower energies.

A mixture of singlet and octet amplitudes can contribute to the $\pi\rho$ and $K\overset{*}{K}(890)$ decays of the J/ψ. These decays are identified by the ρ or $\overset{*}{K}(890)$ recoil mass, observed in the double arm spectrometer (Fig. 3.10). The branching ratios are[59]:

$$J/\psi \to \pi^{\pm}\,\rho^{\mp} \qquad \Gamma_f/\Gamma = (0.78 \pm 0.19) \times 10^{-2}$$
$$\to K^{\pm}\,\overset{*}{K}{}^{\mp}(890) \qquad = (0.41 \pm 0.12) \times 10^{-2}$$

Inserting these experimental values into the corresponding SU(3) amplitudes

$$A(\pi^{\pm}\rho^{\mp}) = A_1 - 2A_8$$
$$A(K^{\pm}\overset{*}{K}{}^{\mp}(890)) = A_1 + A_8$$

and correcting for a phase space factor of 0.85 one gets for the ratio of octet to singlet amplitude

$$\frac{|A_8|}{|A_1|}\cos\delta = 0.07 \pm 0.06$$

where δ is the phace between the two amplitudes. This is, therefore, an independent check that J/ψ is predominantly a singlet state.

d) Meson Form Factors

If we assume that the J/ψ does not decay directly into $\pi^+\pi^-$ or

K^+K^-, the ratio of the following amplitudes

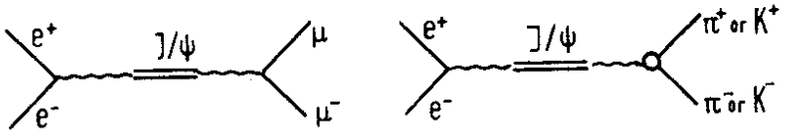

will measure the pion or kaon form factor:

$$|F_\pi|^2 = 4\,\frac{\Gamma_{\pi^+\pi^-}}{\Gamma_{\mu^+\mu^-}}\,, \qquad |F_K|^2 = 4\,\frac{\Gamma_{K^+K^-}}{\Gamma_{\mu^+\mu^-}}$$

Inserting this into the cross section formula for pair production of pseudoscalar mesons one obtains[63]

$$\sigma_{\pi,K} = \frac{\pi\alpha^2}{3s}\,|F_{\pi,K}(s)|^2 = \sigma_{\mu^+\mu^-}\,\frac{\Gamma_{\pi^+\pi^-,\ K^+K^-}}{\Gamma_{\mu^+\mu^-}}\,.$$

The experimental values for J/ψ and ψ' are given in the following table where for comparison the ρ-pole form factor of the pion is shown as well.

s[GeV]	$\lvert F_\pi\rvert^2$	$\lvert F_\pi\rvert^2 = (1 - \frac{s}{m_\rho^2})^{-2}$	$\lvert F_K\rvert^2$
3.1	$(5.6 \pm 4.0) \times 10^{-3}$	4.5×10^{-3}	$< 2 \times 10^{-2}$
3.7	< 0.15	2×10^{-3}	< 0.55

The form factor values at the J/ψ energy agree well with measurements at lower energies[64] shown in Fig.3.11.

e) Nucleon Form Factors

For purely electromagnetic $p\bar{p}$ production, the electric and magnetic nucleon form factors, G_E and G_M, would be obtained from the angular distribution[65] of the reaction $e^+e^- \to p\bar{p}$:

$$\frac{d\sigma}{d\Omega} = \frac{\alpha^2 m^2}{s^2}\,\{|G_E|^2\,\sin^2\theta + \frac{s}{4m^2}\,|G_M|^2\,(1 + \cos^2\theta)\}$$

where m is the nucleon mass and θ the scattering angle. As mentioned before, however, the J/ψ decays directly into $p\bar{p}$ which then precludes any definite statement concerning the nucleon form

factors at this energy. The $p\bar{p}$ pairs, identified by time of flight in the two opposite spectrometer arms of the DASP collaboration, are shown in Fig.3.12 where the recoiling mass M_x is plotted[59] versus the $p\bar{p}$ mass $M_{p\bar{p}}$. For the cluster of events at $M_{p\bar{p}} = 3.1$ GeV all the energy is carried away by the nucleons. If we take these events and compare the ratio of $p\bar{p}$ to $\mu^+\mu^-$ production to corresponding measurements at lower energies[56,66], we see from Fig.3.13 that the DASP point lies well above the value expected from nucleon form factor contributions. To interpret this direct decay of the J/ψ into $p\bar{p}$, the decay angular distribution is best written in terms of density matrix elements $\rho_{\lambda\bar{\lambda}}$ where $\lambda,\bar{\lambda}$ are the helicities of p and $\bar{p}$, respectively:

$$\frac{d\sigma}{d\Omega} \sim \rho_{\frac{1}{2},\frac{1}{2}} \sin^2\theta + \frac{1}{2}\rho_{\frac{1}{2},-\frac{1}{2}}(1+\cos^2\theta) \quad .$$

This first term corresponds to a D-wave and the second to an S-wave of the $p\bar{p}$ system. The two extreme angular distributions $1+\cos^2\theta$ for the S-wave and $\sin^2\theta$ for the D-wave are shown in Fig.3.14 together with the data points. In terms of the nucleon form factors $G_E \sim \rho_{\frac{1}{2},\frac{1}{2}}$ $(G_M = 0)$ is associated with the D-wave and $G_M \sim \rho_{\frac{1}{2},-\frac{1}{2}}$ $(G_E=0)$ with the S-wave. Within the statistics, the production of $p\bar{p}$ - as one example of the hadronic final states in section 3.1.b - is not only limited to the two lowest partial waves possible, but the S-wave seems to be preferred. However, more data are clearly needed.

f) Heavy Vector Meson Dominance

A direct way to determine how the photon couples to the new vector mesons consists in the measurement of their radiative decay widths. The expected decay widths would strongly depend on whether the photon couples only via the old vector mesons like the ρ or only via the new vector mesons like the J/ψ. For the J/ψ decay into η'γ the following orders of magnitude are expected[67]:

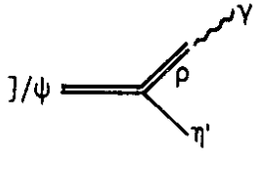

$\Gamma_{\eta'\gamma,\ \text{theory}} \sim 1$ eV

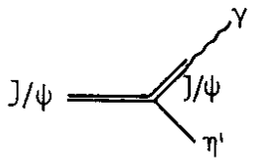

$\Gamma_{\eta'\gamma,\ \text{theory}} \sim 1$ keV

Do the experiments favour one of these values? In order to determine the η'γ decay width one can utilize the fact that 30% of the η' decay proceeds via $\rho^0\gamma$. In Fig.3.15 several invariant mass distributions[68] are shown for the $\pi^+\pi^-\gamma\gamma$ final state, where all charged tracks are assumed to be pions. The two photon spectrum in Fig.3.15a shows a strong signal from π^0's some of which are produced in addition to the ρ^0 in Fig.3.15b and some of which come from the decay of the $\rho^\pm$ in Fig.3.15c. The η' signal ist seen in Fig.3.15d and the signal to background ratio is enhanced if π^0 events are excluded and $\pi^+\pi^-$ combinations from the ρ-region selected. All the relevant kinematic cuts are given on the figure. From the observations we obtain the experimental value

$$\Gamma_{\eta'\gamma,\ \text{exp.}} = 160 \pm 50 \text{ eV}$$

and may conclude that the old vector meson dominance is not sufficient but that J/ψ and/or ψ' are required as new pieces of the electromagnetic current. The J/ψ decay into ηγ is smaller but of the same order of magnitude[69,70]:

$$\frac{\Gamma(J/\psi \to \eta'\gamma)}{\Gamma(J/\psi \to \eta\,\gamma)} = 2.4 \pm 1.0$$

g) Inclusive Spectra and Particle Ratios

In section 3.1 we have seen that the particles of hadron induced reactions have an angular distribution completely different from e^+e^- interactions. However, the large partial waves contribute mostly to forward hadron scattering and it might be interesting to compare the momenta of e^+e^- hadron production with the transverse momentum distribution of hadronic interactions. As already mentioned in the section on detectors, the double arm spectrometer allows π/k separation up to 1.6 GeV and k/p separation up to 3.0 GeV due to 0.6 nsec time resolution and a 5 m flight path. From Fig.3.16a one can see the quality of the particle separation. Even for the momentum range between 1.2 and 1.5 GeV the relative amount of

particles can be easily estimated. The excitation curve for the J/ψ resonance in Fig.3.16b is obtained with the single particle inclusive trigger[71].

Fig.3.17 shows the differential cross sections $d\sigma/dp$ for the π, k, and $\bar{p}$ particles at the J/ψ and ψ' resonances. Because of background problems from beam gas interactions, the protons have been omitted from the analysis. Both resonances show roughly the same behaviour. The kinematic effect caused by different particle masses is taken into account by plotting the invariant cross sections $\frac{E}{4\pi p^2} d\sigma/dp$ in Fig.3.18. The pion yield from the J/ψ can be described by a single exponential whereas for the ψ' one observes a break around $E_\pi = 400$ MeV due to the pions from the cascade decay $\psi' \to J/\psi + \pi^+\pi^-$. All particles at both resonances show a similar slope, compatible with $kT = 170$ MeV for the exponential $e^{-\frac{E}{kt}}$ [72]. Even more surprisingly, the same slope and also the same relative particle abundances are observed for particle production from pp collisions at the ISR [73]. The curves in Fig.3.18a represent the ISR particle spectra ($\sqrt{s} = 53$ GeV and 89° scattering angle) scaled with a common factor to fit the π spectrum from e^+e^- collisions.

The particle ratios at the resonances are shown in Fig.3.19 as a function of the momentum. The k and p ratios increase relative to the π yield with increasing momentum. Fitting the particle spectra with exponential functions one obtains the following particle yields for the entire momentum range[71]:

	$R_{\pi^\pm}$	$R_{k^\pm}$	$R_{p,\bar{p}}$
J/ψ	87.5 ± 1.5%	8.9 ± 1.0%	3.6 ± 0.9%
ψ'	90.8 ± 1.0%	6.9 ± 0.9%	2.3 ± 0.7%

h) Summary of J/ψ and ψ' Properties

Except for its mass and width there is no outstanding property which distinguishes the ψ' from the J/ψ. They have identical quantum numbers $J^{PC} = 1^{--}$ and $I^G = 0^-$ and are compatible with being SU(3) singlets. Having the same quantum numbers as the photon they seem to add additional pieces to the electromagnetic current in the vector dominance model. The inclusive particle spectra are similar for the two resonances and agree with slopes and relative abundances of particles produced under 90° in the cms of the hadronic induced reaction.

3.4.2 Hidden and Open Charm

Before the J/ψ and ψ' were discovered, all hadrons could be built from three quarks and their anti-quarks. In this picture the surprisingly narrow widths of the new particles (see section 3.1.c) pose a problem. One can try to explain these narrow widths in the same way as one has explained the suppression of the non-strange Φ decays: As mentioned already in section 2.1.a, the Φ is visualized as a $s\bar{s}$ state and therefore couples mainly to $K\bar{K}$ in its decay (Okubo-Zweig-Iizuka-rule[74]). By introducing a fourth quark c , carrying the charm quantum number, one can picture the J/ψ and ψ' particles as bound $c\bar{c}$ states. In this case the decay would proceed mainly via the charm-carrying mesons ($c\bar{q}$ or $\bar{c}q$); but if the mass of these new charmed mesons is larger than $\frac{M(\psi')}{2} = 1.84$ GeV, the decay of J/ψ and ψ' into charmed mesons is forbidden by energy conservation while the decay into normal non-charm hadrons is possible, though strongly suppressed.

In the following we shall briefly comment on the charm model and then present results from DORIS which are relevant to the charm picture.

a) Some Comments on the Charm Model

The concept of a charmed quark was introduced before the discovery of the new particles in order to achieve symmetry between leptons and quarks and to explain the absence of strangeness changing neutral currents[75]. Let us first consider mesons of hidden charm, which are built from a charm and an anti-charm quark [76], and therefore have charm quantum number zero. Such a system is called "charmonium" [77,78] in analogy to the electron positron bound state, "positronium" [79]. An essential point is that the mass of the charmed mesons is roughly half of the ψ' mass and, therefore, a non-relativistic description may be used to compute the level scheme[80]. Using field theoretical arguments theorists have proposed potentials with an r-dependence somewhere between the Coulomb and the oscillator potential. Level schemes of the type shown in Fig.3.20 for the lowest lying states have been derived, but the level spacings have to be adjusted empirically. Levels with the quantum numbers $J^{PC} = 1^{--}$, i.e. the states 1^3S_1, 2^3S_1 and 1^3D_1, can couple directly to the photon. The S-states correspond to the J/ψ and ψ'. There is at present no experimental evidence for the D-state; however, some theoretical speculations[81] place it at a mass around 3.75 GeV. The states which can be reached

by radiative transitions from the J/ψ and ψ' are those with positive C-parity. As we shall see in the following sections these radiative decays have been the object of extensive experimental investigations.

By introducing a fourth quark, the symmetry scheme of hadrons is generalized from SU(3) to SU(4). The meson nonets are replaced by hexadecuplets, each consisting out of the original nonet and a singlet meson with hidden charm (c = 0) plus two triplets of open charm (c = ±1). Each level in Fig.3.20 is a member of such a SU(4) multiplet[82] as we can see from the example of the pseudoscalar multiplet in Fig.3.21 which includes the 1^1S_0 state η_c' of Fig.3.20. The charm-carrying pseudoscalar mesons D and F are shown above (c = +1) and below (c = -1) the plane of the SU(3) nonet of conventional pseudoscalar mesons. As one can see from its quark constituents the F meson has in addition to charm also strangeness different from zero. The corresponding vector mesons D^* and F^* can be grouped together with J/ψ, ρ, ω, Φ and $K^*(890)$ into a similar SU(4) multiplet. Because the charm quantum number is conserved in strong and electromagnetic interactions, the states of open charm are produced in association with their corresponding anti-states. To prove the existence of charm-carrying particles one has to find their characteristic weak decays. In the following table some examples of hadronic and semileptonic decays[78,83] are given together with the relative decay rates for each type where c,u,d,s denote the charm and ordinary quarks and θ_c the Cabibbo angle[84].

c decay mode	example	relative rate
hadronic: $c \to s u \bar{d}$	$D^0\{\bar{u}\,c\}$ — W^+ — $\{u\,\bar{s}\}K^-$, $\bar{d}\,\pi^+$	$\cos^2\theta_c \simeq 1$ Cabibbo-angle favoured
$c \to d u \bar{d}$	$D^0\{\bar{u}\,c\}$ — W^+ — $\{u\,\bar{d}\}\pi^-$, $\bar{d}\,\pi^+$	$\sin^2\theta_c \simeq 0.05$ Cabibbo-angle suppressed
semileptonic: $c \to s \overset{e}{\mu} \nu$	$D^0\{\bar{u}\,c\}$ — W^+ — $\{\bar{u}\,s\}K^-$, ν_e, e^+	$\cos^2\theta_c \simeq 1$ Cabibbo-angle favoured
$c \to d \overset{e}{\mu} \nu$	$D^0\{\bar{u}\,c\}$ — $\{\bar{u}\,d\}\pi^-$, ν_e, e^+	$\sin^2\theta_c \simeq 0.05$ Cabibbo-angle suppressed

As one can see from these examples, the Cabbibo-angle favoured decays have a strange particle in the final state. The search for charm states has been carried out at DORIS along the line of semileptonic decays. The evidence for a signal from events with a low energy electron and for a possible electron kaon correlation is presented in section d) below.

b) States of Even Charge Conjugation and Hidden Charm Observed in Cascade Decays from ψ' to J/ψ

The first evidence[62,85] for an even C-parity intermediate state between ψ' and J/ψ came from the radiative cascade decay $\psi' \to J/\psi + \gamma\gamma$ observed in the DASP detector in two independent ways, i.e. by identifying the J/ψ via its e^+e^- decay in the inner detector and via its $\mu^+\mu^-$ decay in the outer detector arms.

To illustrate the method of analysis, we shall discuss the cascade decays $\psi' \to J/\psi + X$ with $J/\psi \to \mu^+\mu^-$ detected in the magnetic double arm spectrometer. The plot of the effective μ pair mass in Fig.3.22 shows two peaks: one from direct decays and QED processes at a mass of 3.7 GeV and a second one from the cascade decay into J/ψ at 3.1 GeV. Selecting events with $M_{\mu\mu}$ near 3.1 GeV one obtains the spectrum of the recoil mass squared in Fig.3.23. 88% of this spectrum can be explained by the final state $\mu^+\mu^-\pi\pi$ (solid curve) since the charged pions have a unique signature in the inner detector and the neutral pions add one half of the charged pions due to isospin considerations (see section 3.4.1.b). There is a clear η signal on top of this curve which accounts for 6% of the spectrum and, therefore, 6% of the events are left as candidates for cascade decays. However, only those events are taken which have two photons positively identified in the inner detector as shown in the computer drawn reconstruction for such an event in Fig. 3.24. In order to eliminate background from $\psi' \to J/\psi + \pi^0\pi^0$ it is required, that $J/\psi + \gamma\gamma$ be coplanar, and $J/\psi + \eta$ final states are avoided by selecting events with $M_{\gamma\gamma}$ less than 510 MeV. One then obtains by a 2 constraint fit a clean sample of 8 events, the photon energies of which are plotted in Fig. 3.25. One sees a clear clustering of 5 events at a

total energy of 3.51 ± 0.01 GeV ($E_{\gamma 1}$ = 170 MeV) or at 3.28 ± 0.01 GeV ($E_{\gamma 2} \simeq$ 400 MeV), depending on which photon is emitted first. This intermediate state - called P_c by the DASP collaboration - is narrower than 20 MeV and has the following product of branching ratios:

$$\frac{\Gamma(\psi' \to P_c\,\gamma)}{\Gamma(\psi' \to \text{all})} \times \frac{\Gamma(P_c \to J/\psi + \gamma)}{\Gamma(P_c \to \text{all})} = 4 \pm 2\%$$

The background in Fig. 3.25 is estimated to be less than 0.5 events.

The next important question is which photon is emitted first in the cascade decay. The two ambiguous photons, observed in the DESY-Heidelberg experiment[86], are plotted in Fig. 3.26. Selecting events from the shaded area in Fig. 3.26 one obtains the two angular distributions in Fig. 3.27 for the high and low energy photons. Whereas the high energy photon distribution is flat, the low energy photon seems to remember the polarisation of the electrons in the initial state. Therefore, one may conclude that the low energy photon is emitted first and that the P_c mass is 3.51 ± 0.01 GeV. The fitted angular distribution for the low energy photon is $1 + \alpha \cos^2\theta$ with $\alpha = -1.1 \pm 0.3$. This excludes spin 0 for the P_c state since that would require a $1 + \cos^2\theta$ angular distribution.

We now can assume that the low energy photon is always emitted first and plot the DASP events together with the same type of events from SLAC-LBL[51,87] in Fig. 3.28. We see that for the high mass solution there are possibly four states at masses of 3.41, 3.45, 3.51 and 3.55 GeV. The state at 3.41 GeV has been observed to decay strongly into $\pi^+\pi^-$ and K^+K^- and there are some indications of these decay modes for the 3.55 GeV state[51,88]. The decay into pseudoscalar mesons necessitates the natural spin-parity series 0^+, 1^-, 2^+ etc. Assuming the normal triplet splitting (higher masses for higher angular momenta) and having $J^{PC} = 0^{++}$, 0^{-+}, 1^{++}, 2^{++}, 2^{-+} at our disposal from the charmonium level scheme (Fig. 3.20) we would assign 0^{++} to the 3.41 GeV state and 2^{++} to the 3.55 GeV state. If for some reason the D-wave state 2^{-+} were forced to lie at higher masses one could assign 1^{++} to the P_c state

at 3.51 GeV and 0^{-+} to the 3.45 GeV state.

The question whether there are cascade decays from states above the ψ' is hard to answer since these states would lie above the threshold for charm meson production[89]. Some indications might come from two events, observed by the PLUTO group to have total visible energies exceeding the ψ' mass:

$$e^+e^- \to J/\psi + X \qquad J/\psi \to \mu^+\mu^-$$

e^+e^- energy	4.2	4.72	GeV
$M_{\mu\mu}$	3.13 ± 0.03	2.96 ± 0.8	GeV
X	$\pi^+\pi^-$	$\pi^+\pi^-\gamma$ or $\pi^+\pi^-\pi^0$	
M_X	0.92 ± 0.03	1.02 ± 0.17	GeV

In order to identify well defined states above the ψ' one certainly needs more than 2 events, and these events have to be observed in a detector which covers practically the full solid angle, in order to detect all the outgoing particles.

c) State with Even Charge Conjugation below the J/ψ

Since the 1^1S_0 state is expected to lie energetically below the 1^3S_1 state a search for the even C-parity 0^{-+} state has been performed among the decays of the J/ψ. Here, the results on the three photon final states observed in the DASP detector shall be reported[70].

Three photon final states may be caused by direct decays or by quasi-two-body decays:

$$\begin{aligned} J/\psi &\to \pi^0\gamma \to \gamma\gamma\gamma \\ &\to \eta\,\gamma \to \gamma\gamma\gamma \\ &\to \eta'\gamma \to \gamma\gamma\gamma \\ &\to X\,\gamma \to \gamma\gamma\gamma \end{aligned}$$

or by QED contributions:

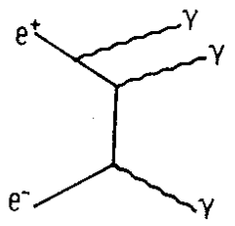

The latter poses a serious background problem in the search for any two photon intermediate state, because it leads to a smooth contribution to the γγ mass distribution which cannot be eliminated by kinematic cuts, but must be subtracted. The following cuts were applied to remove several sources of background:

(i) The smallest of the γγ opening angles was required to be larger than 30°. This avoids overlapping showers from neighbouring photons and eliminates $\pi^{0}\gamma$ events.

(ii) The coplanarity of the three photons had to be better than 5°. This removes four and more photon events.

(iii) Small angles between the beam axis and the three photon plane were excluded by requiring that the photon directions projected onto a plane perpendicular to the beam axis show a smallest opening angle larger than 5°. This cut reduces the QED background, but it also rejects good events and introduces a cut-off at a maximum two photon mass.

Following these cuts, the three photon energies can be obtained from a one constraint fit. Among the three γγ mass combinations two are independent. Plotting the lowest and highest mass solution results in the two histograms in Fig. 3.29. The low mass distribution shows a clear η signal whereas the high mass distribution has a spike of 3.5 standard deviations at 2.83 ± 0.05 GeV which is for short called X(2.8). The background curve underneath is obtained from QED calculations and from the kinematic reflections of η and η'. For the three photon events at the ψ' energy[90] we observe a similar shape of the spectrum near the ψ' mass and a small accumulation of events around 2.8 GeV (Fig. 3.30). However, the signal of four events on top of the QED background cannot be considered as statistically significant. The branching ratios obtained with the DASP detector are the following:

$$BR(J/\psi \to X\gamma) \cdot BR(X \to \gamma\gamma) = (1.2 \pm 0.5) \times 10^{-4}$$
$$BR(\psi' \to X\gamma) \cdot BR(X \to \gamma\gamma) < 3.4 \times 10^{-4}$$

The results from the DESY-Heidelberg group[86] agree with the findings; only the mass of this new object seems to be shifted to a slightly lower value of 2.7 GeV which is different from the DASP value by two or three standard deviations in terms of mass resolution. Further results from the three photon investigations have been the following branching ratios[70,90]:

decay mode	J/ψ	ψ'
$\pi^{0}\gamma$	$(7.3 \pm 4.7) \times 10^{-5}$	$< 10^{-2}$
$\eta\gamma$	$(0.8 \pm 0.18) \times 10^{-3}$	$< 1.6 \times 10^{-4}$
$\eta'\gamma$	$(2.2 \pm 1.7) \times 10^{-3}$	$< 1.2 \times 10^{-4}$

We close the sections on even C-parity states with the remark that it seems puzzling that for the X(2.8) as well as for the 3.45 GeV state the direct hadronic decays are strongly suppressed. Another remarkable observation is, that the spin orbit splitting of the P_c states in the previous section is of the order of 100 MeV and therefore relatively large with respect to the separation of the states J/ψ and ψ' with different main quantum numbers. But more surprisingly, the hyperfine splitting of the $^{3}S_{1}$ and $^{1}S_{1}$ states is with 250 MeV even larger than the spin orbit splitting.

d) Semileptonic Decays of Charmed Particles

What can we learn from the inclusive electron spectrum in a search for semileptonic decays of charmed particles? One has to keep in mind that low energy electrons can come from radiative QED processes or possibly from the decays of heavy leptons or charmed mesons. Whereas heavy leptons decay mainly leptonically or semileptonically, the decay of charmed mesons is expected to be mostly semileptonic or hadronic. Consequently, the particle multiplicity of heavy lepton decays should be low and the average electron momentum high [91], and the reverse should hold for charmed particles.

In order to improve the electron/pion separation in the double arm spectrometer for low momenta, a Cerenkov counter was needed in addition to the shower counter [92]. This Cerenkov counter was inserted between the second and third wire chamber of the inner detector (Fig. 3.31) in the spring of 1976 and first results were available half a year later.

In the first round of experiments data were taken at e^+e^- energies between 4.0 and 4.2 GeV and control measurements performed at 3.6 GeV to obtain a reliable estimate for background events and at 3.68 GeV to see how frequently - with the ψ' as pion source - a pion would fake an electron. Whereas the electron trigger was purely inclusive, it was required in the data analysis that at least one non-showering track was present, and this removed the QED events most of which are produced with $e^+e^-\gamma$ in the final state. In order to discriminate against various types of background, the following cuts were made [92]:

(i) The pulse height of the scintillation counters S_o and S_M in Fig. 3.31 had to be that of a minimum ionizing track. This rejects events with Dalitz decays from π^o or η or with pair conversion of photons in front of the Cerenkov counter where one of the leptons curls up in the magnetic field. Events below the dashed lines in Fig. 3.32a were taken.

(ii) The independent identification of particles in the Cerenkov and in the shower counter helps to avoid that pions or kaons fake electrons via knock-on electrons. Events above the dashed lines in Fig. 3.32b were taken.

(iii) Beam gas events were rejected by an appropriate vertex cut (Fig. 3.32c).

After these cuts 28 events with one electron and at least one non-showering track remain for $\sqrt{s}$ between 4.0 and 4.2 GeV. The background is estimated to be ~7 events. Neglecting contributions from two photon processes, one may conclude that one has observed the production of a new particle which decays weakly. In order to distinguish between heavy leptons and charmed particles, the multiplicity of charged and neutral tracks is shown in Fig.3.33. A comparison with a Monte Carlo simulated multiplicity distribution of heavy sequential leptons [93] in Fig.3.34 shows that the characteristic feature of the experimental distribution, which peaks at a multiplicity of 5 and has only six events below 4, is not reproduced. Additional evidence comes from the electron

momentum distribution for events with a multiplicity larger than three (Fig. 3.35). The observed spectrum shows much lower values than expected for a heavy lepton with a mass of 1.9 GeV (V-A theory and massless neutrino). Note that above 700 MeV no electron has been observed at all. Therefore, the most likely interpretation is that the events come from the semileptonic decay of a hadron carrying a new quantum number which is conserved in strong and electromagnetic interactions.

For the high multiplicity events ($n \geq 4$) the cross section is plotted in Fig.3.36 as a function of energy. The strong increase of the cross section near 4 GeV and the fall-off are consistent with the threshold behaviour for pair production of particles with mass between 1.8 and 2.0 GeV. The lower limit for the production cross section times branching ratio is estimated to be:

$$\sigma(e^+e^- \to e + \text{hadrons}) \simeq 2 \cdot BR(H \to e + X) \cdot \sigma(e^+e^- \to H\bar{H}) > 1\text{nb}$$

Once we have established the semileptonic decay of a new hadron we may go back to the question whether we observe kaons in coincidence with the electrons as expected in the charm model (section 3.4.2.a). The PLUTO group has observed such correlations between electrons and neutral kaons [94]. Among their hadronic events they selected neutral kaons by reconstructing a common vertex for a positively and a negatively charged track and requiring that this vertex has a minimum distance from the interaction point of 5 mm and that the parent momentum points at the interaction region. The effective mass for K^o candidates so selected is shown in Fig. 3.37a for three different cms energies. A K^o signal on top of a smooth hand-drawn background is seen at about 0.5 GeV in all three cases but most pronounced for energies above 4 GeV. Next it is required that for this event sample an electron of at least 300 MeV momentum converted in the second radiator of 1.7 radiation lengths thickness (see section 3.3.c). In Fig. 3.37b the ratio of events with $e^\pm\pi^+\pi^-$ to all the hadronic events in the sample is plotted and one observes at 4.1 GeV a signal for e-K correlations rising above the background level of 4% whereas no such correlation is seen at

4.4 GeV. The background level corresponds to the fraction of 3% π/e misidentification obtained from a pion sample at the ψ' resonance.

Selecting events with $0.46 < m_{\pi\pi} < 0.54$ GeV, the visible cross section for e-K correlation is plotted in Fig. 3.38 as a function of the energy and shows a surprisingly narrow peak at about 4.05 GeV. After background subtraction and corrections for acceptance, branching ratio, and unobserved K_L^o mesons one finds a peak cross section of $\sigma(e^+e^- \to eK^o + \text{anything}) = 3\text{nb}$ with a systematic uncertainty of a factor of two. The multiplicity of the eK_S^o events consists on the average of 2.5 observed additional charged tracks and the electron momentum is in general below 700 MeV. These observations agree with the findings of the DASP group and lead with the occurence of e-K correlations to the conclusion that the weakly decaying hadrons are charmed particles.

The question of correlation between electrons and charged particles has been approached by the DASP group by identifying pions and kaons via time of flight and by looking for coincident electron showers of at least 250 MeV in the inner detector. As a preliminary result the number of $e\pi^\pm$ events normalized to the number of charged pions passing through the spectrometer are plotted in Fig. 3.39a as a function of energy. The point below the ψ' resonance defines the background level (dash-dotted line) and a clear increase of genuine $e\pi^\pm$ is seen above 4 GeV. One can now ask: Is this increase expected because of the observed inclusive electron cross section? The answer is yes, and the dashed lines show the ratio estimated from $\frac{\sigma(e^+e^- \to e + \text{anything})}{\sigma(e^+e^- \to \text{hadrons})}$ x (number of charged pions through the spectrometer arms). The increase in $eK^\pm$ events is not that trivial. The $eK^\pm$ data points, the background level (dash-dotted line), and the estimated increase (dashed line) are shown in Fig. 3.39b. The obvious interpretation of the observed behaviour is that for the inclusive electron production one has an increased probability to find a kaon, in agreement with the charm model predictions discussed in section 3.4.2.a.

In conclusion, DORIS experiments have found evidence for weakly decaying charmed particles, the mass of which must lie between 1.8 and 2 GeV as indicated by the threshold behaviour of the cross section. Since semileptonic decays always include neutrinos the particle mass cannot be reconstructed directly.

e) Summary on Observed Charm States

Most of the states predicted by the charm model have quantum numbers different from the photon. The even C-parity states have been observed in radiative decays of the ψ' and J/ψ. The P_c states have been identified in the cascade decay $\psi' \to J/\psi + \gamma\gamma$. They occur at masses of 3.41, 3.45, 3.51, and 3.55 GeV and are tentatively associated with the J^P quantum numbers 0^+, 0^-, 1^+, and 2^+ respectively. A further state at 2.83 GeV has been obtained from the radiative decay of the J/ψ and, according to the charm model, it can be associated with $J^P = 0^-$. For this state the two photon decay has been observed as its only decay mode sofar. In this respect it is similar to the state at 3.45 GeV for which no hadronic decay mode has been seen either.

The charm-carrying states have been identified by their weak decays. The approach at DORIS has been to single out the semileptonic decays of these states. An inclusive electron spectrum, characteristic for such decays - and completely different from the spectra of heavy sequential lepton decays - has been observed. In addition, the expected e-K correlation has been seen. The mass of these charm-carrying states can be deduced from the threshold behaviour of the cross section to lie between 1.8 and 2.0 GeV.

f) Open Questions

The first and obvious question in the light of the SPEAR findings on heavy leptons[95] is, whether the inclusive electrons from heavy leptons are hidden in the spectra for charmed particles, and how can we distinguish these two processes. One way is to measure carefully the energy dependence of inclusive electron data for high and low particle

multiplicities. The cross section for charmed particle production (high multiplicity) near threshold should level off at higher energies, whereas the cross section for heavy lepton production should vary only moderately for energies well above the threshold. Another possibility is, to search for two-lepton events, which may either yield an enriched sample of heavy leptons or, for the case of charmed particles, still exhibit a strong correlation with kaons. To settle this question additional data have been taken by the DASP and PLUTO experiments at energies between 4 and 5 GeV, and the results should be published soon.

A further question concerning the charm model is: Do we see any evidence for F mesons? The F mesons carry strangeness in addition to charm and, therefore, should be a particularly rich source of kaons as one can see from the following diagrams:

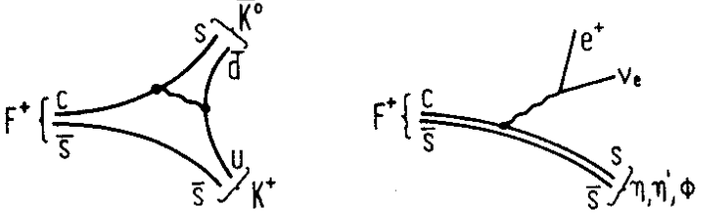

For the semileptonic diagram the η, η', and Φ couple to kaon pairs. In particular the Φ decays into K^+K^- in 47% and into $K_L^oK_S^o$ in 35% of the cases. However, only additional measurements can clarify this situation.

3.5 e^+e^- Physics at Higher Energies

The unexpected findings at present energies, which brought electron physics into the limelight of physics interest, have caused an ever increasing urge, to continue the e^+e^- investigations at energies beyond the presently available range. Some of the points of interest are:

(i) A careful measurement of R, the ratio of hadronic to μ pair cross section, for finding possible new degrees of freedom, i.e. possible evidence for additional quantum numbers.

(ii) Since the electromagnetic cross sections are falling as the inverse square of the cm energy, other types of interaction will become increasingly important, such as weak interactions and two photon processes.

As an example, the influence of weak interactions on μ pair production has been studied[96]. In addition to one photon exchange with its $1 + \cos^2\theta$ angular distribution we have contributions from the weak neutral current:

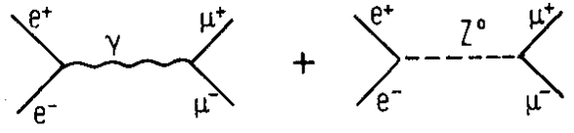

Neglecting effects from electron or positron polarization, the interference of weak and electromagnetic interactions will modify the simple $(1 + \cos^2\theta)$ behaviour in the following way:

$$\frac{d\sigma}{d\Omega} = \frac{\alpha^2}{16E^2}\left\{(1 + \frac{2E^2 g_V^2}{\pi\alpha(4E^2 - M_Z^2)})(1 + \cos^2\theta) + \frac{4E^2 g_A^2}{\pi\alpha(4E^2 - M_Z^2)}\cos\theta\right\}$$

where E is the cms energy, M_Z the Z^o mass and g_V, g_A the vector and axialvector couplings. The difference $\frac{\Delta\sigma}{\sigma}$ in the integrated cross section measures the vector coupling, and the asymmetry $A = \frac{\sigma_- - \sigma_+}{\sigma_- + \sigma_+}$, which can be interpreted as a charge asymmetry, determines the axial vector coupling. From standard V-A theory and from the Weinberg model it is expected that changes in σ and in A will be of the order of 10% for beam energies of 15 GeV.

Two photon processes, which are of fourth order in QED, become increasingly important at higher energies:

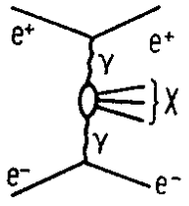

$$\sigma(E) \sim \frac{\alpha^n}{m^2} (\ell n \frac{E}{m_e})^2 (\ell n \frac{E}{m_e})^n$$

where E, m_e are the electron energy and mass and $n \geq 1$ depends on the specific final state X. Note that this cross section does not drop like $\frac{1}{s}$, but the cms energy is replaced by the threshold mass m of the state X. One can also see from the cross section formula that one power of α is approximately cancelled since $(\ln \frac{E}{m_e})^2 \approx 100$ for E = 15 GeV. However, to positively identify the two photon processes, it would be advantageous to catch at least one of the electrons scattered at small angles with respect to the beam. Therefore, a special forward detector close to the beam line would be a useful tool to obtain information on these processes.

A more detailed discussion of the physics interest in high energy electron positron colliding beams and of possible implications for detector arrangements has been given elsewhere[97].

a) PETRA, a Next Generation Storage Ring

The growing interest in high energy e^+e^- colliding beams was the reason for proposing a 2 x 19 GeV Positron-Electron-Tandem-Ring-Accelerator, PETRA, at DESY. Fig.3.40 shows the layout of PETRA. The circumference of the ring is 2.3 km and the bending radius 197 m. The ring has octogonal shape with rounded corners. There are eight straight sections, two of which house the radio frequency system. The other six are available for experiments, but at the beginning only four interaction regions will be equipped. Fast and relatively inexpensive construction of PETRA is possible by using the 7.5 GeV electron-synchrotron and the storage ring DORIS as injector and intermediate storage ring. The scheme of injection

is indicated in Fig.3.41. Electrons and positrons, injected into the synchrotron by two linacs, are accelerated in DESY up to 2.2 GeV and transfered and accumulated in DORIS. Fast kickers will then eject individual bunches from DORIS for re-injection into DESY. After acceleration up to 7 GeV, these single bunches will be injected into PETRA. This scheme assures short filling times of the ring which are estimated to be of the order of 10 minutes.

The PETRA proposal was submitted to the authorities in the fall of 1974 and approved one year later. Ground breaking took place in January 1976. The construction of more than three quarters of the tunnel, the injection channels and the experimental halls were finished by the end of 1976. The installation of machine components has started and is expected to be completed in September 1978. First injections into the PETRA tunnel are scheduled for the spring of 1977. The installation of the experiments may start in January 1979 and data taking commence in the middle of 1979. The initial operation of PETRA will be at 15 GeV, and the luminosity is expected to be close to 10^{32} $cm^{-2}sec^{-1}$.

b) Proposed Experiments

All of the experiments, proposed to be installed in the interaction regions at PETRA, use a magnetic field surrounding the interaction point and try to cover as much as possible of the full solid angle. The various experiments differ in some of the means of particle identification.

Five proposals have been presented at a meeting in August and accepted on October 19 for the first round of experiments. Collaborations from the following universities and institutions are involved, and their projects have been given the short names on the left:

CELLO: DESY-Karlsruhe-Munich-Orsay-Paris-Saclay[98].

TASSO: Aachen-Bonn-DESY-Hamburg-Imp.College, London-Oxford-Rutherford Lab.-Weizmann Inst. (Rehovot)[99].

MARK J: DESY-MIT and FOM(Holland) Collaboration[100].

JADE : Daresbury Lab.-DESY-Hamburg-Heidelberg-Lancaster-Manchester-Tokyo[101].

PLUTO: Aachen-DESY-Hamburg-Frascati-Siegen-Wuppertal[102].

The experiments can be classified according to their physics objectives. Three examples are taken from the list above. Experiment "MARK J" (Fig.3.42) has a very narrow core of wire chambers and shower counters surrounded by magnetic iron into which drift chambers are inserted. The main interest of this experiment is to determine weak interaction effects by observing μ pair final states. Experiment "JADE" (Fig.3.43) uses a magnetic solenoid of approximately 1 m radius surrounded by lead glass counters and range counters. This set-up intends to carefully identify electrons and photons; the directions of the photons can be obtained by using the coordinates of the interacting point known from the charged tracks. Experiment "TASSO"(Fig.3.45) has a magnetic solenoid of close to 1.5 m radius. Electrons and muons are identified by shower and range counters in a large fraction of the solid angle and hadrons are classified by a set of Cerenkov counters with a limited spatial acceptance. Further details on future experiments at PETRA should be obtained from the written proposals.

It is a pleasure to acknowledge the help of many colleagues at DESY for supplying us with data and figures on the respective experiments.

References

(1) Proceedings of the 1975 International Symposium on Lepton and Photon Interactions at High Energies, Stanford, 1975.
B. H. Wiik and G. Wolf; DESY 77/01 (1977)

(2) See for example: J. D. Bjorken and S. D. Drell;
Relativistic Quantum Mechanics (Mc Graw-Hill, N.Y., 1964)

(3) N. Dombey, p.17 in: Hadronic Interactions of Electrons and Photons
(Scottish Universities Summer School, 1970,
ed.: J. Cumming and H. Osborn, Academic Press, London, 1971)

(4) See e.g.: Wissenschaftlicher Jahresbericht, DESY, Hamburg, 1975

(5) J. Gayler; DESY 76/42 (1976) and Proceedings of the Topical Conference on Baryon Resonances, Oxford, 1976, p.219

(6) G. Weber; High Energy Physics Proceedings of the EPS Internationa Conference, Palermo, 1975, p.1183 and DESY 75/17

(7) A. Silverman; Proceedings of the 1975 International Symposium on Lepton and Photon Interactions at High Energies, Stanford, 1975, p.355

(8) J. J. Aubert et al.; Phys. Rev. Letters 33, 1404 (1974)

(9) J.-E. Augustin et al.; Phys. Rev. Letters 33, 1406 (1974)

(10) J. J. Sakurai; Proceedings of the 4th International Symposium on Electron and Photon Interactions at High Energies, Liverpool, 1969, p.91.
J. J. Sakurai; Currents and Mesons (Univ. of Chicago Press, 1969).
H. Fraas and D. Schildknecht; Nucl. Phys. B14, 543 (1969).
D. Schildknecht; Springer Tracts in Modern Physics (Springer, Berlin, 1972) p.57

(11) A. N. Diddens; Proceedings of the XVIIth International Conference on High Energy Physics, London, 1974, p.I-41.
M. Derrick, ibid. p.I-3 and ANL-HEP-CP-75-52 (1975)

(12) J. D. Bjorken; Proceedings of the 1971 International Symposium on Electron and Photon Interactions at High Energies, Cornell, 1971, p.281

(13) B. T. Feld; Models of Elementary Particles (Blaisdell, London, 1969)

(14) H.-J. Behrend et al.; DESY 75/05 and Phys. Letters 56B, 408 (1975).
H. J. Behrend et al.; Paper submitted to XVIII International Conference on High Energy Physics, Tiblisi, 1976

(15) V. Barteneo et al., Phys. Rev. Letters 31, 1088 (1973);
similar values were derived by A. Martin; Nucl. Phys. B77, 226 (1974),
and by D. P. Roy et al., ibid., p.240

(16) R. K. Carnegie et al.; SLAC-PUB-1610 (1975)

(17) S. Bartolucci et al.; DESY 76/43 and Nuovo Cimento (to be published)

(18) H. H. Bingham et al.; Phys. Letters 41B, 635 (1972).
G. Barbarino et al.; Nuovo Cimento 3, 689 (1972)

(19) J. C. Pati, p.384 in: Current Induced Reactions (Summer Inst. on
Theoretical Particle Physics in Hamburg, 1975, ed. Körner, Kramer,
Schildknecht; Springer, Berlin, 1976)

(20) R. E. Taylor; Proceedings of the 1975 International Symposium on Lepton
and Photon Interactions at High Energies, Stanford, 1975, p.679

(21) R. P. Feynman; Photon-Hadron Interactions (W. A. Benjamin, Reading,
Mass., 1972)

(22) J. J. Sakurai; Phys. Rev. Letters 30, 245 (1973)

(23) F. W. Brasse et al.; DESY 75/23 and Phys. Letters 58B, 467 (1975)

(24) P. Brauel et al.; DESY 76/33 and Phys. Letters 65B, 181 (1976)

(25) P. Brauel et al.; Phys. Letters 65B, 184 (1976)

(26) G. Buschhorn et al.; Phys. Rev. Letters 17, 1027 (1966).
G. Buschhorn et al.; Phys. Rev. Letters 18, 551 (1967).
Z. Bar-Yam et al.; Phys. Rev. Letters 19, 40 (1967)

(27) C. J. Bebek et al.; Phys. Rev. D13, 25 (1976).
S. D. Holmes et al.; Phys. Rev. Letters 35, 1313 (1975)

(28) H. Ackermann et al.; DESY 76/44 and Nucl. Phys. (to be published)

(29) T. Azemoon et al.; Paper submitted to 6th International Symposium on
Electron and Photon Interactions at High Energies, Bonn 1973

(30) B. M. Abramov et al.; Preprint, Moscow Inst. for Theoretical and
Experimental Physics GKAE-ITEF-35 (1973)

(31) DESY-Glasgow-Collaboration, paper submitted to the 1975 International
Symposium on Lepton and Photon Interactions at High Energies, Stanford, 1975

(32) P. Bosetti et al.; Nucl. Phys. B54, 141 (1973)

(33) M. Burfeindt et al.; Nucl. Phys. B74, 189 (1974)

(34) C. J. Bebek et al.; Phys. Rev. Letters 34, 115 (1975)

(35) P. Joos et al.; DESY 76/17 and Nucl. Phys. B13,53 (1976)

(36) P. Joos et al.; DESY 76/09 and Phys. Letters 62B, 230 (1976)

(37) P. Brauel et al.; DESY 73/24 and Phys. Letters 45B, 389 (1973).
A. Del Guerra et al.; Daresbury Preprint, DL/P 256 (1976) and
Nucl. Phys. B107, 65 (1976)

(38) D. H. Perkins; Proceedings of the 1975 International Symposium on
Lepton and Photon Interactions at High Energies, Stanford, 1975, p.571

(39) K. Moffeit; Proceedings of the 6th International Symposium on Electron
and Photon Interactions at High Energies, Bonn, 1973, p.313

(40) ABBHHM Collaboration; Phys. Rev. 175, 1669 (1968)

(41) J. Ballam et al.; Phys. Rev. D5, 545 (1972)

(42) E. M. Riordan et al.; SLAC-PUB-1634 (1975)

(43) J. Ballam et al.; Phys. Rev. D10, 765 (1974)

(44) J. Dakin et al.; Phys. Rev. D8, 687 (1973)

(45) K. Gottfried; Proceedings of the 1971 International Symposium on
Electron and Photon Interactions at High Energies, Cornell, 1971, p.222

(46) L. Criegee et al.; DESY 77/07 and Nucl. Phys. (to be published)

(47) S. Hartwig et al.; Paper submitted to the XVIIIth International
Conference on High Energy Physics, Tiblisi, 1976

(48) D. Schildknecht; Nucl. Phys. B66, 398 (1973)

(49) S. Stein et al.; Phys. Rev. D12, 1884 (1975)

(50) J. Bernabeu; Nucl. Phys. B49, 186 (1972)

(51) F. Pierre; Saclay Preprint, D Ph P E 76-21 (1976)

(52) N. Arteago-Romero et al.; Phys. Rev. D3, 1569 (1971).
S. L. Brodsky et al.; Phys. Rev. D4, 1532 (1971).
H. Terezawa; Rev. Mod. Phys. 45, 615 (1973).
G. Bonneau and F. Martin; Nucl. Phys. B27, 381 (1974)

(53) Particle Data Group; Rev. Mod. Phys. 48, No.2, Part II (1976)

(54) S. D. Drell and T. M. Yan; Annals Phys. 66, 578 (N.Y., 1971).
S. D. Drell; Proceedings of the XVIth International Conference on High Energy Physics, Chicago, 1972, Vol.2, p.8.
J. Kogut and L. Susskind; Phys. Reports 8, 75 (1973).
M. L. Perl; High Energy Hadron Physics (Wiley, N.Y., 1974)

(55) A. M. Boyarski et al.; Phys. Rev. Letters 34, 762 (1975).
J.-E. Augustin et al.; Phys. Rev. Letters 34, 764 (1975)

(56) V. Silvestrini; Proceedings of the XVIth International Conference on High Energy Physics, Chicago, 1972, Vol.4, p.1

(57) DASP-Collaboration, W. Braunschweig et al.; DESY 74/62 and Phys. Letters 53B, 491 (1975)

(58) DASP-Collaboration, W. Braunschweig et al.; DESY 75/07 and Phys. Letters 56B, 491 (1975)

(59) DASP-Collaboration, W. Braunschweig et al.; DESY 76/28 and Phys. Letters 63B, 487 (1976)

(60) J. E. Augustin et al.; Phys. Letters 28B,508 (1969)

(61) F. M. Renard; Phys. Letters 47B, 361 (1973)

(62) B. H. Wiik; DESY 75/37 and Proceedings of the 1975 International Symposium on Lepton and Photon Interactions at High Energies, Stanford, 1975, p.69

(63) G. J. Feldman and M. L. Perl; Phys. Reports 19C, 233 (1975)

(64) M. Bernardini et al.; Phys. Letters 46B, 261 (1973)

(65) R. Gatto; Proceedings of the 1965 International Symposium on Electron and Photon Interactions at High Energies, Hamburg, 1965, Vol.I, p.106

(66) M. Conversi et al.; Nuovo Cimento 40A, 690 (1965).
D. L. Hartill et al.; Phys. Rev. 184, 1415 (1969)

(67) D. Schildknecht and F. Steiner; DESY 74/55 and Phys. Letters 56B, 36 (1975).
T. F. Walsh; DESY 75/21 and Lett. Nuovo Cimento 14, 290 (1975).
R. N. Cahn and M. S. Chanowitz; Phys. Letters 59B, 277 (1975).
H. Harari; Phys. Letters 60B, 172 (1976).
A. Kazi et al.; DESY 75/38 and Lett. Nuovo Cimento 15, 120 (1976)

(68) W. Bartel et al.; DESY 76/40 and Phys. Letters 64B, 483 (1976)

(69) W. Bartel et al.; DESY 76/65 and Phys. Letters (to be published)

(70) DASP-Collaboration, W. Braunschweig et al.; DESY 77/02 and Phys. Letters (to be published).

(71) DASP-Collaboration, W. Braunschweig et al.; DESY 76/21 and Phys. Letters 63B, 115 (1976)

(72) J. Engels et al.; Nuovo Cimento 17A, 535 (1973).
F. Elvekjiar; DESY 75/53.
F. Elvekjiar and F. Steiner; Phys. Letters 60B, 456 (1976)

(73) British-Scandinavian Collaboration, B. Alper et al.; Nucl. Phys. B87, 19 (1975)

(74) S. Okubo; Phys. Letters 5, 105 (1963).
G. Zweig; CERN TH 401, 412 (1964).
J. Iizuka et al.; Progr. Theor. Phys. 35, 1061 (1966)

(75) Y. Hava; Phys. Rev. B134, 701 (1964).
J. D. Bjorken and S. L. Glashow; Phys. Letters 11, 255 (1964).
S. L. Glashow et al.; Phys. Rev. D2, 1285 (1970)

(76) T. Appelquist et al.; Phys. Rev. Letters 34, 43 (1975).
C. G. Callan et al.; Phys. Rev. Letters 34, 52 (1975).
T. Appelquist et al.; Phys. Rev. Letters 34,365 (1975),
E. Eichten et al.; Phys. Rev. Letters 34, 369 (1975)

(77) L. B. Okun and M. B. Voloshin; Preprint, Moscow Inst. of Theoretical and Experimental Physics, ITEP-152, 1976.
A. De Rujula; Proceedings of the XVIIIth International Conference on High Energy Physics, Tiblisi, 1976 (to be published)

(78) J. D. Jackson; Proceedings of the Summer Institute on Particle Physics, SLAC, Stanford, 1976 (to be published)

(79) See e.g.; D. H. Perkins; Introduction to High Energy Physics (Addison-Wesley, Reading, Mass., 1972)

(80) J. Pumplin et al.; Phys. Rev. Letters 35, 1538 (1975).
H. J. Schnitzer; Phys. Rev. Letters 35, 1540 (1975).
H. J. Schnitzer; Phys. Rev. D13, 74 (1976)

(81) E. Eichten et al.; Phys. Rev. Letters 36, 500 (1976)

(82) M. K. Gaillard et al.; Rev. Mod. Phys. 47, 277 (1975)

(83) M. B. Einhorn and C. Quigg; Phys. Rev. D12, 2015 (1975)

(84) C. Jarlskog; Proceedings of the 1974 CERN School of Physics, CERN 74/22, 1974, p.1.
J. Leite Lopes; Weak Currents, Lectures at the Ecole Internationale de Physique des Particules Elementaires, Basko Polje, Makarska, Yugoslavia

(85) DASP-Collaboration, W. Braunschweig et al.; DESY 75/20 and Phys. Letters 57B, 407 (1975)

(86) W. Bartel et al.; Paper submitted to the XVIIIth International Conference on High Energy Physics, Tibliski, 1976

(87) W. Tannenbaum et al.; Phys. Rev. Letters 35, 1323 (1975)

(88) G. J. Feldmann et al.; Phys. Rev. Letters 35, 821 (1975)

(89) G. Goldhaber et al.; Phys. Rev. Letters 37, 255 (1976)
I. Peruzzi et al.; Phys. Rev. Letters 37, 569 (1976)

(90) DASP-Collaboration, W. Braunschweig et al.; DESY 77/03 and Phys. Letters (to be published)

(91) Y. I. Azimov et al.; Preprint, Leningrad Nuclear Physics Inst., No.245, 1976.
C. H. Llewellyn-Smith; Heavy Leptons, Oxford Preprint, No.33/76, and Proceedings of the Royal Society, London (to be published)

(92) DASP-Collaboration, W. Braunschweig et al.; DESY 76/37 and Phys. Letters 64B, 471 (1976)

(93) Y. S. Tsai; Phys. Rev. D4, 2821 (1971).
J. D. Bjorken and C. H. Llewellyn-Smith; Phys. Rev. D7, 887 (1973).
K. Fuyikawa and N. Kawamoto; DESY 76/01.
K. J. F. Graemers and R. Raito; SLAC-PUB-1727 (1976)

(94) J. Burmester et al.; DESY 76/50 and Phys. Letters 64B, 369 (1976)

(95) M. L. Perl et al.; Phys. Rev. Letters 35, 1489 (1975).
M. L. Perl et al.; Phys. Letters 63B, 466 (1976)

(96) D. Buchholz et al.; Proceedings of the 1974 PEP Summer Study, SLAC, Stanford, 1974, p.283

(97) Proceedings of the 1974 and 1975 Summer Studies, SLAC, Stanford.

(98) PETRA Proposal 76/13

(99) PETRA Proposal 76/14

(100) PETRA Proposals 76/15 and 76/18

(101) PETRA Proposal 76/16

(102) PETRA Proposal 76/19.

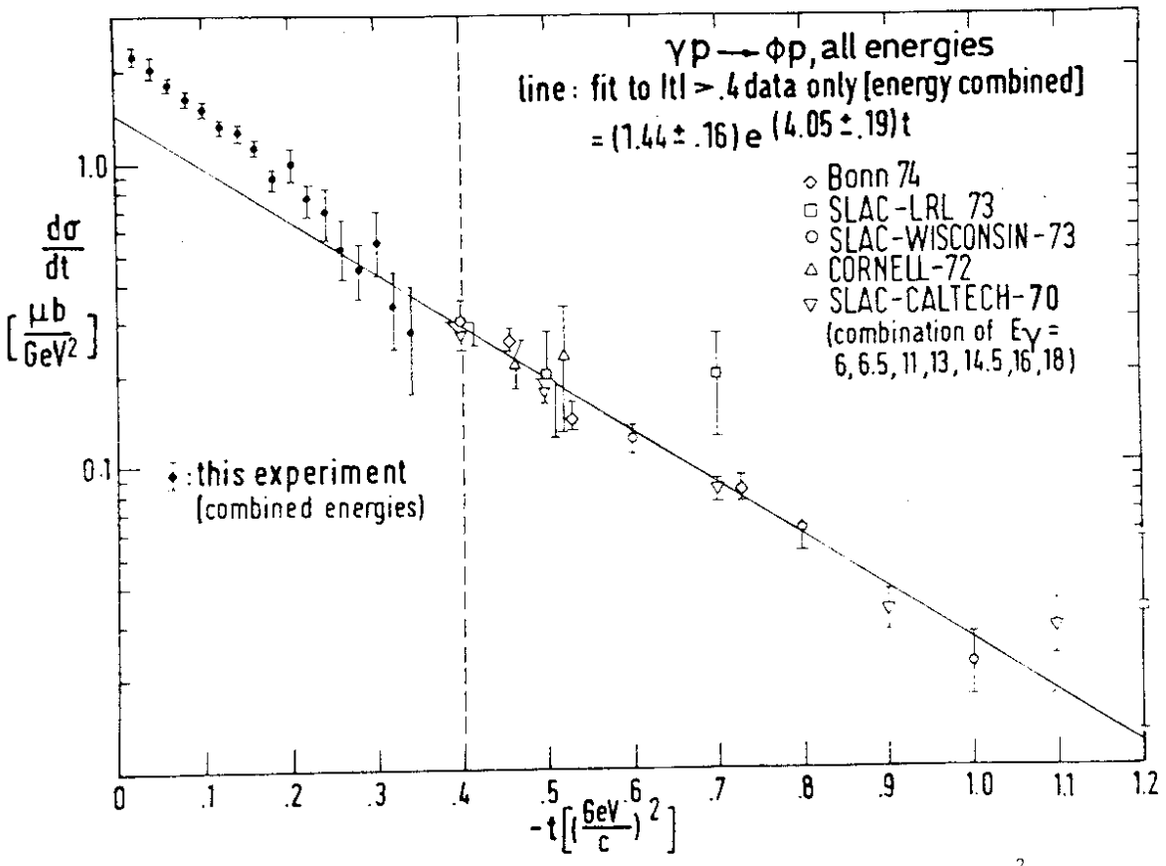

FIG.2.2 Differential cross section for elastic φ production. New results for $|t| < 0.4$ GeV^2 are shown together with the results of previous experiments for $|t| \geq 0.4$ GeV^2.

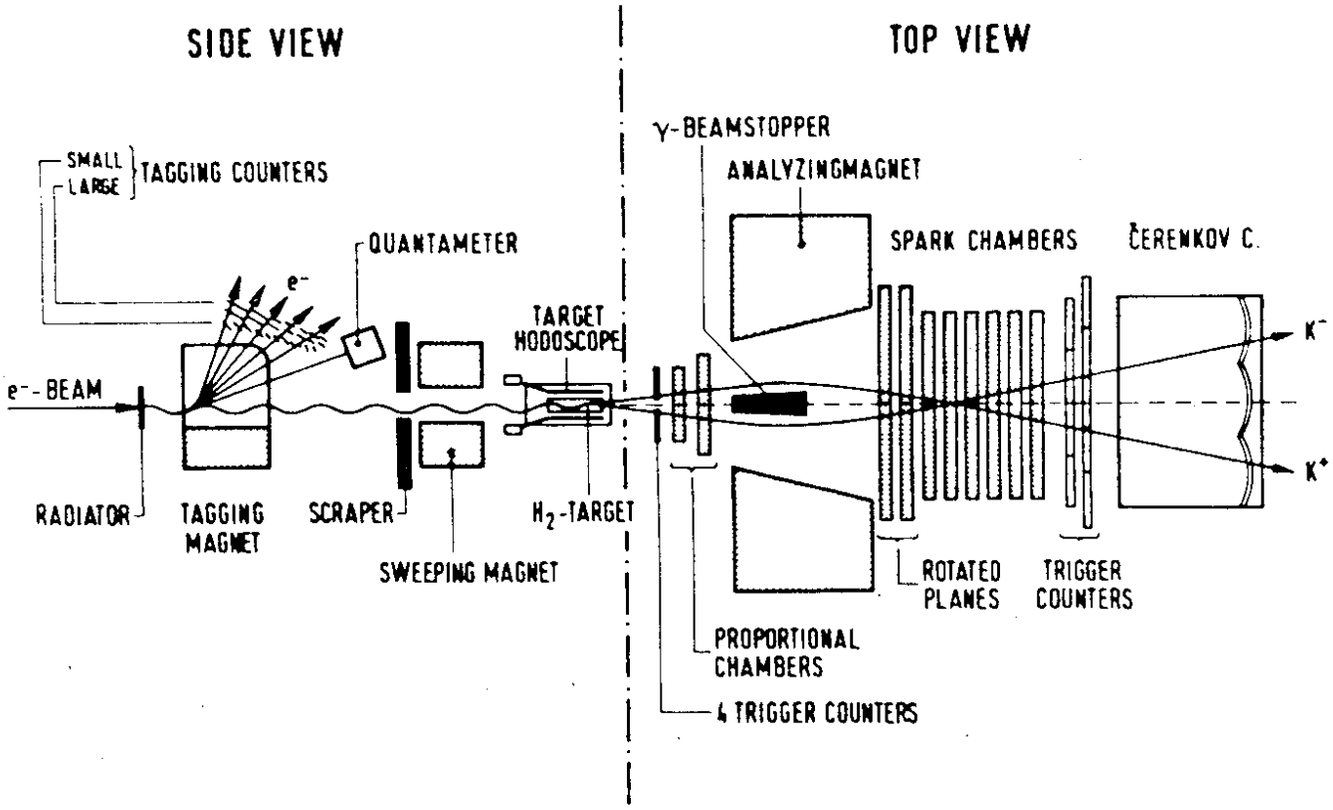

FIG.2.1 Experimental set-up for photoproduction of φ mesons.

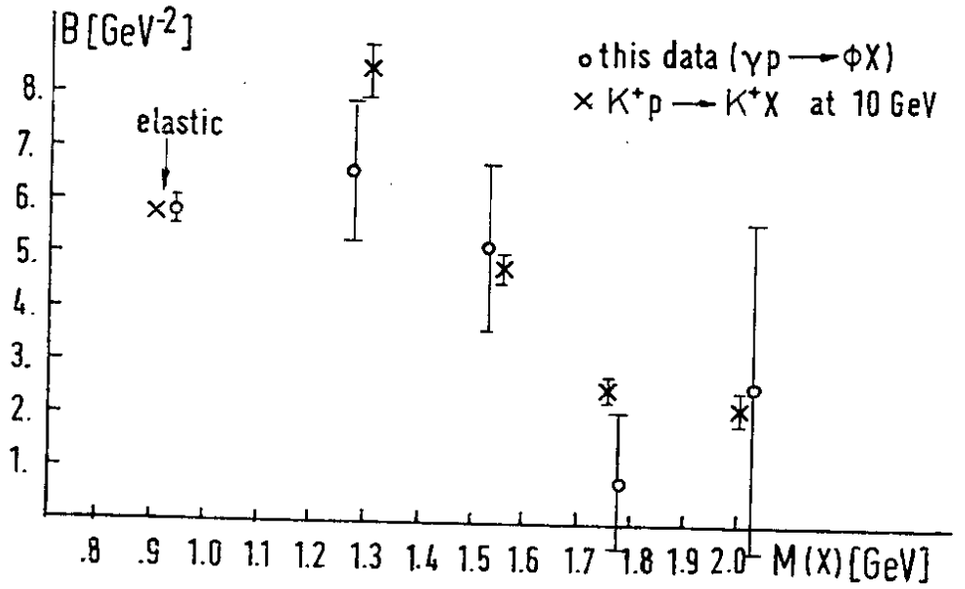

FIG.2.4 The slope parameter B derived by fitting A · exp{-Bt} to the inelastic φ production data as a function of the missing mass. The slope parameter for $K^+p \to K^+X$ (see Ref.16) are shown for comparison.

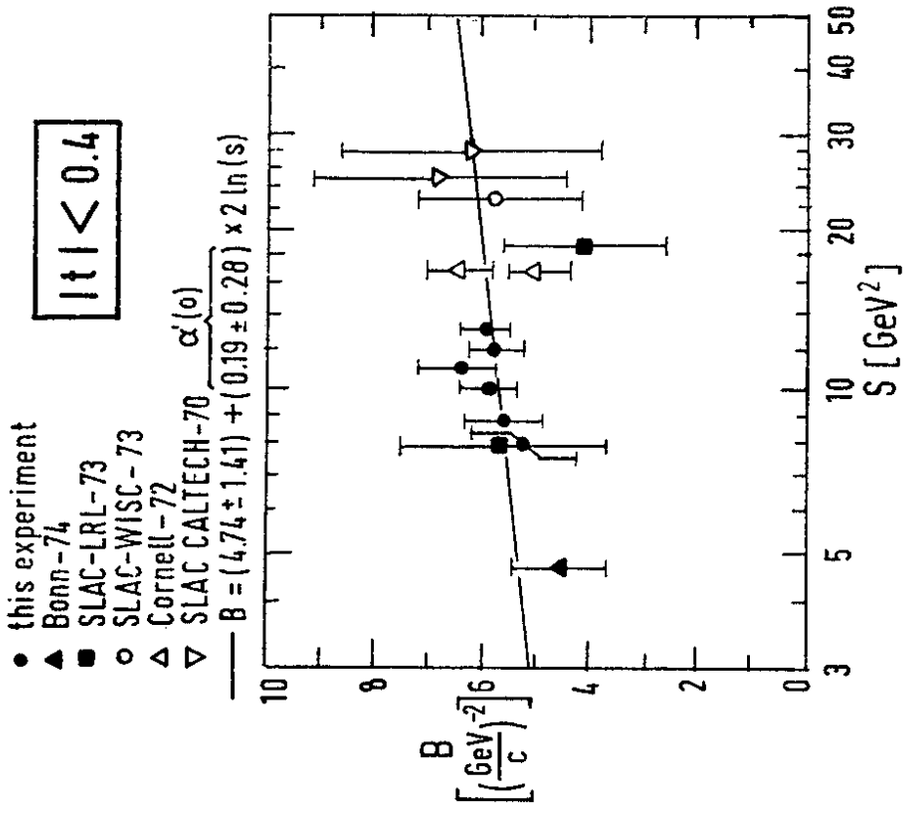

FIG.2.3 The slope parameter B of the elastic cross section $\frac{d\sigma}{dt} = \left.\frac{d\sigma}{dt}\right|_{t=0} \cdot \exp\{-B\,t\}$ for $|t| \leq 0.4$ GeV^2.

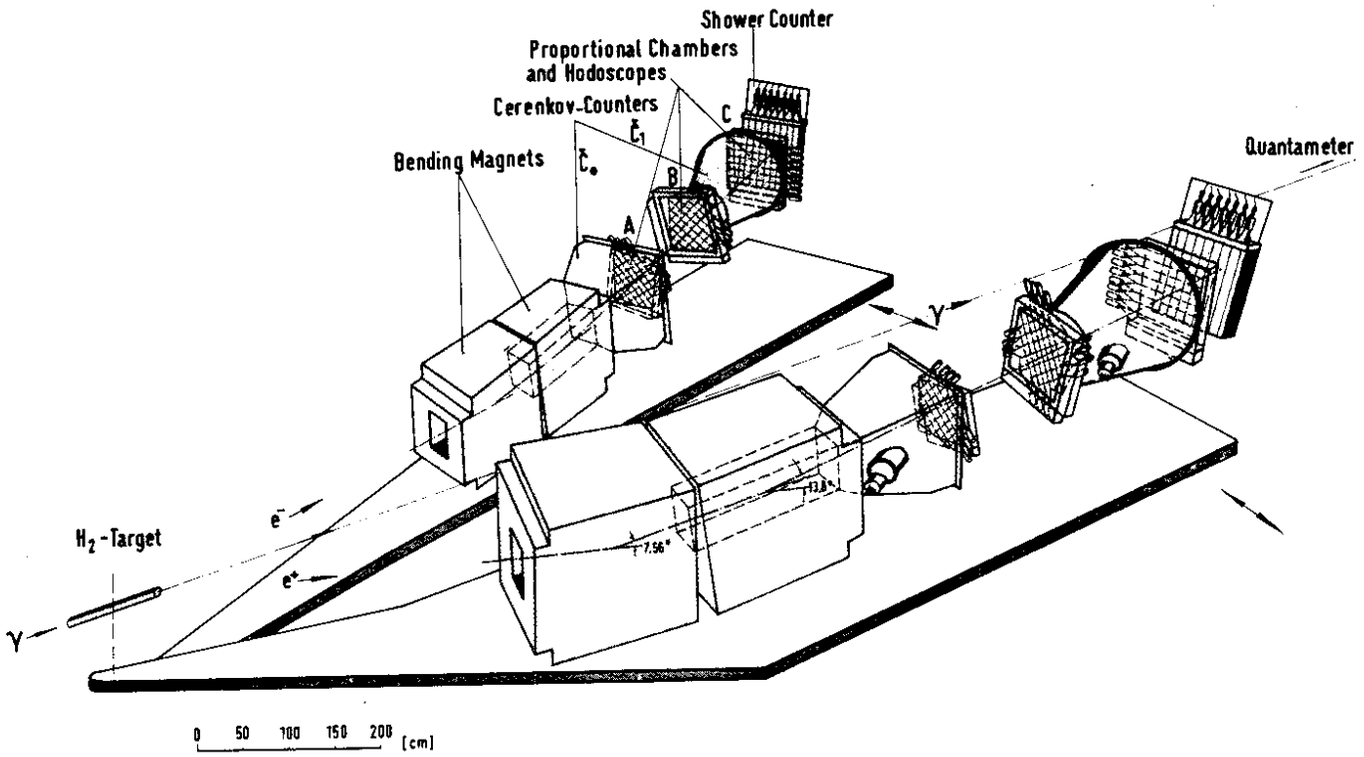

FIG.2.6 Experimental set-up for photoproduction of electron positron pairs.

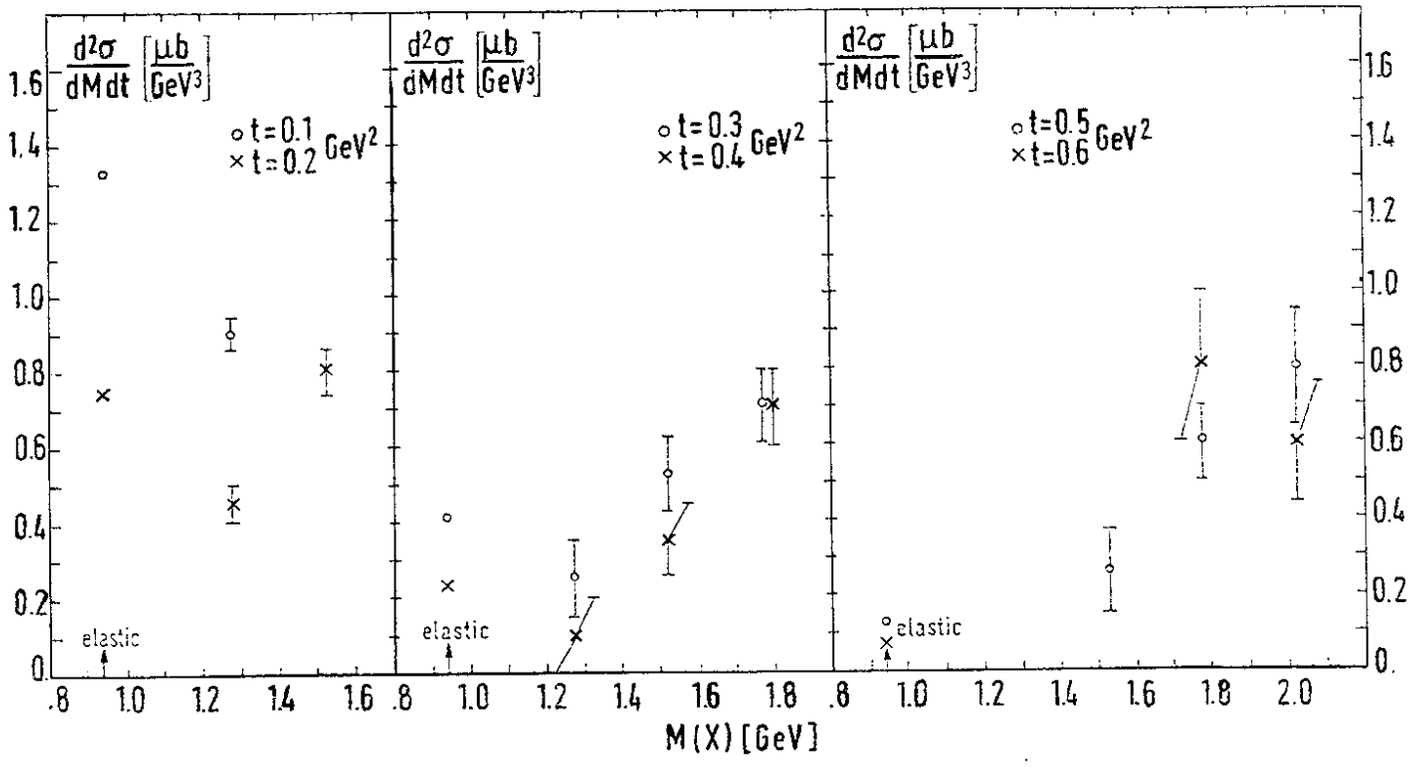

FIG.2.5 The inelastic Φ production cross section normalized to 1 GeV mass bin for different values of t as a function of the missing mass. The elastic cross section, given in μb/GeV^2, is also shown.

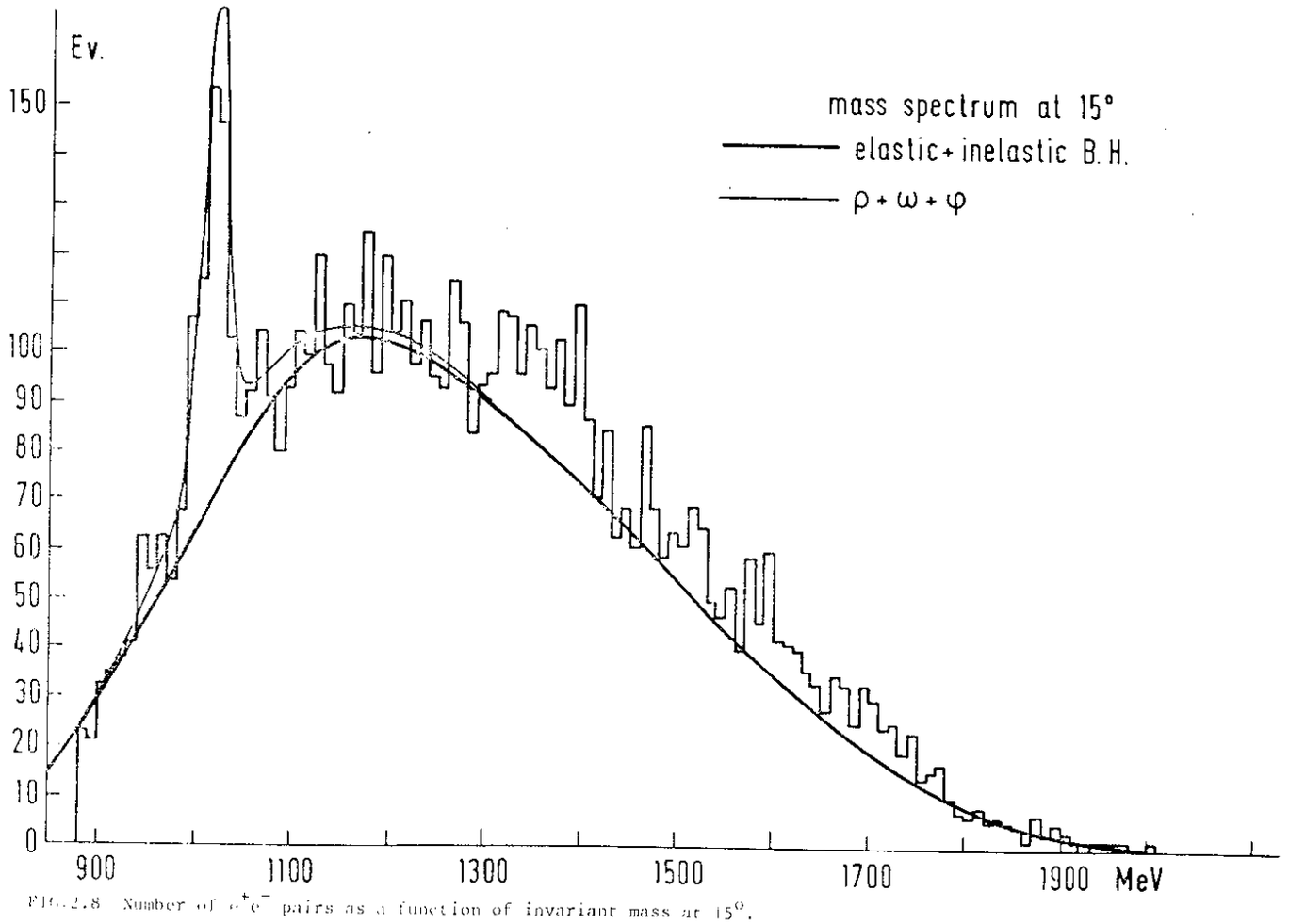

FIG.2.8 Number of e^+e^- pairs as a function of invariant mass at 15°.

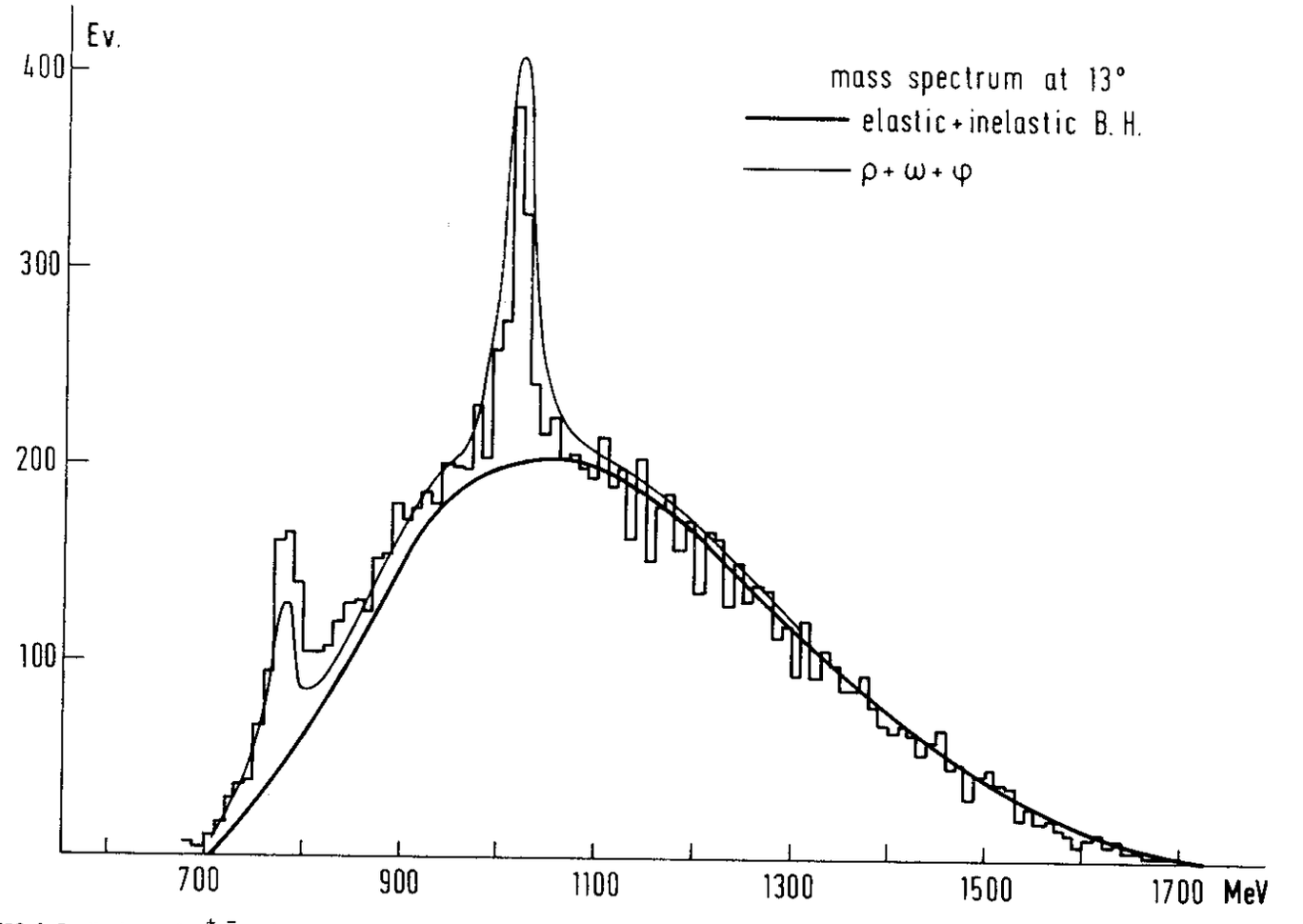

FIG.2.7 Number of e^+e^- pairs as a function of invariant mass at 13°. The contributions from Bethe-Heitler graphs alone and from the ρ+ω and the φ peaks are shown by heavy and light curves.

FIG. 2.10 Number of e^+e^- pairs as a function of invariant mass of 19°.

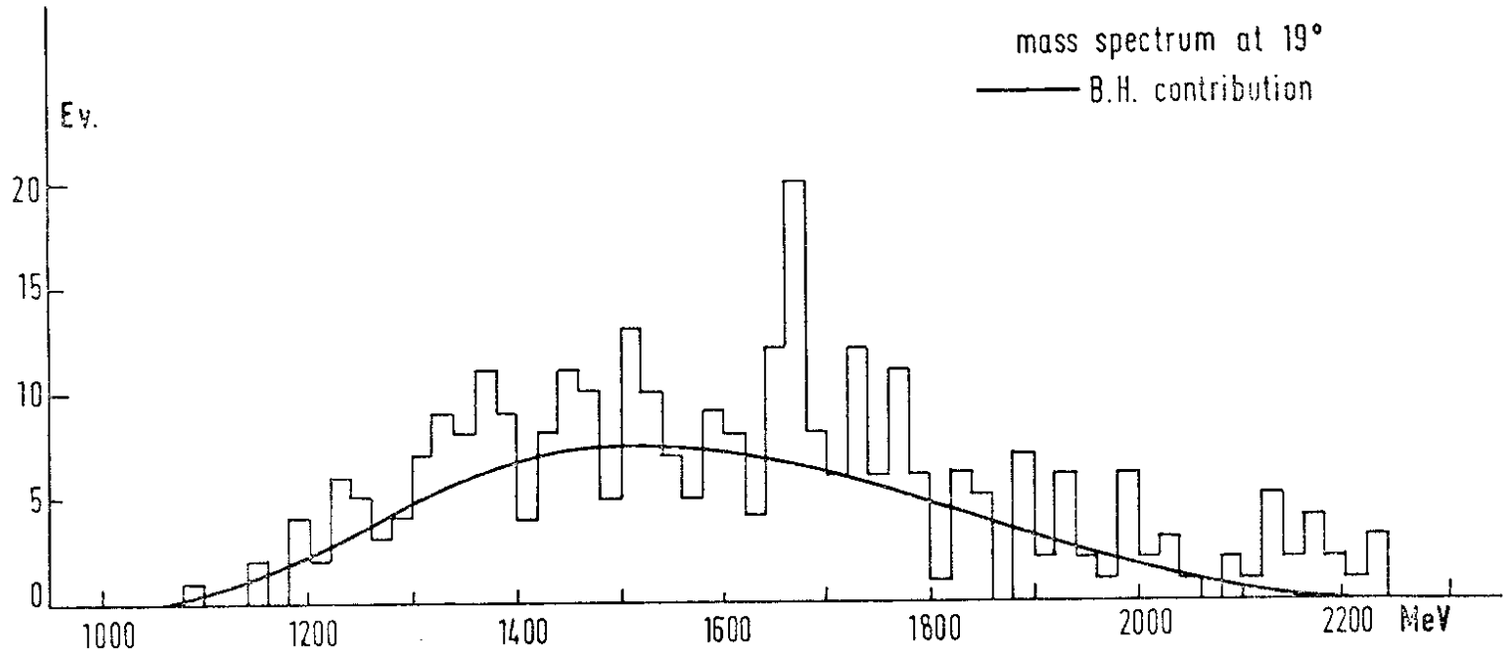

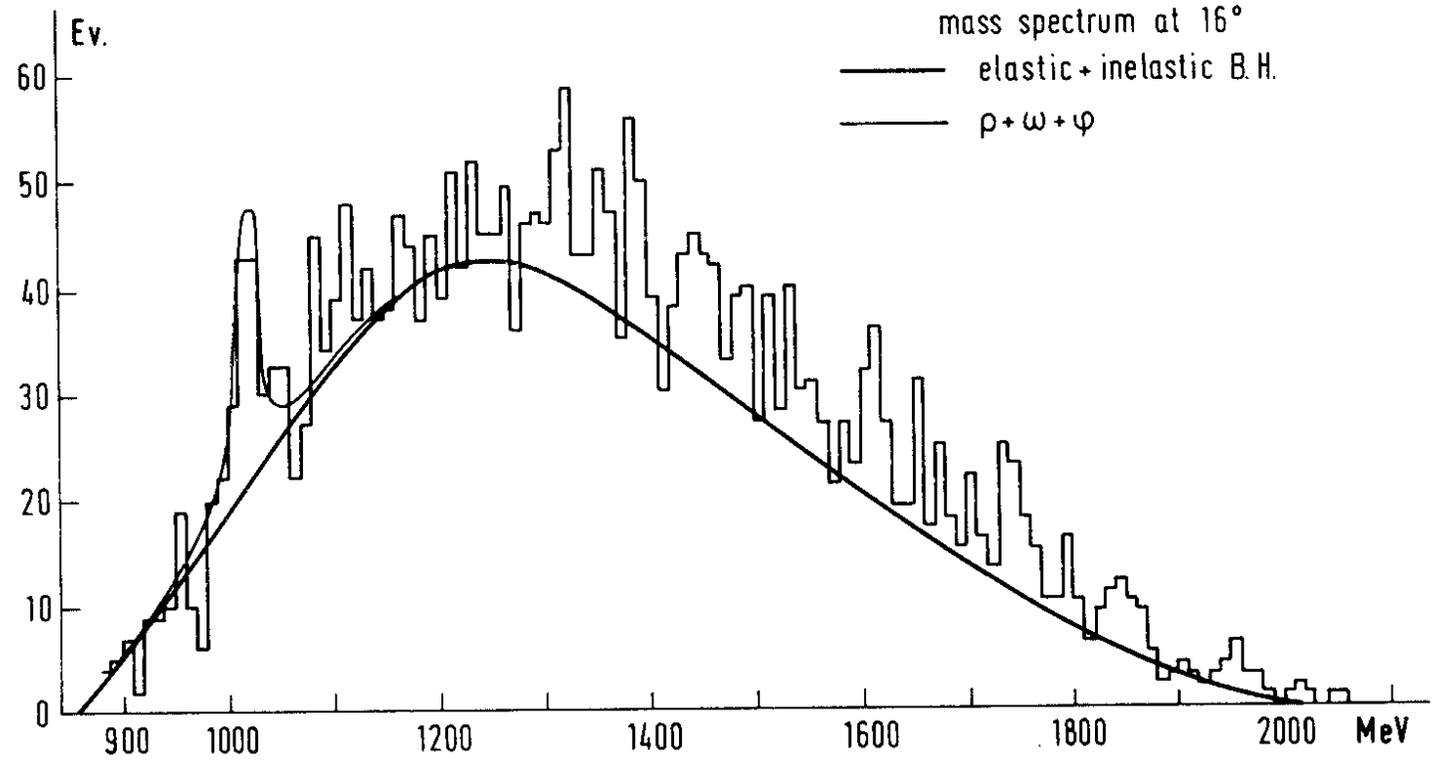

FIG. 2.9 Number of e^+e^- pairs as a function of invariant mass of 16°.

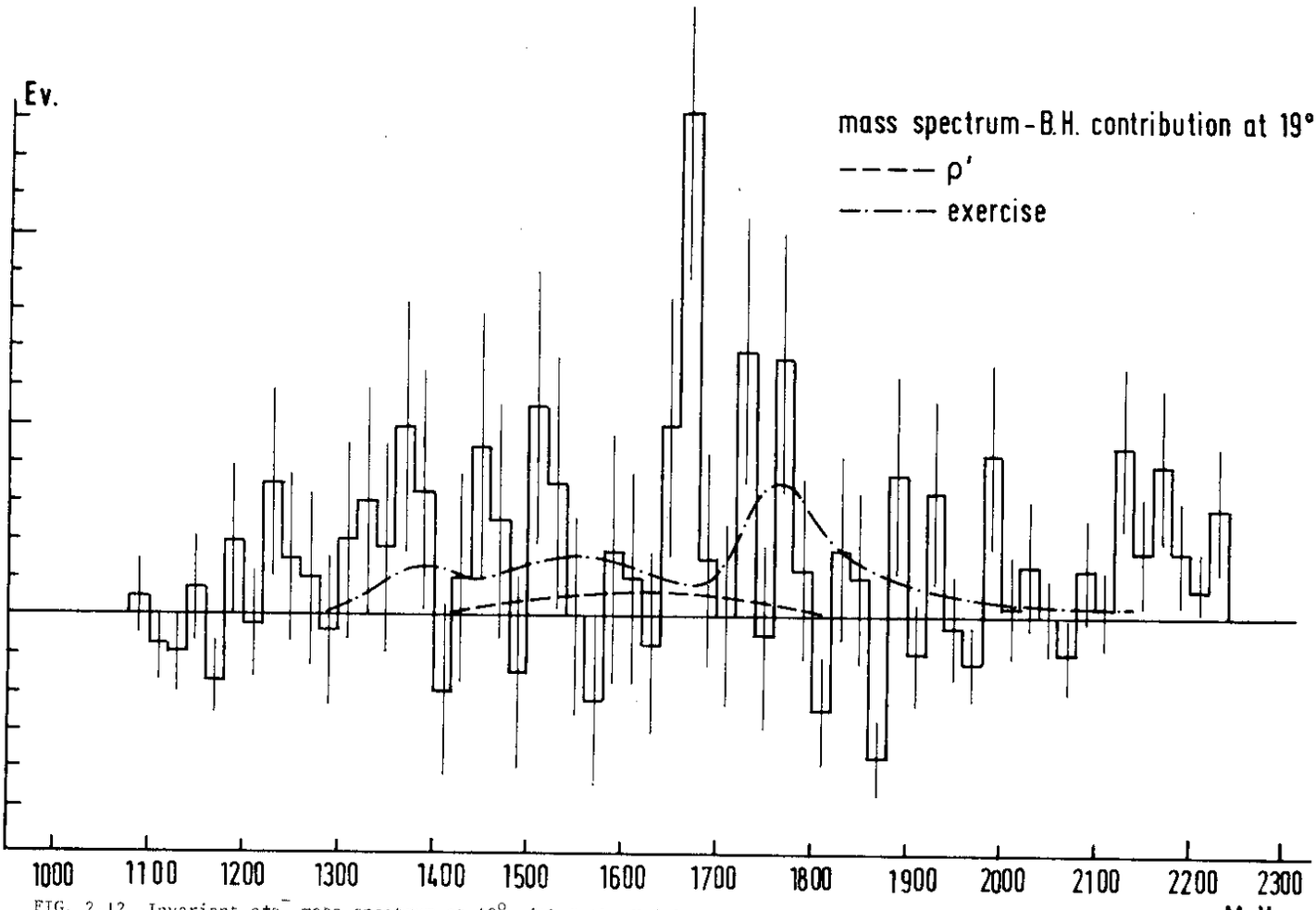

FIG. 2.12 Invariant e^+e^- mass spectrum at 19° with Bethe-Heitler contribution subtracted.

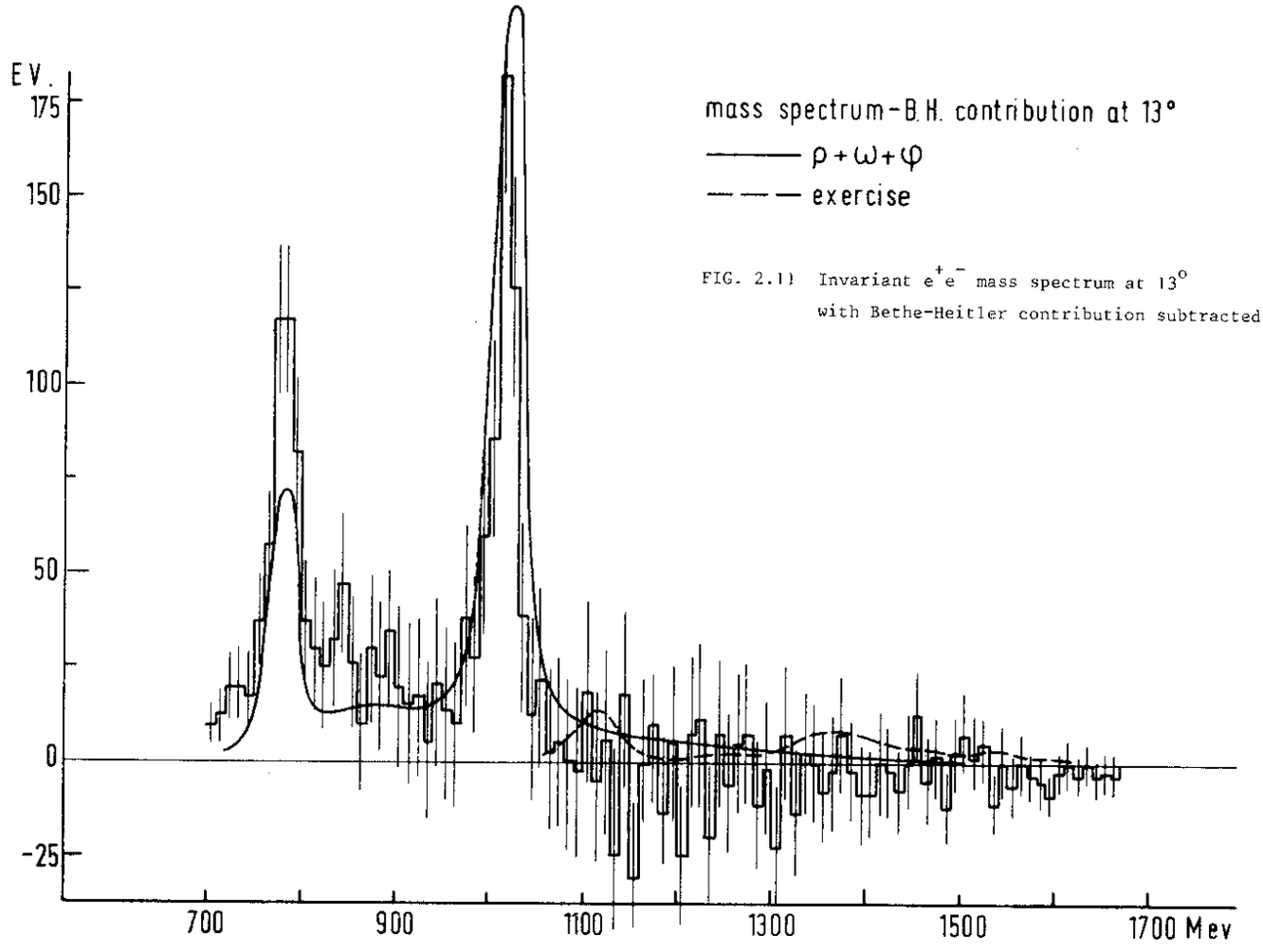

FIG. 2.11 Invariant e^+e^- mass spectrum at 13° with Bethe-Heitler contribution subtracted.

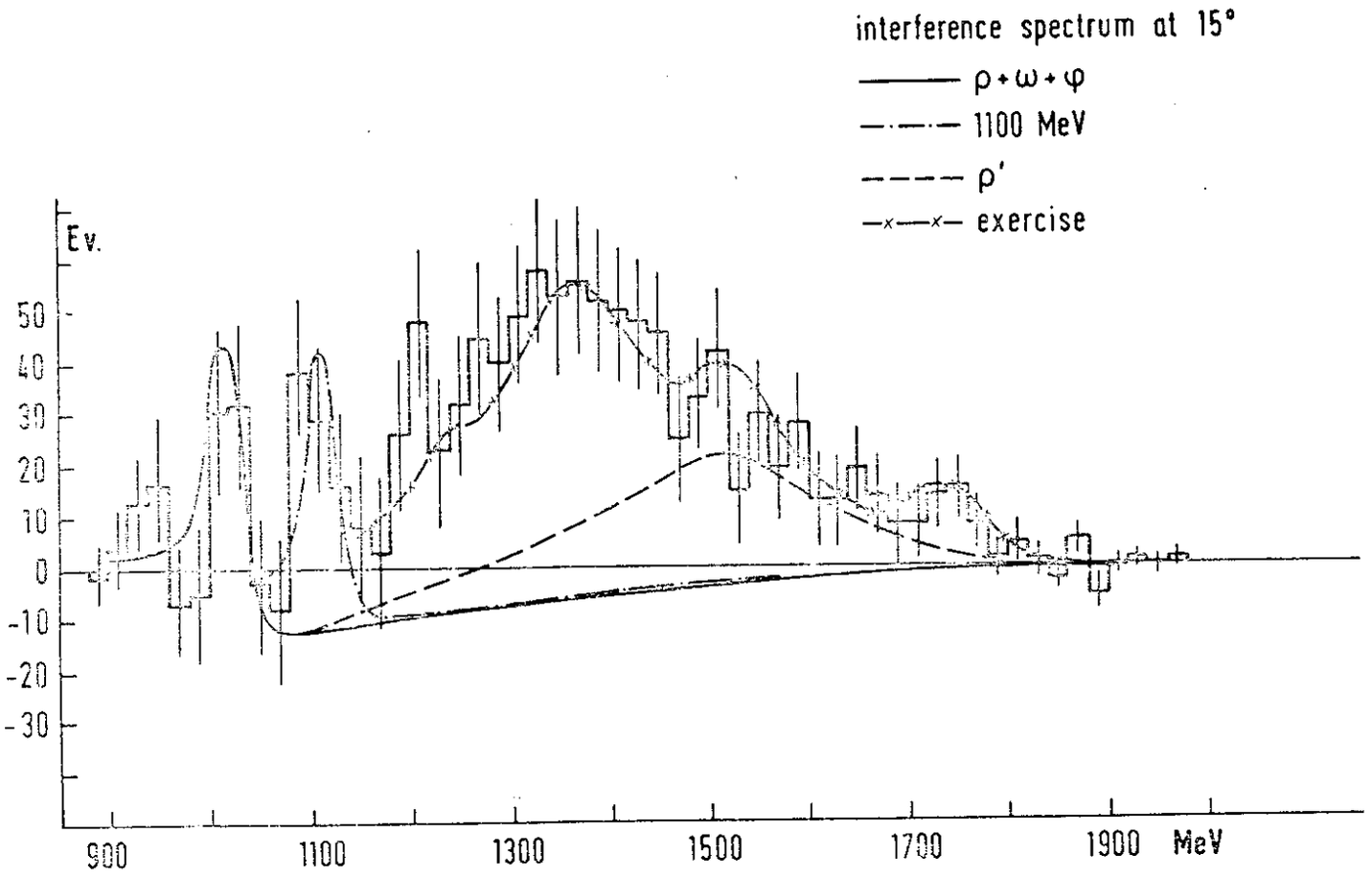

FIG. 2.14 Interference term between Bethe-Heitler and Compton production of e^+e^- pairs observed at 15°.

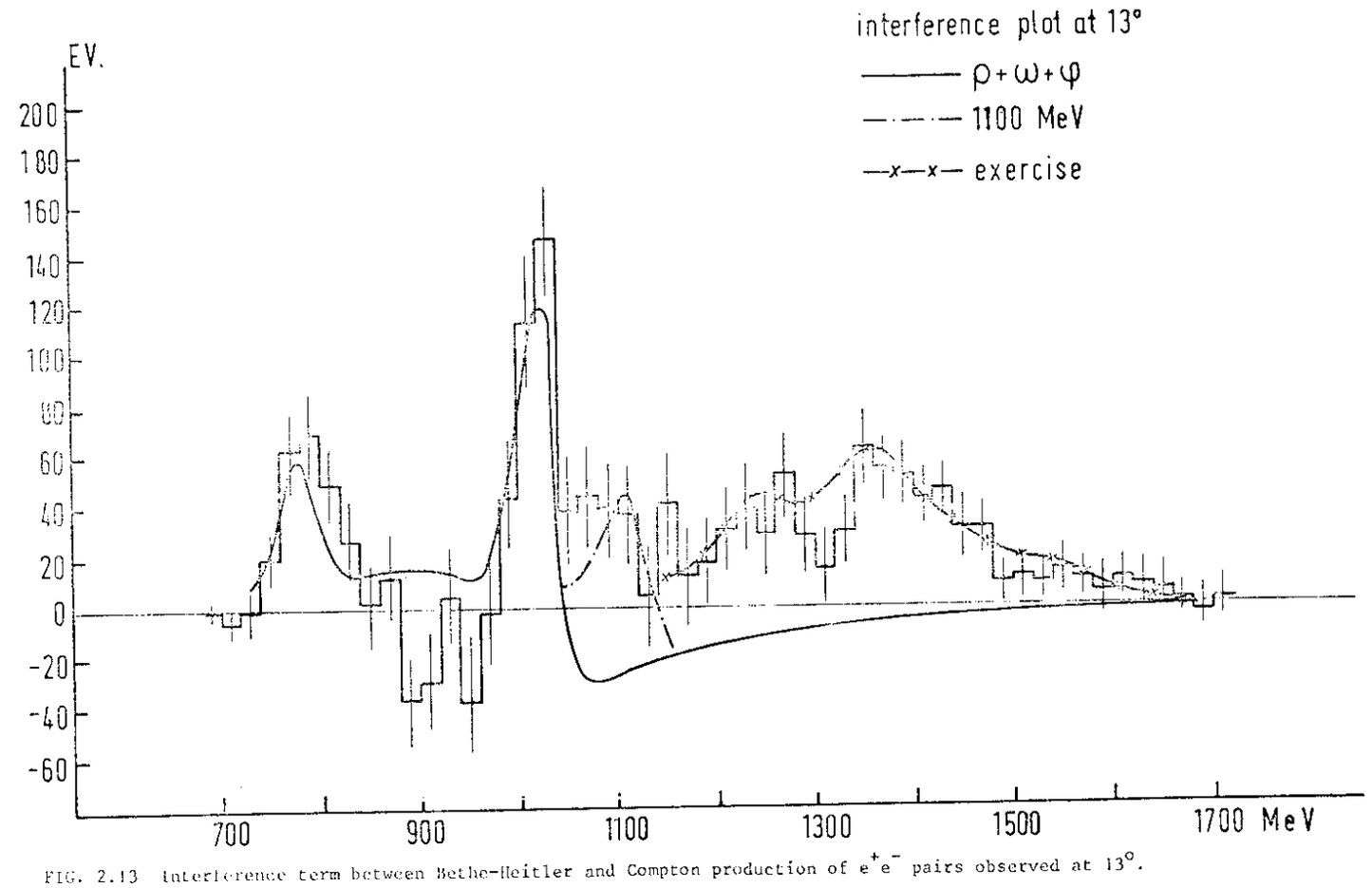

FIG. 2.13 Interference term between Bethe-Heitler and Compton production of e^+e^- pairs observed at 13°.

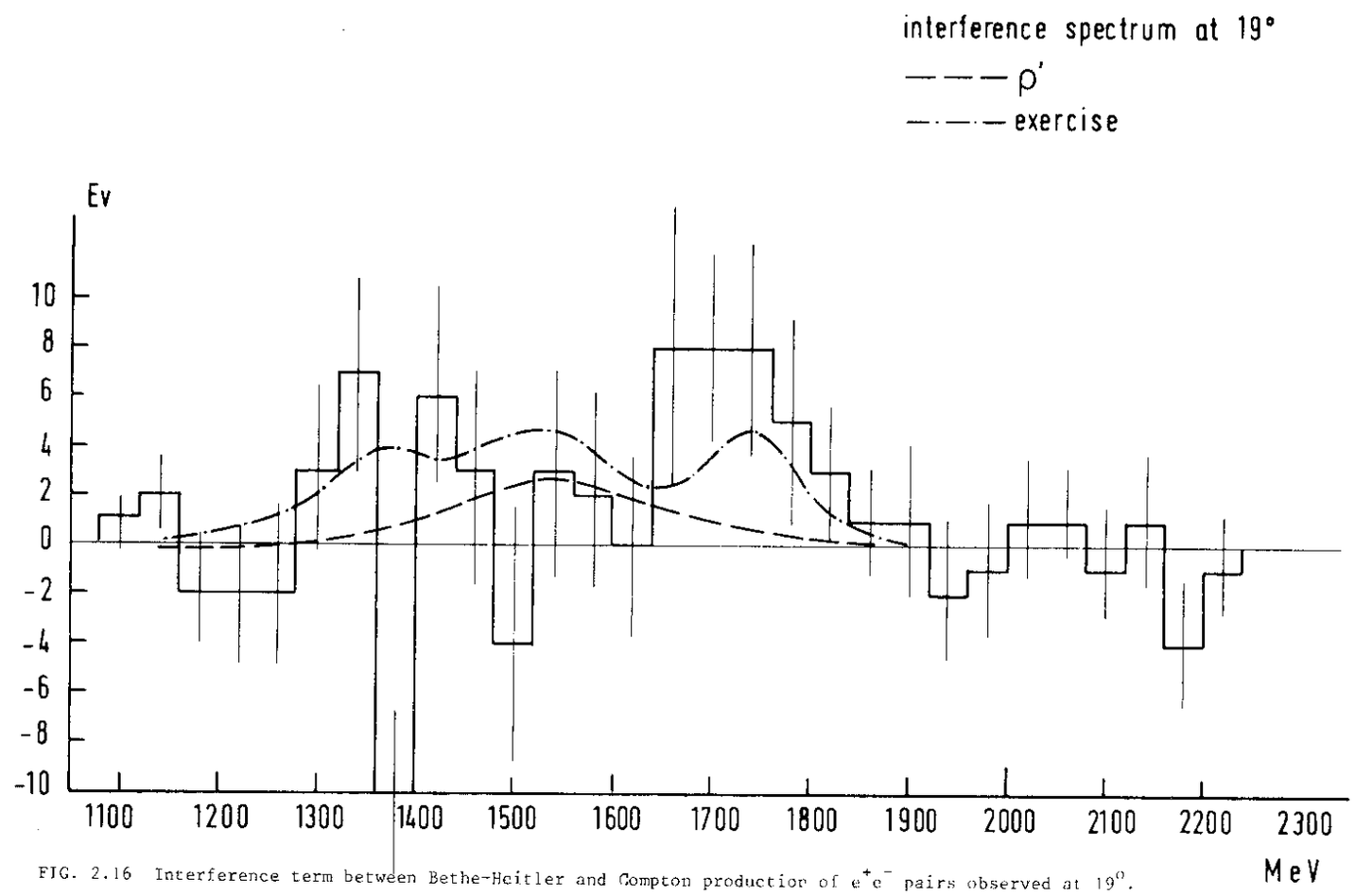

FIG. 2.16 Interference term between Bethe-Heitler and Compton production of e^+e^- pairs observed at 19^o.

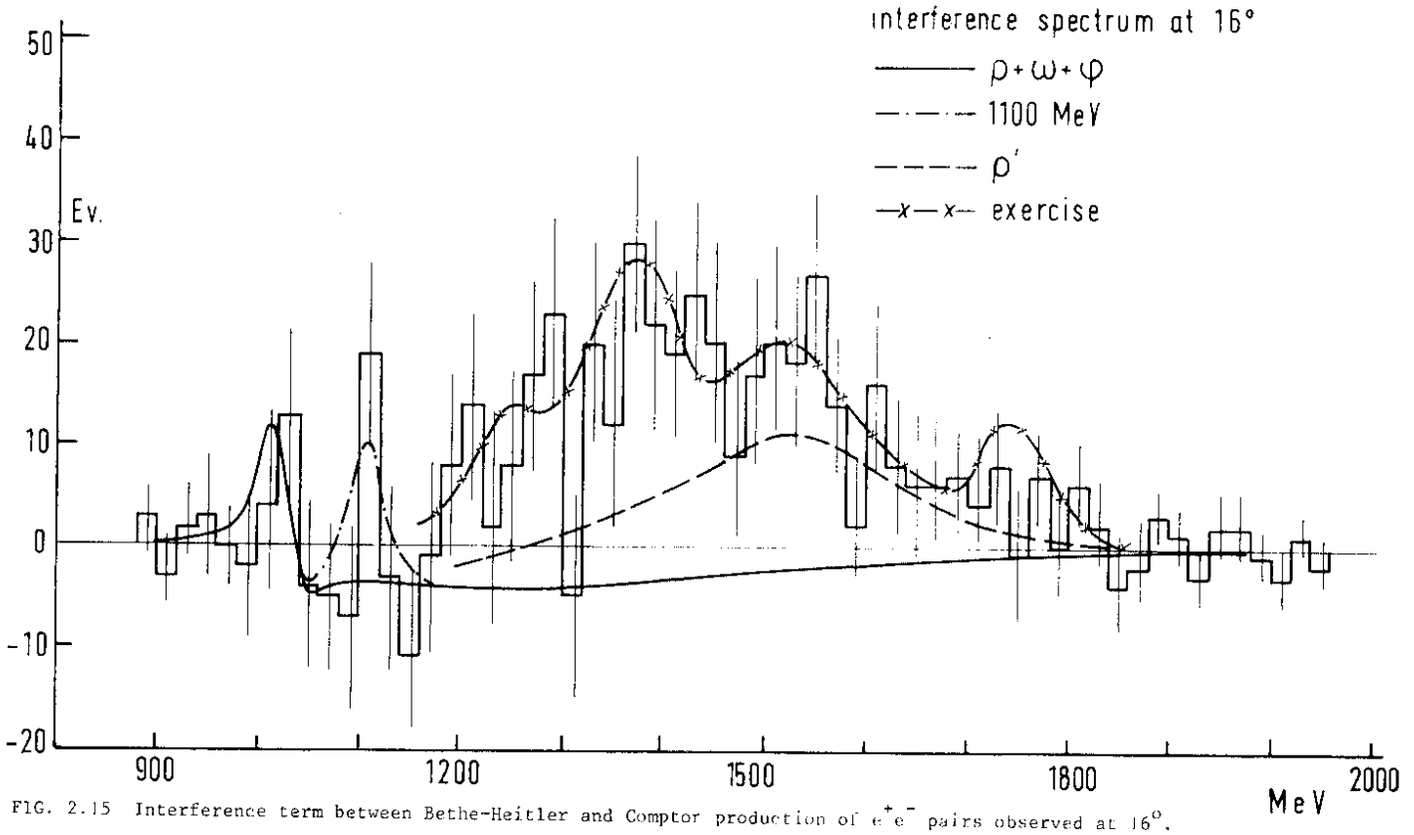

FIG. 2.15 Interference term between Bethe-Heitler and Comptor production of e^+e^- pairs observed at 16^o.

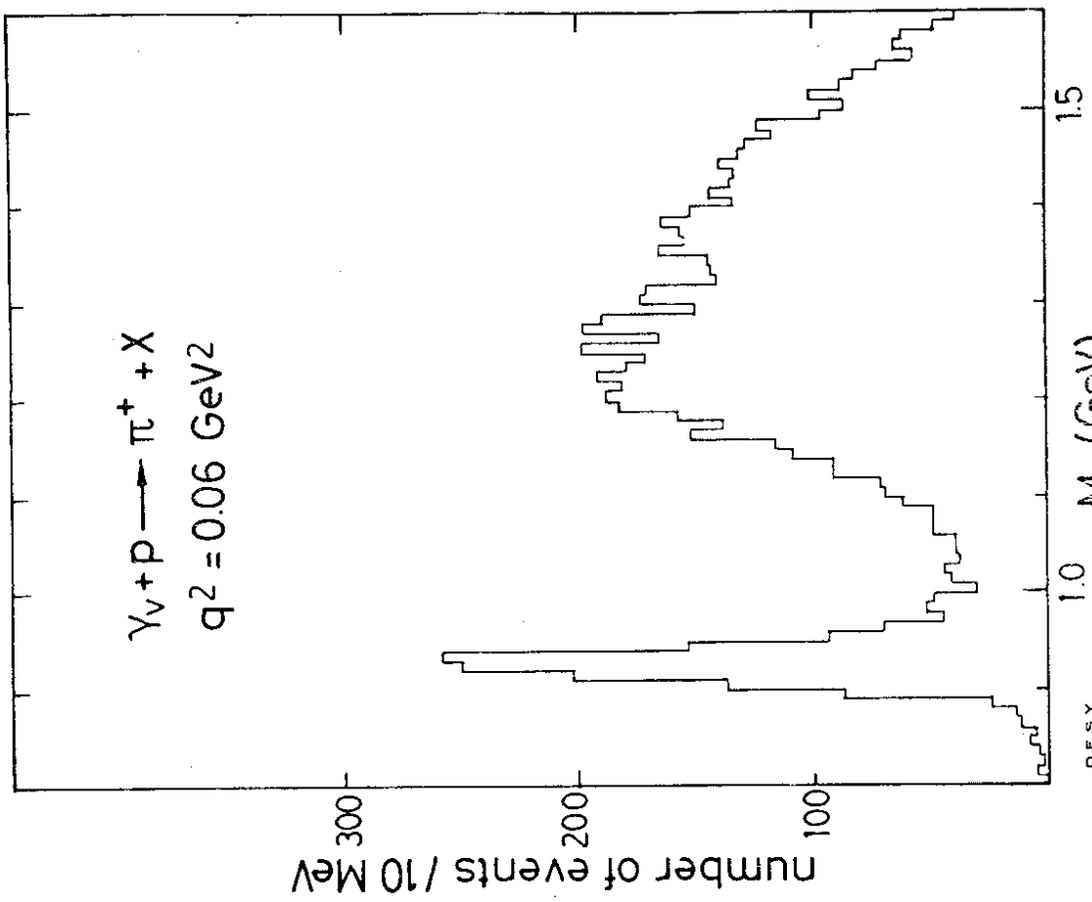

FIG. 2.18 Missing mass plot for electroproduction of π^+.

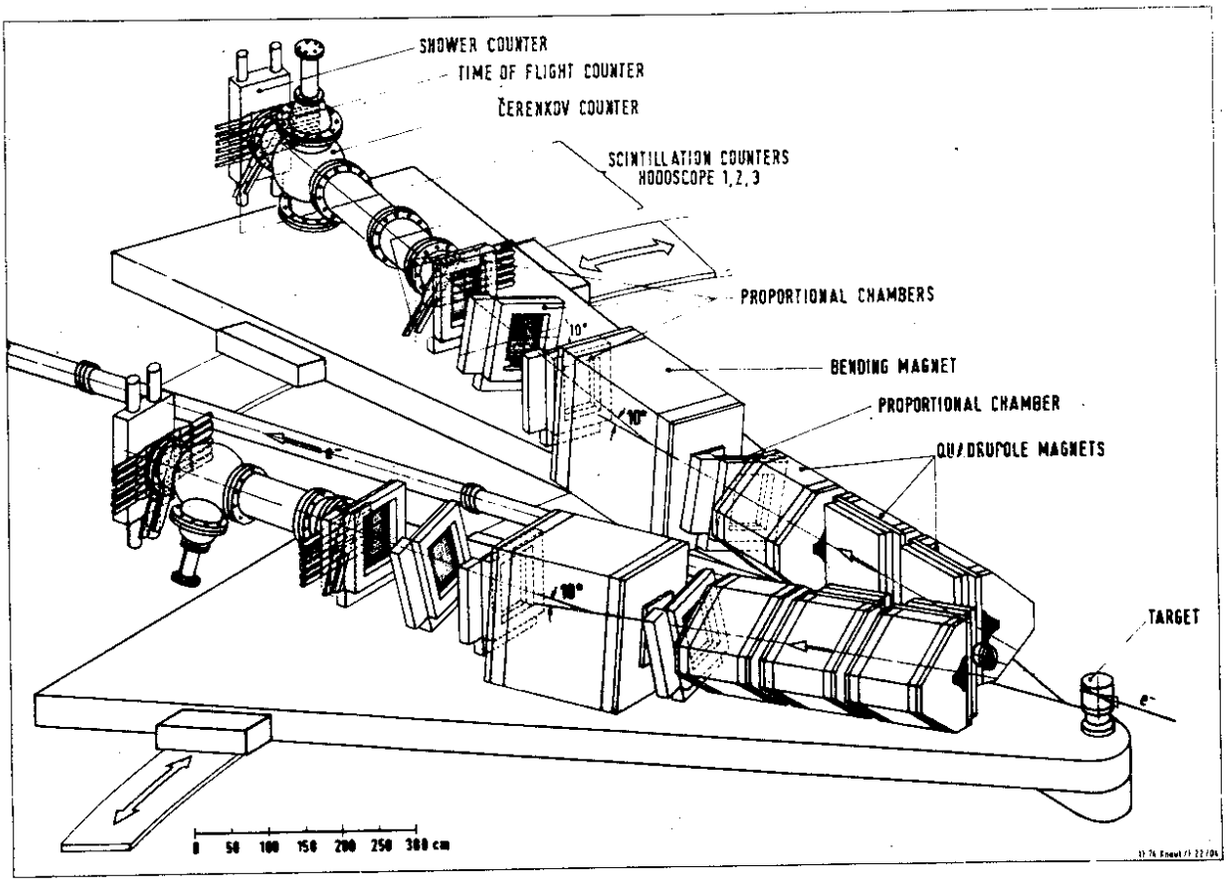

FIG. 2.17 Experimental set-up for electroproduction of charged pions.

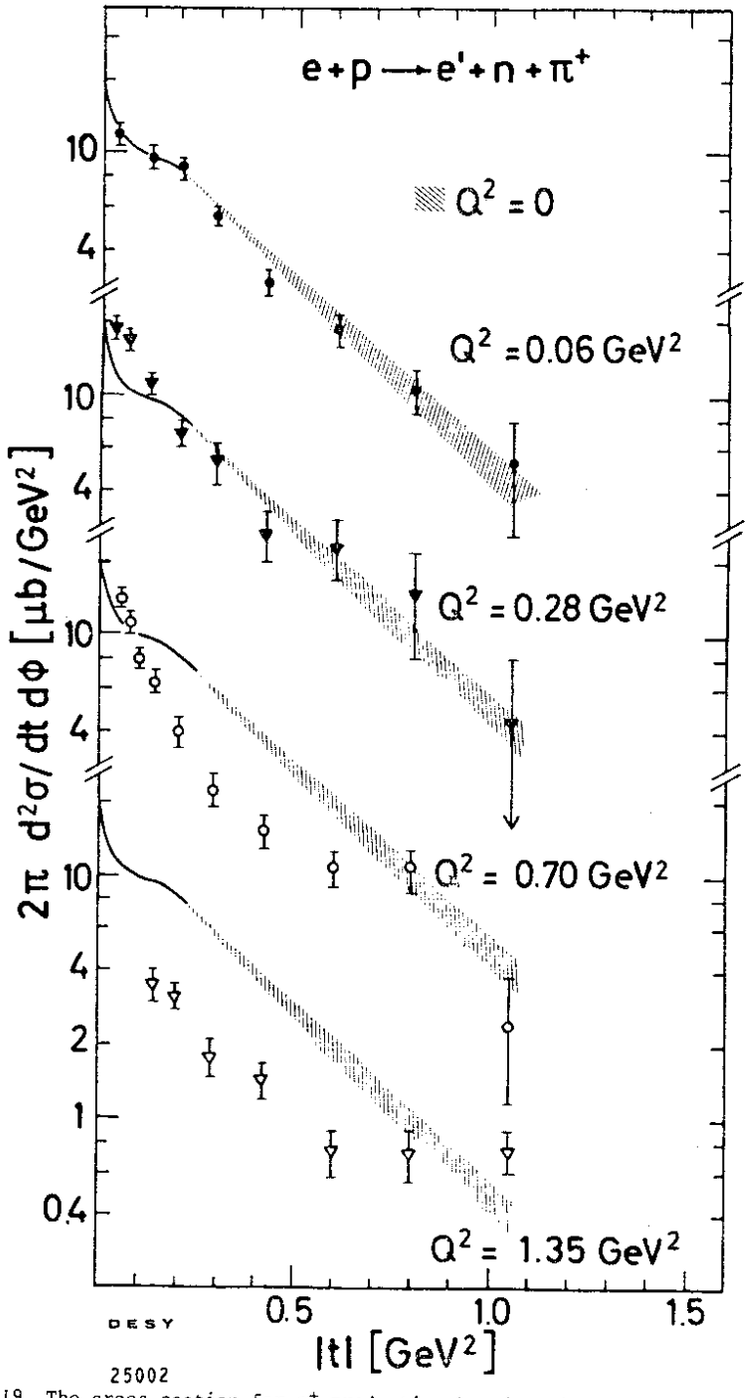

FIG. 2.19 The cross section for π^+ production by virtual photons versus $|t|$ for four different values of Q^2.

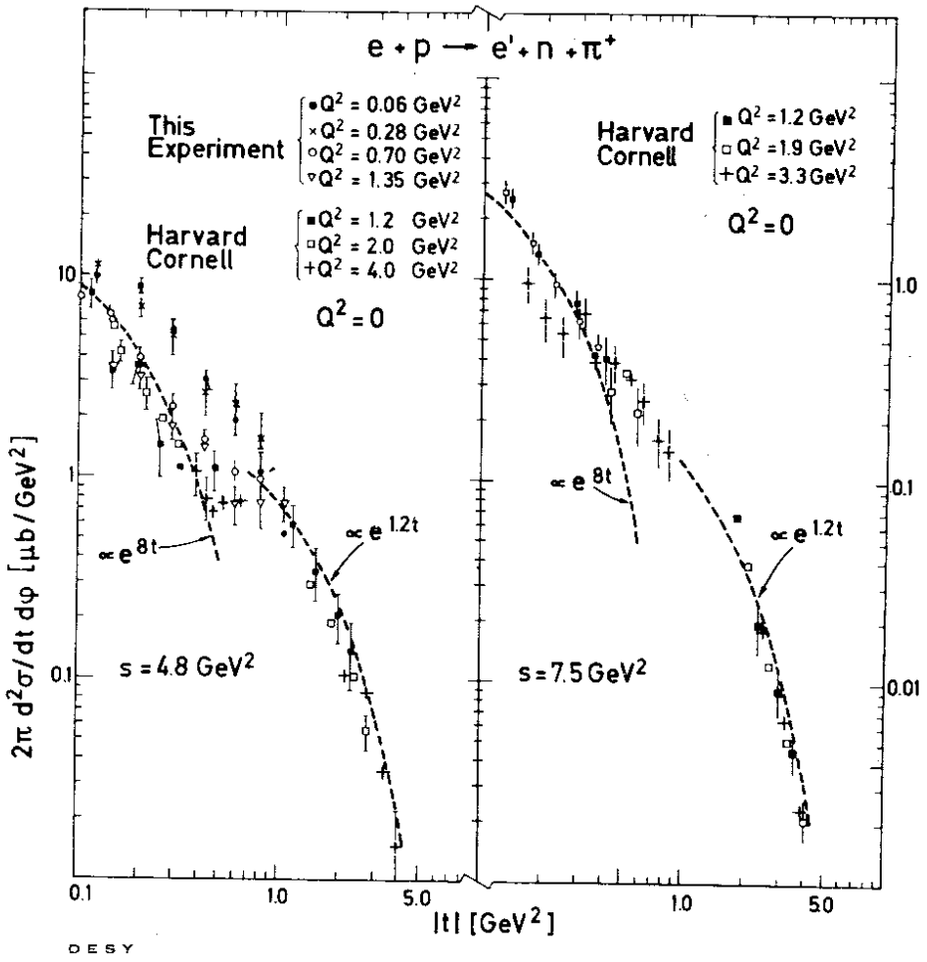

FIG. 2.20 The data of Fig.2.19 together with those of the Cornell-Harvard group. Error bars are only plotted at some representative points.

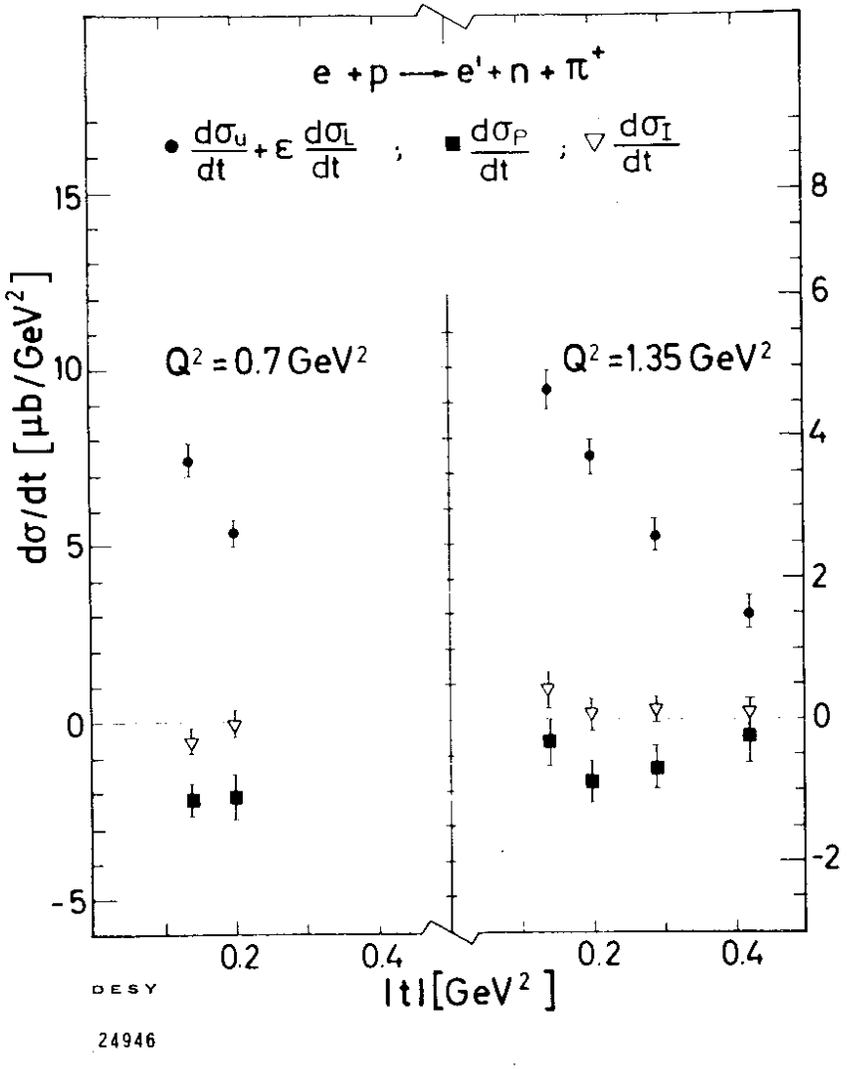

FIG. 2.21 The t dependence of $d\sigma_U/dt + \varepsilon\, d\sigma_L/dt$, $d\sigma_I/dt$, and $d\sigma_P/dt$ for $\gamma_v p \to \pi^+ n$.

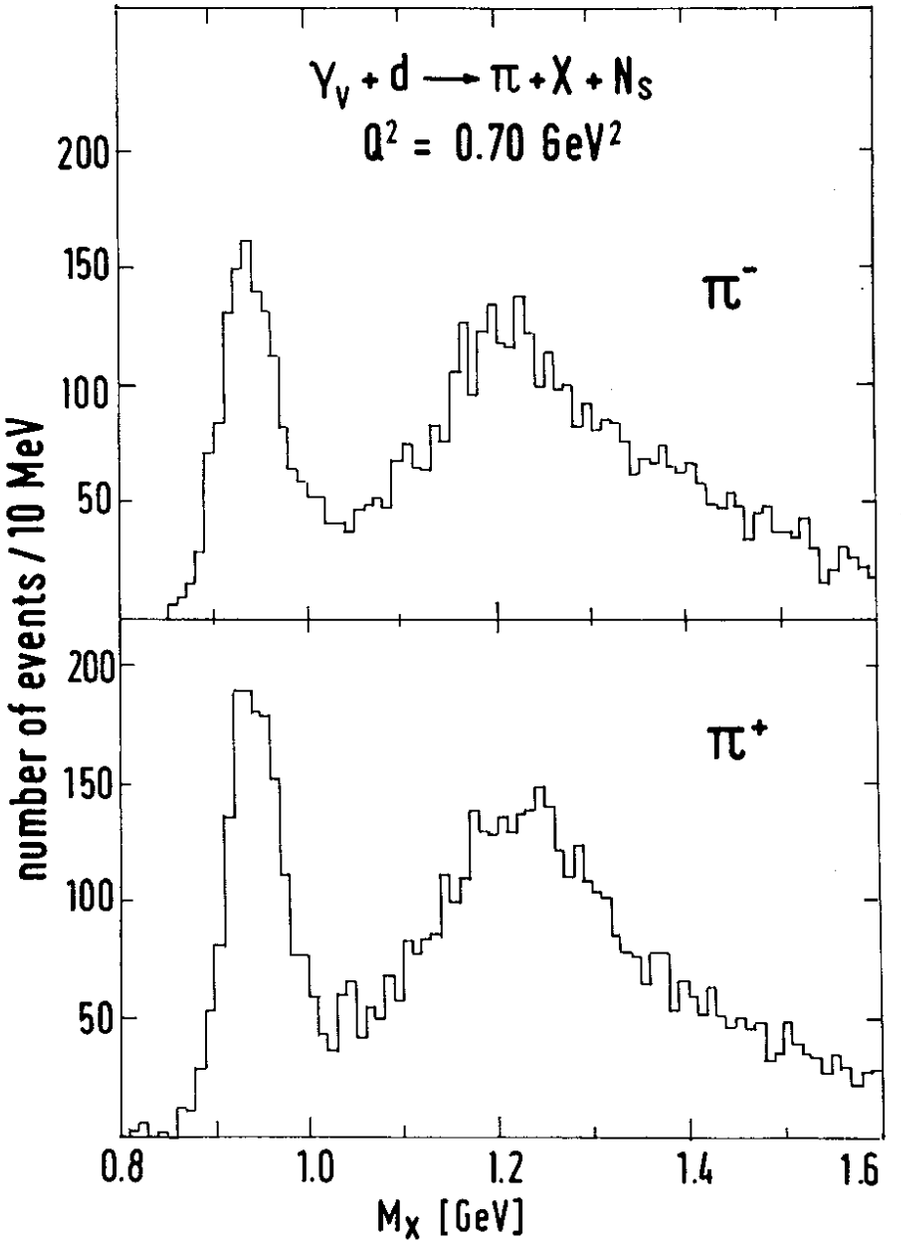

FIG. 2.22 Missing mass spectra for virtual photoproduction of π^- and π^+ off the deuteron.

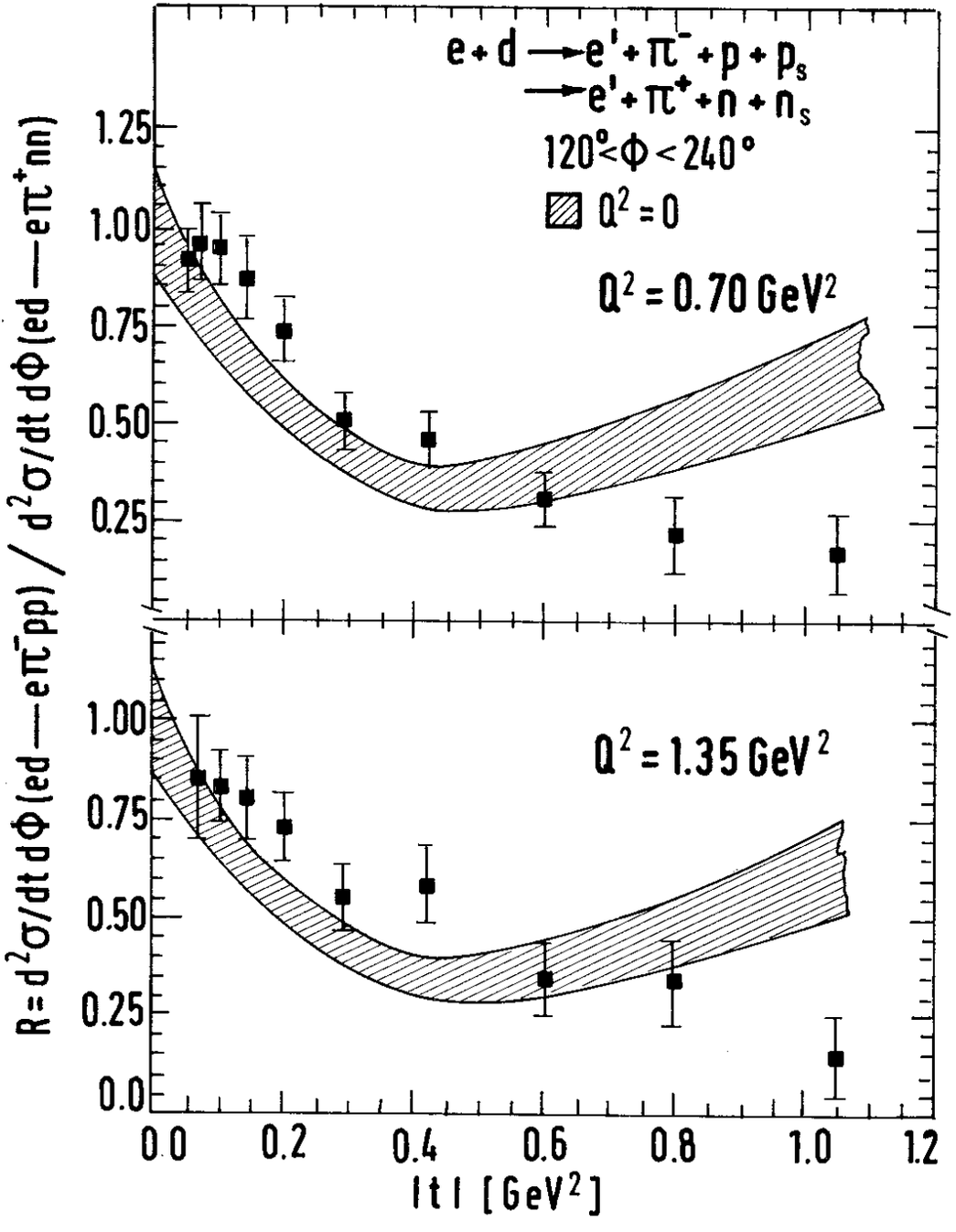

FIG. 2.23 The ratio of cross sections for elastic π^- and π^+ production versus $|t|$ for two values of Q^2.

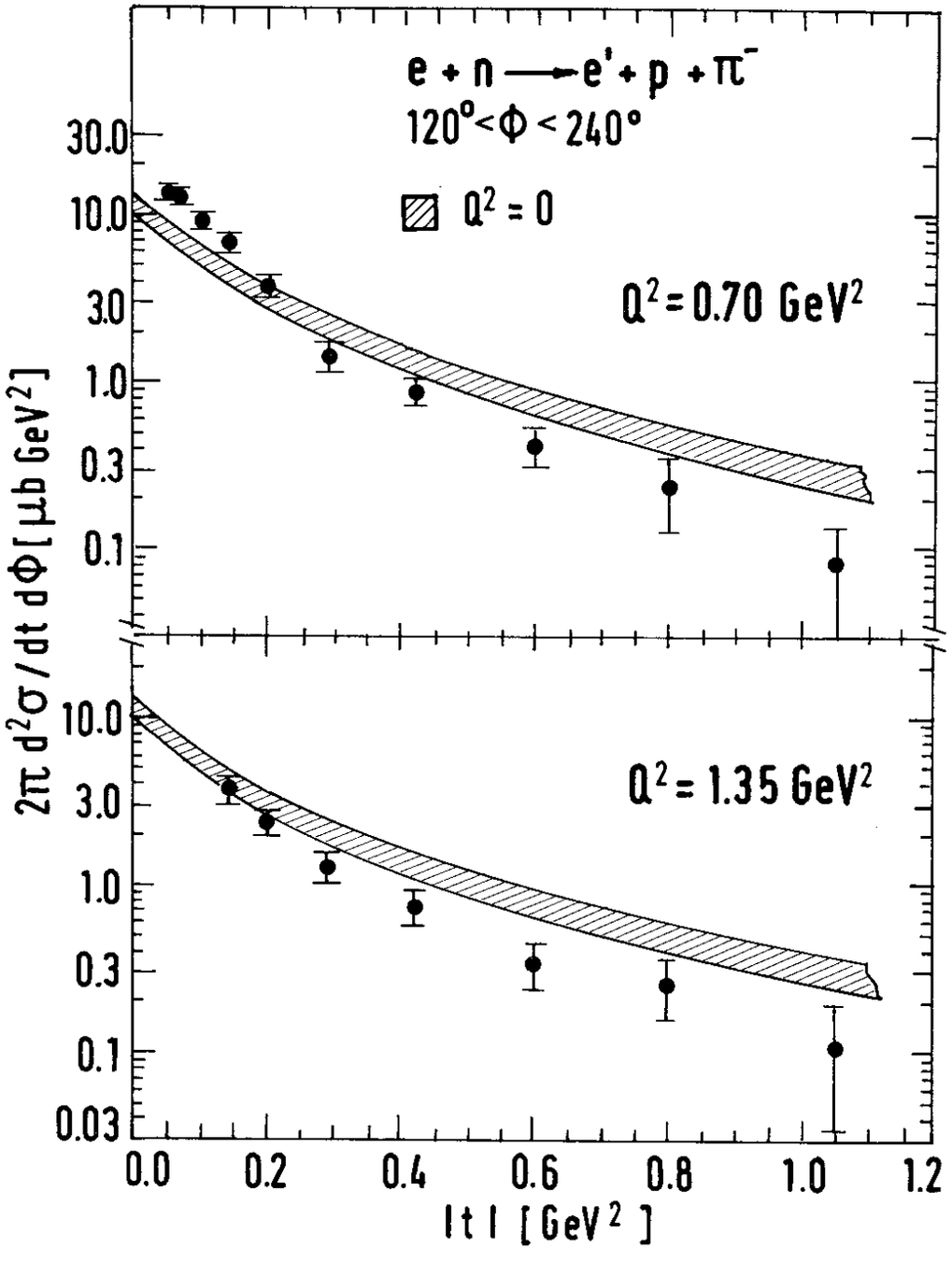

FIG. 2.24 The differential cross section for π^- production for two values of Q^2.

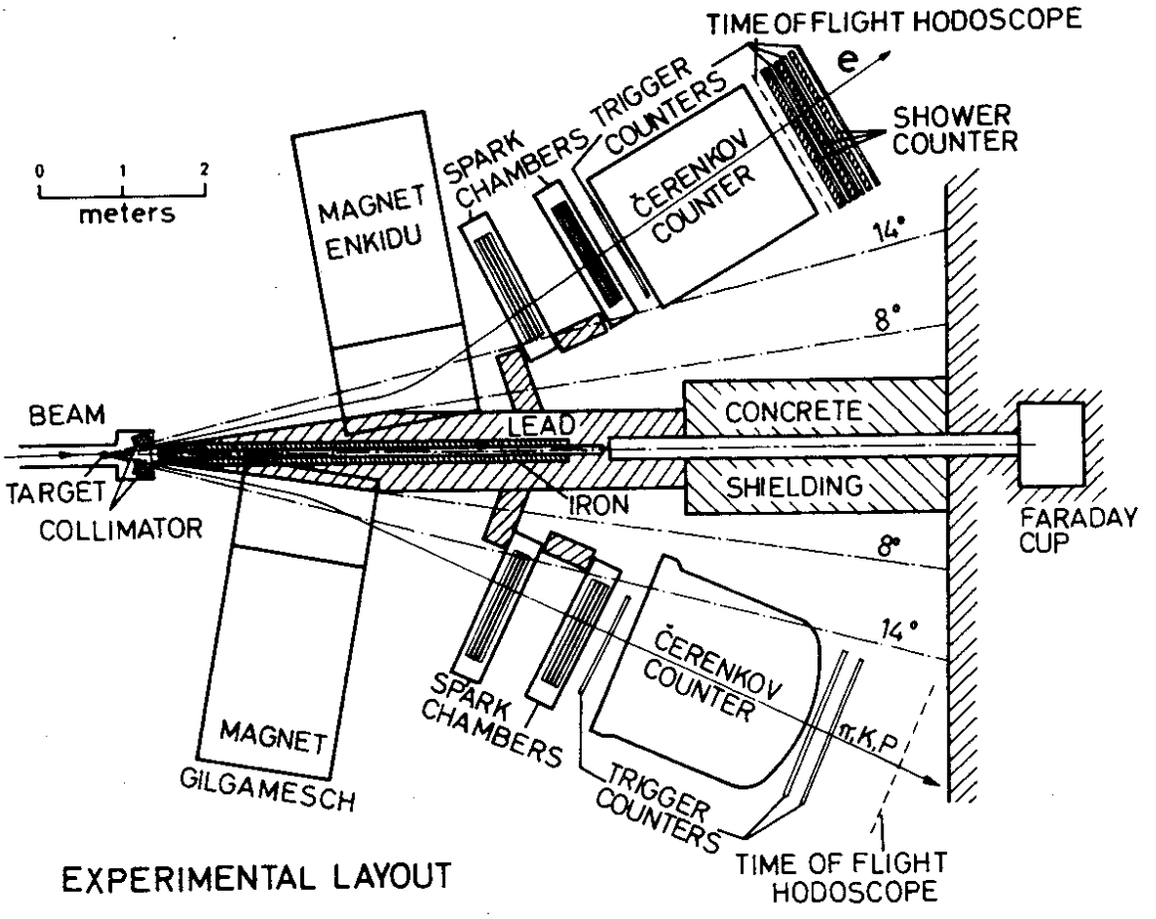

FIG. 2.26 Experimental arrangement for studying inclusive electroproduction of protons and π^+ mesons.

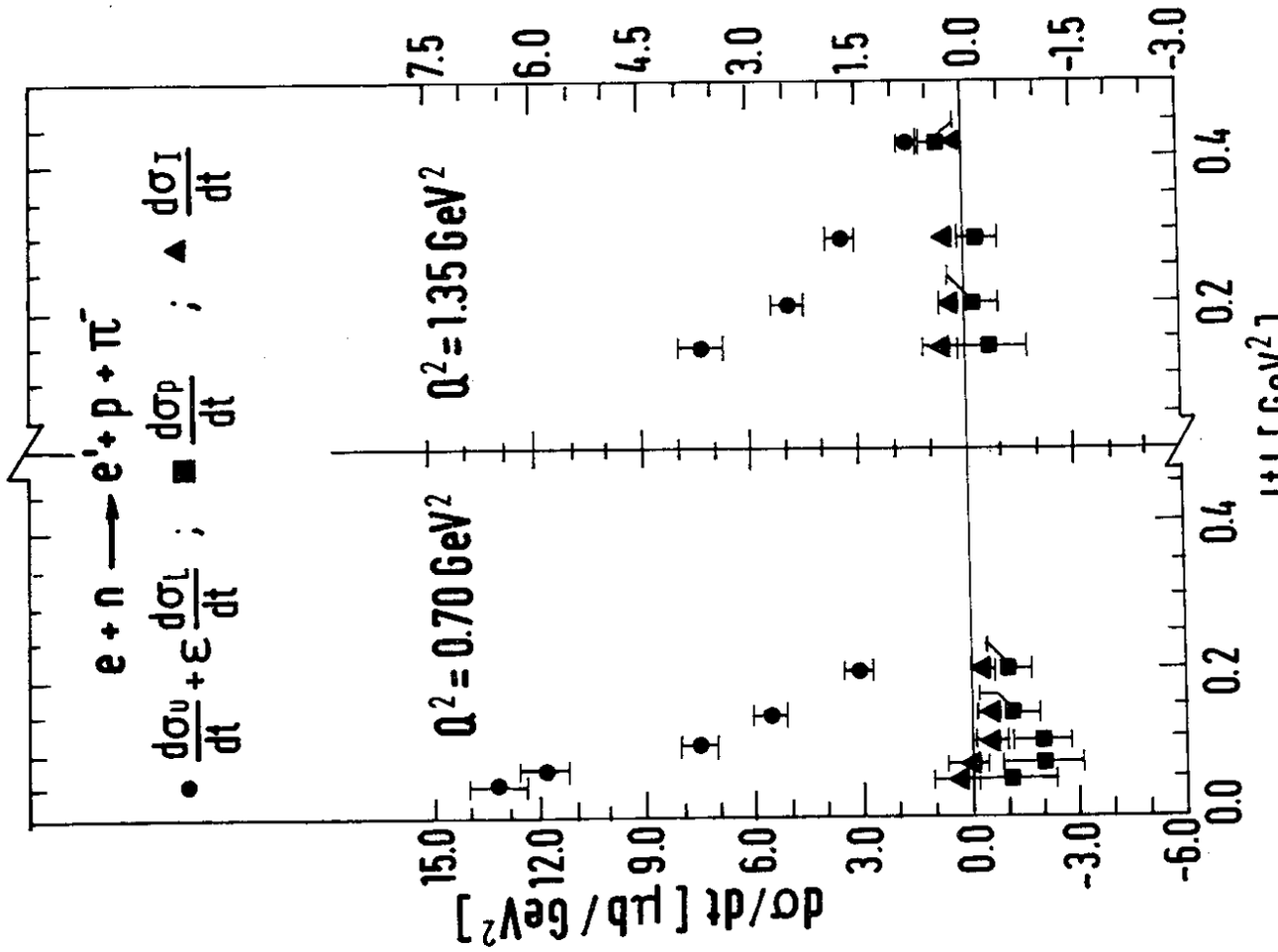

FIG. 2.25 The cross section components $d\sigma_U/dt + \varepsilon\, d\sigma_L/dt$, $d\sigma_L/dt$, and $d\sigma_p/dt$ for $\gamma_v n \to \pi^- p$.

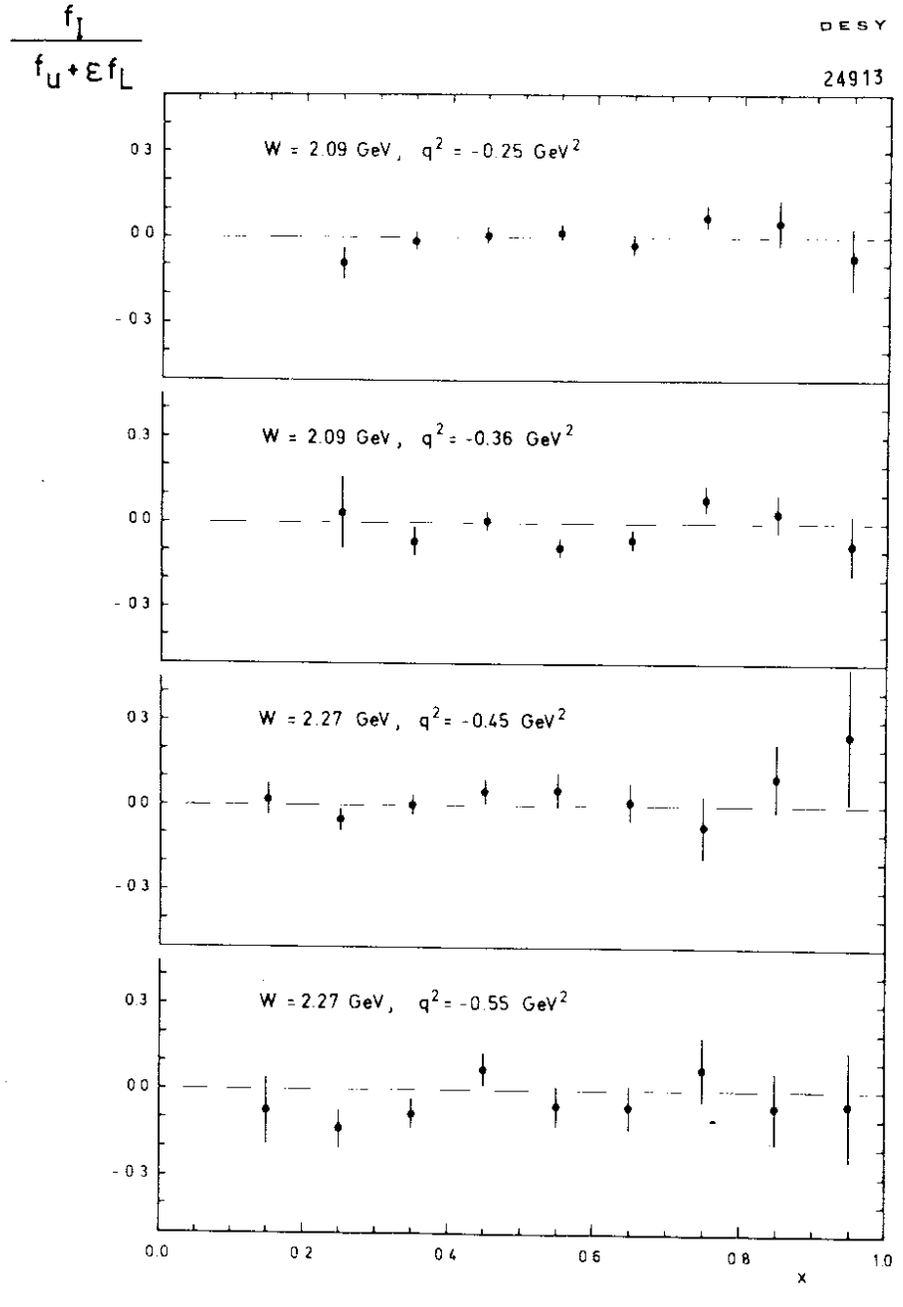

FIG. 2.27 x distribution of $f_I/(f_U + \varepsilon f_L)$ in inclusive electroproduction of protons.

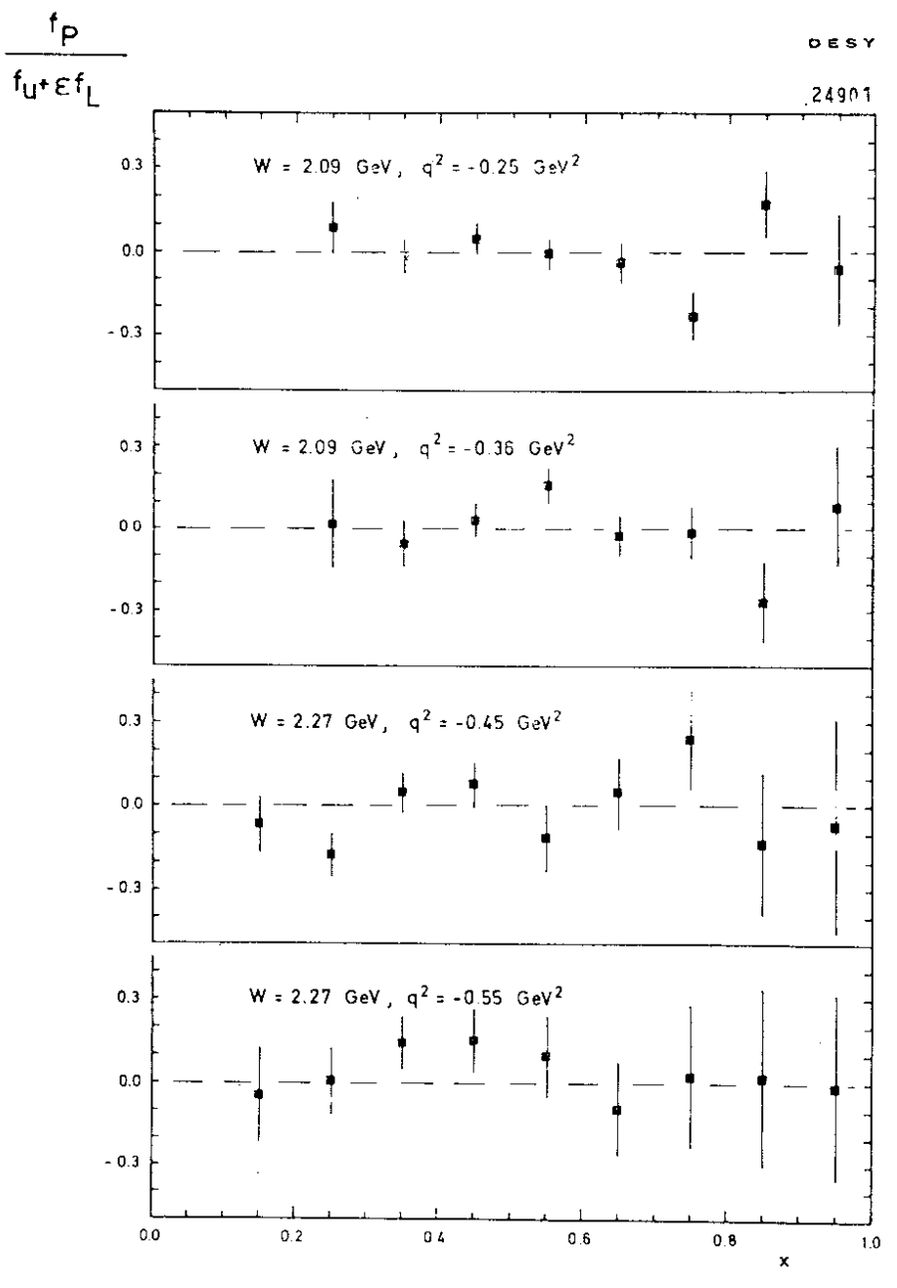

FIG. 2.28 x distribution of $f_P/(f_U + \varepsilon f_L)$ in inclusive electroproduction of protons.

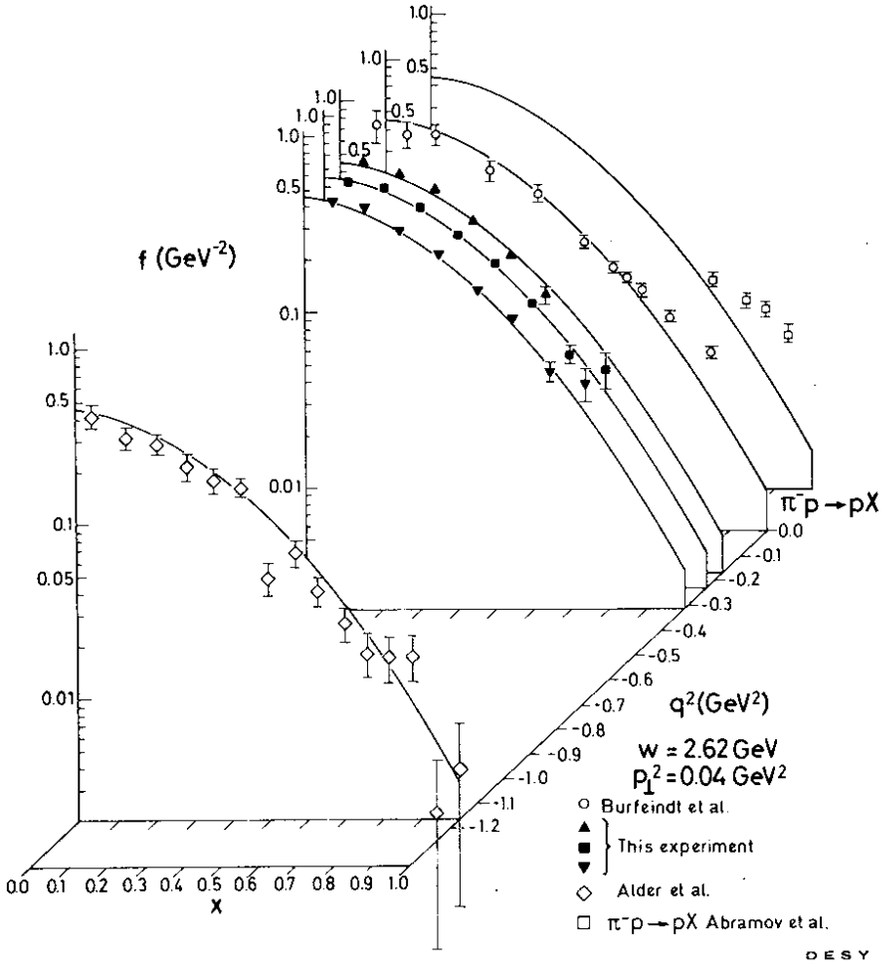

FIG. 2.29 x distribution of f for W = 2.62.

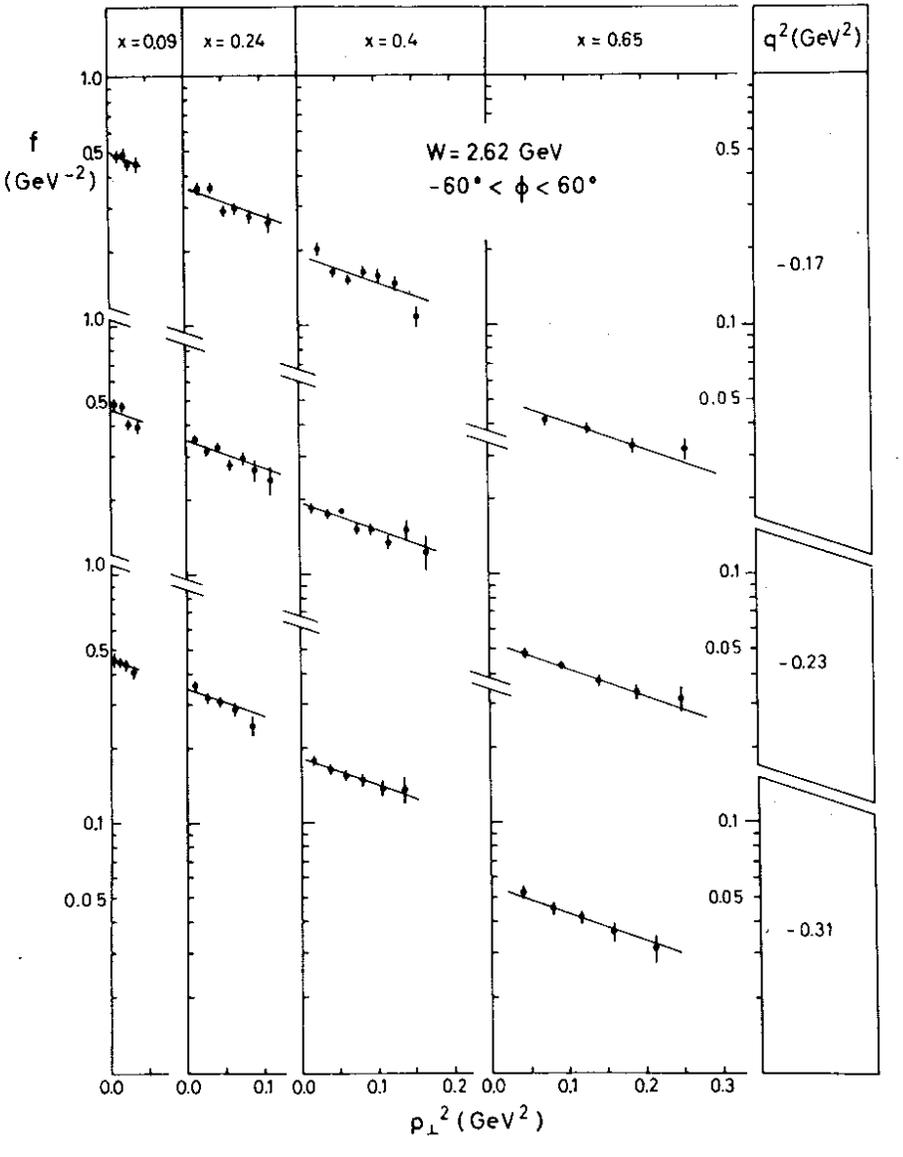

FIG. 2.30 The dependence of f on $p_\perp^2$ for W = 2.62 GeV.

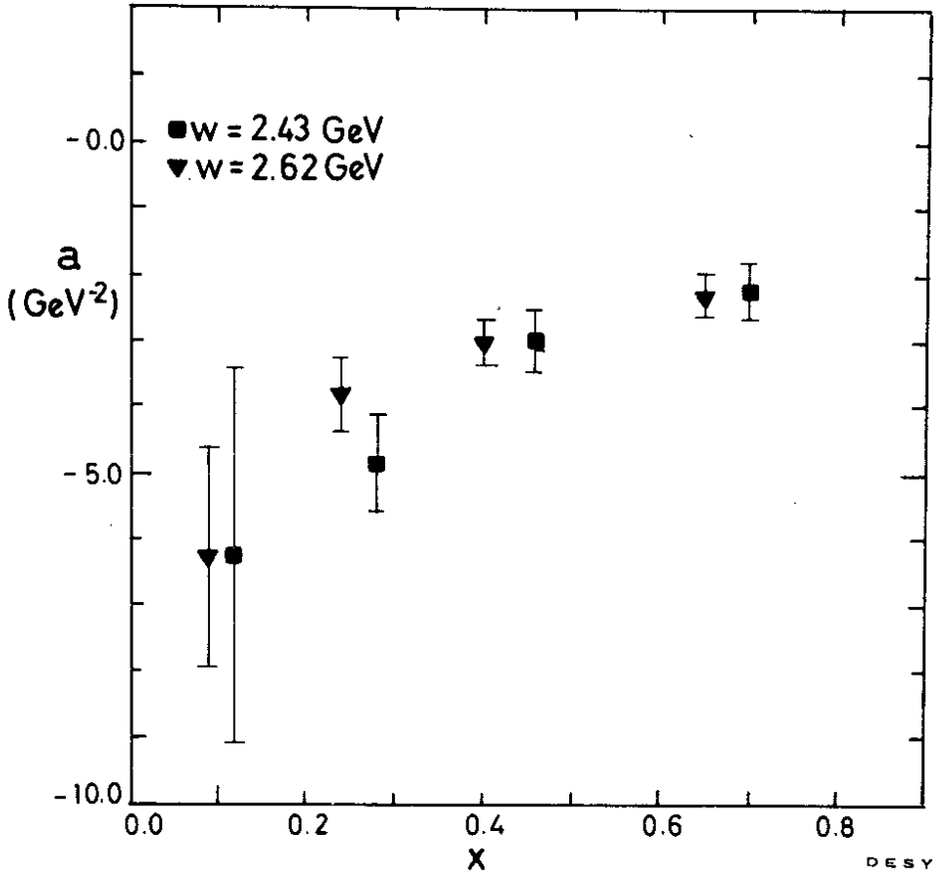

FIG. 2.31 The slope parameter a in $f = A \cdot \exp\{-a\, p_\perp^2\}$, averaged over Q^2 as a function of x.

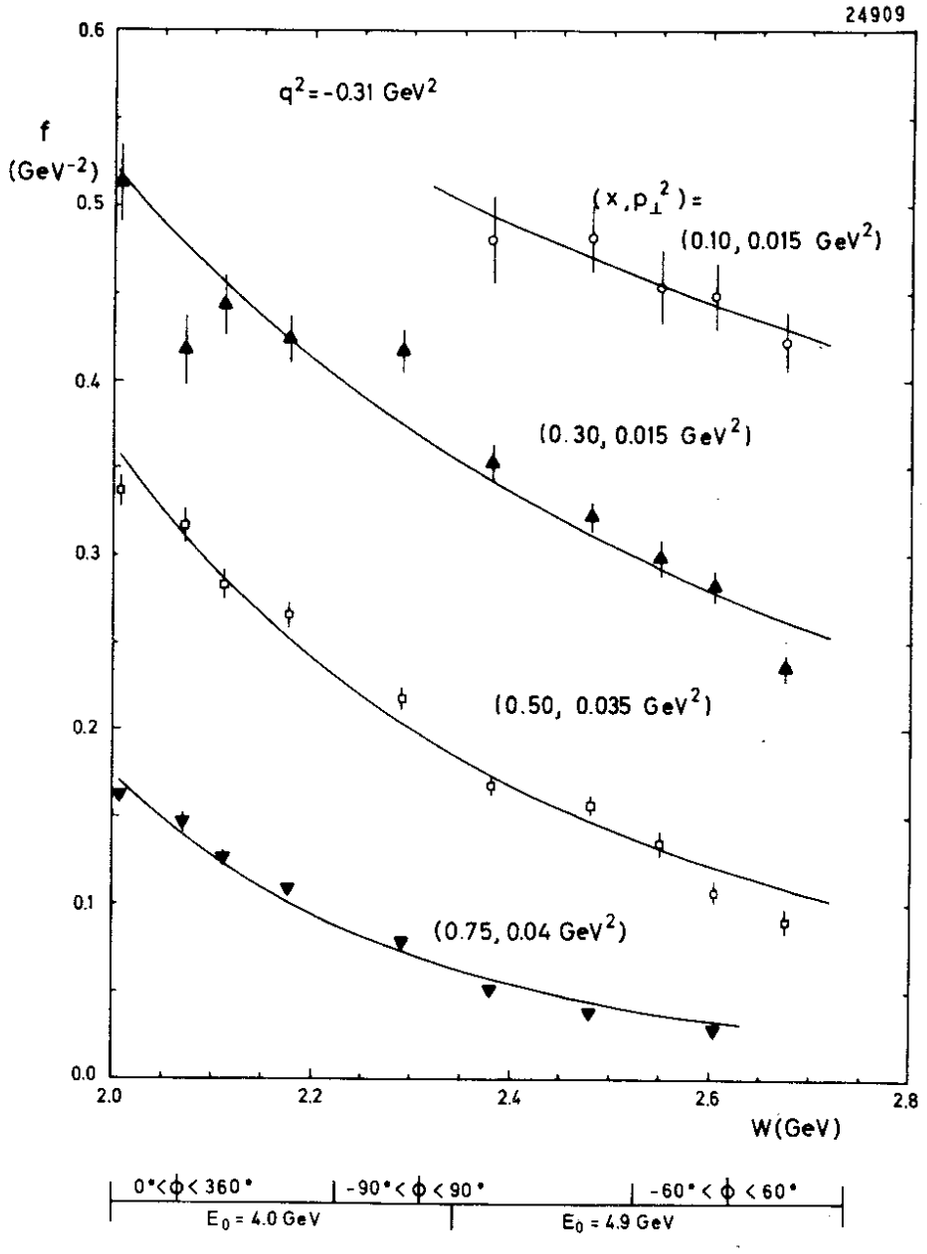

FIG. 2.32 W dependence of f for Q^2 = 0.31 GeV^2.

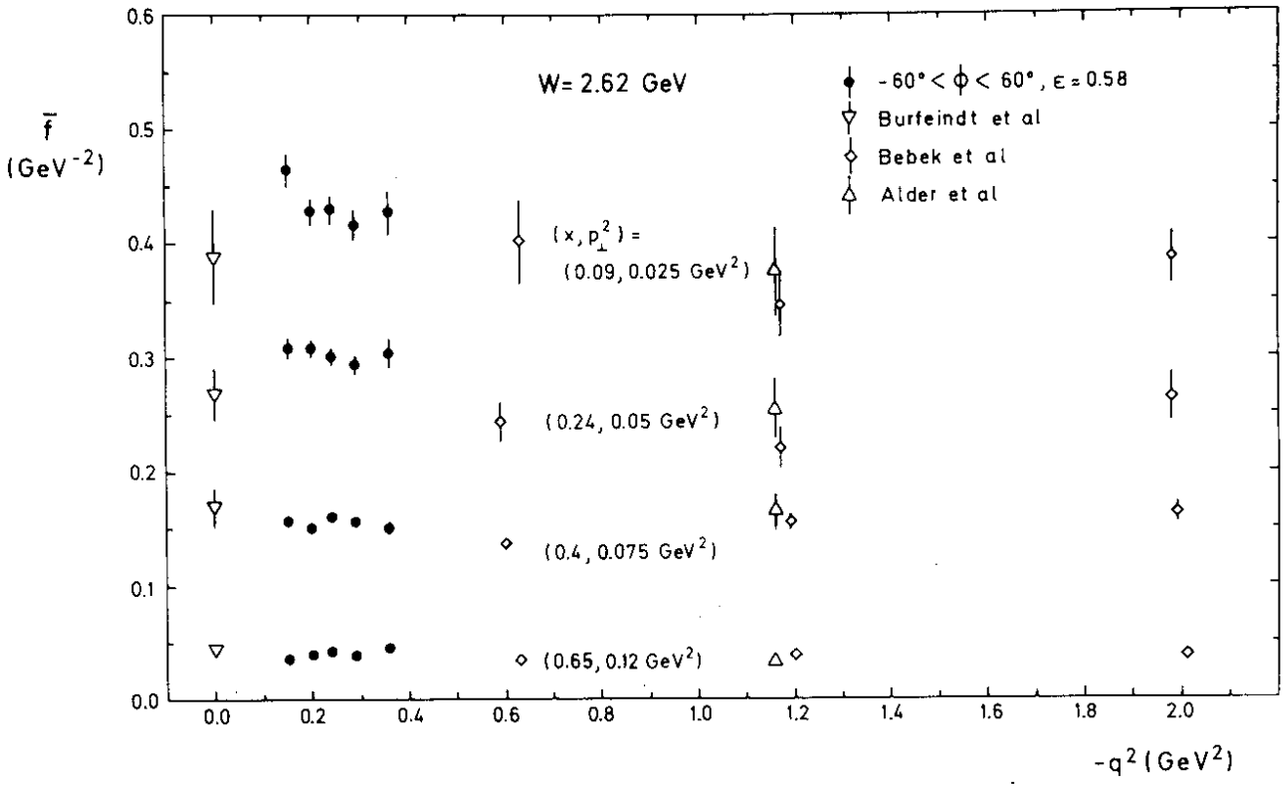

FIG. 2.34 The Q^2 dependence of f at W = 2.62 GeV.

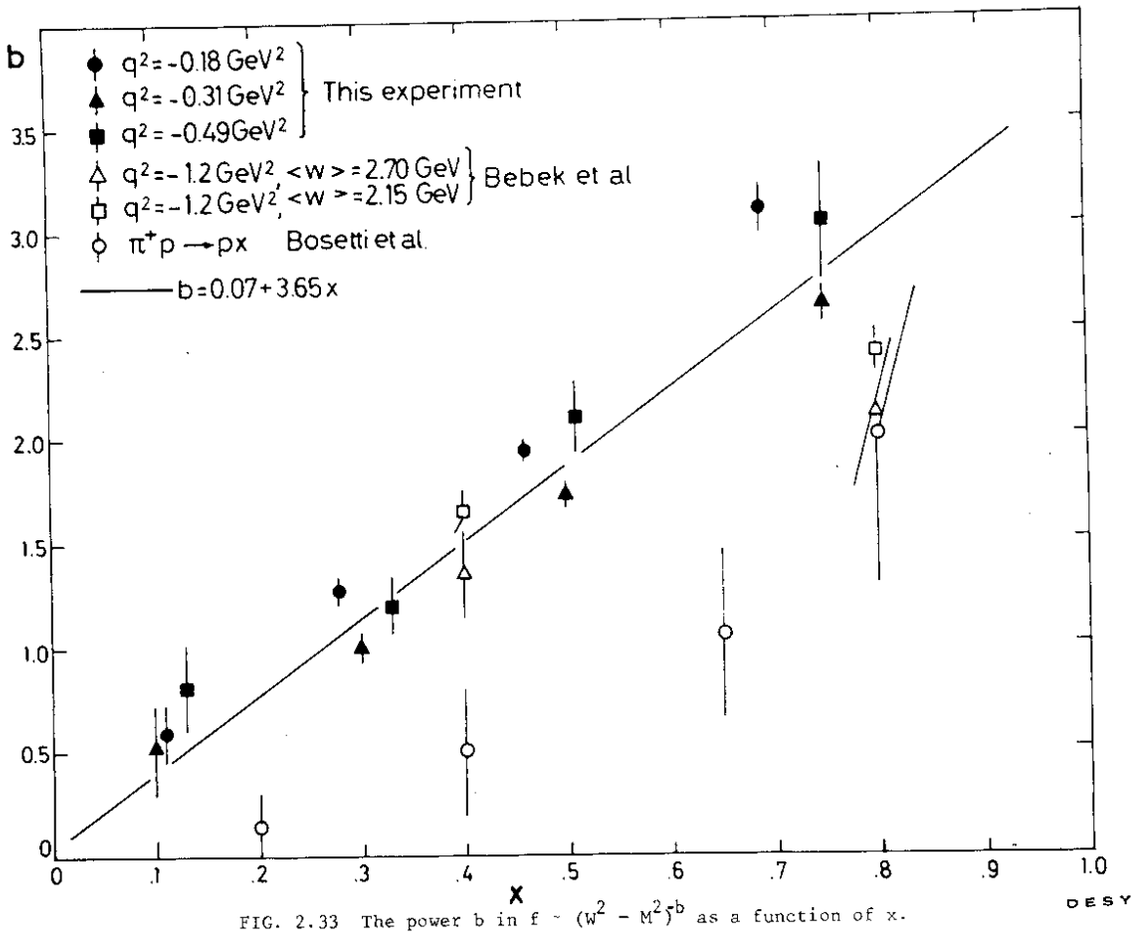

FIG. 2.33 The power b in $f \sim (W^2 - M^2)^b$ as a function of x.

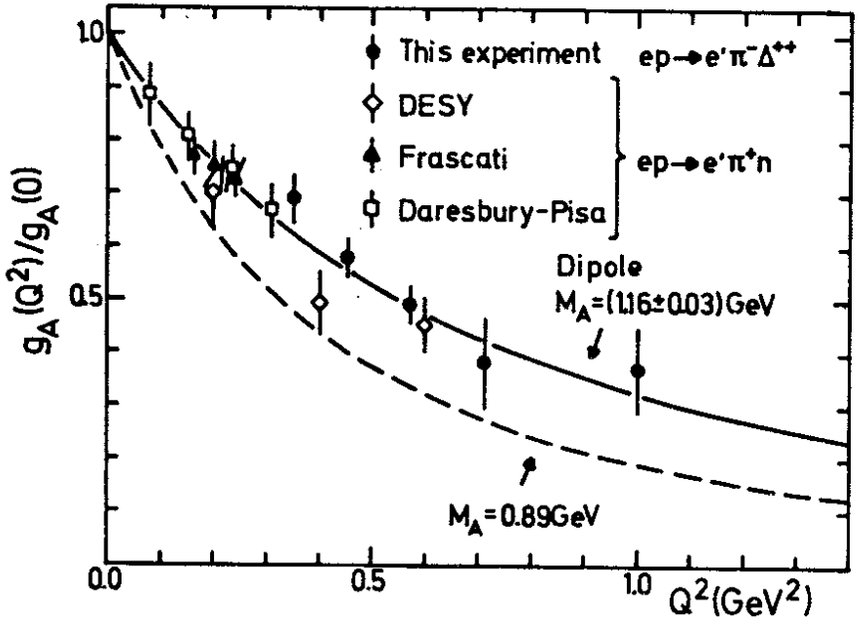

FIG. 2.35 Axial form factor of the nucleon as determined by $\gamma_v p \to \pi^+ n$ and $\gamma_v p \to \pi^- \Delta^{++}$.

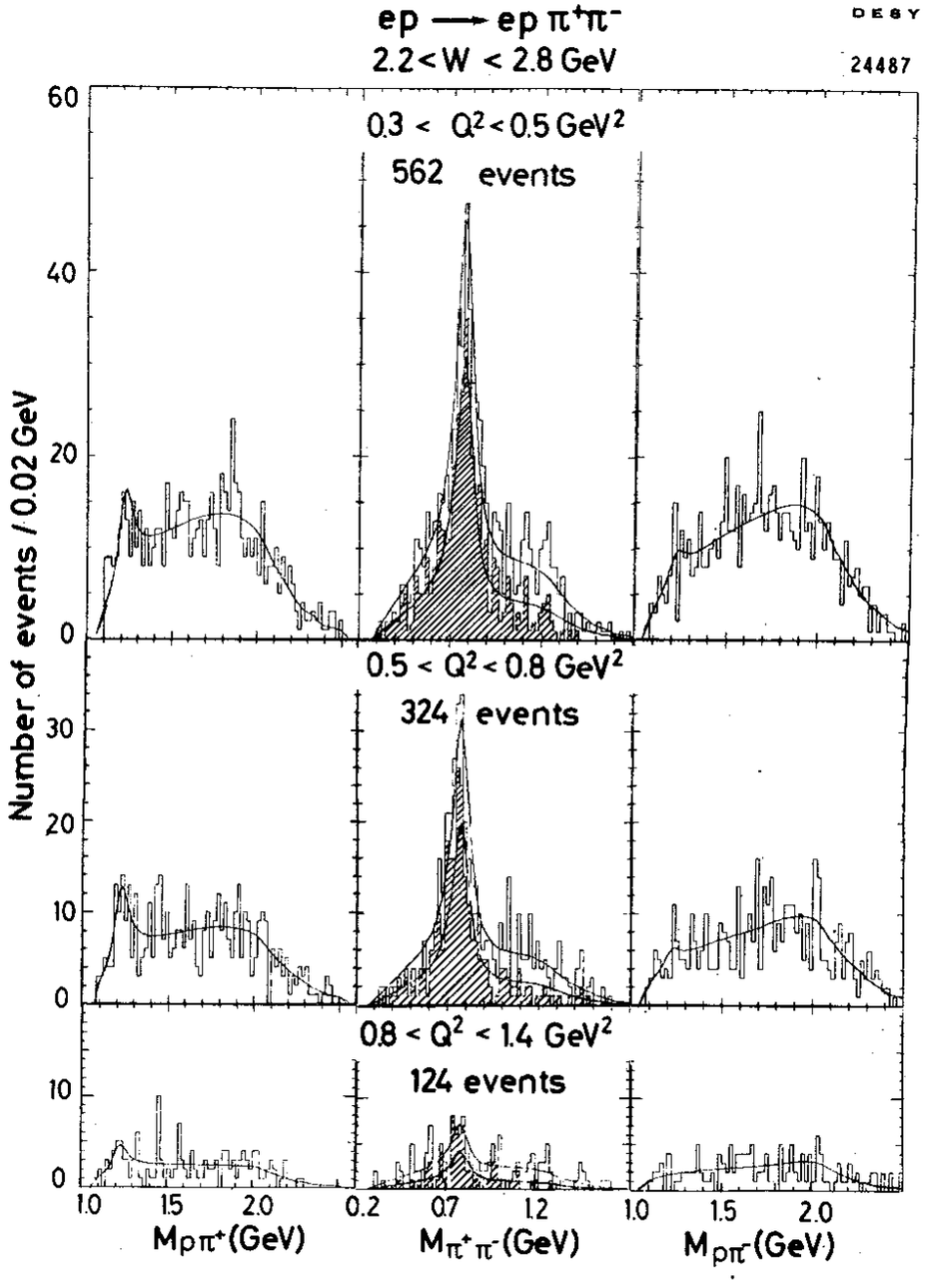

FIG. 2.36 The $p\pi^+$, $\pi^+\pi^-$ and $p\pi^-$ mass distribution for 2.0 < W < 2.2 GeV.

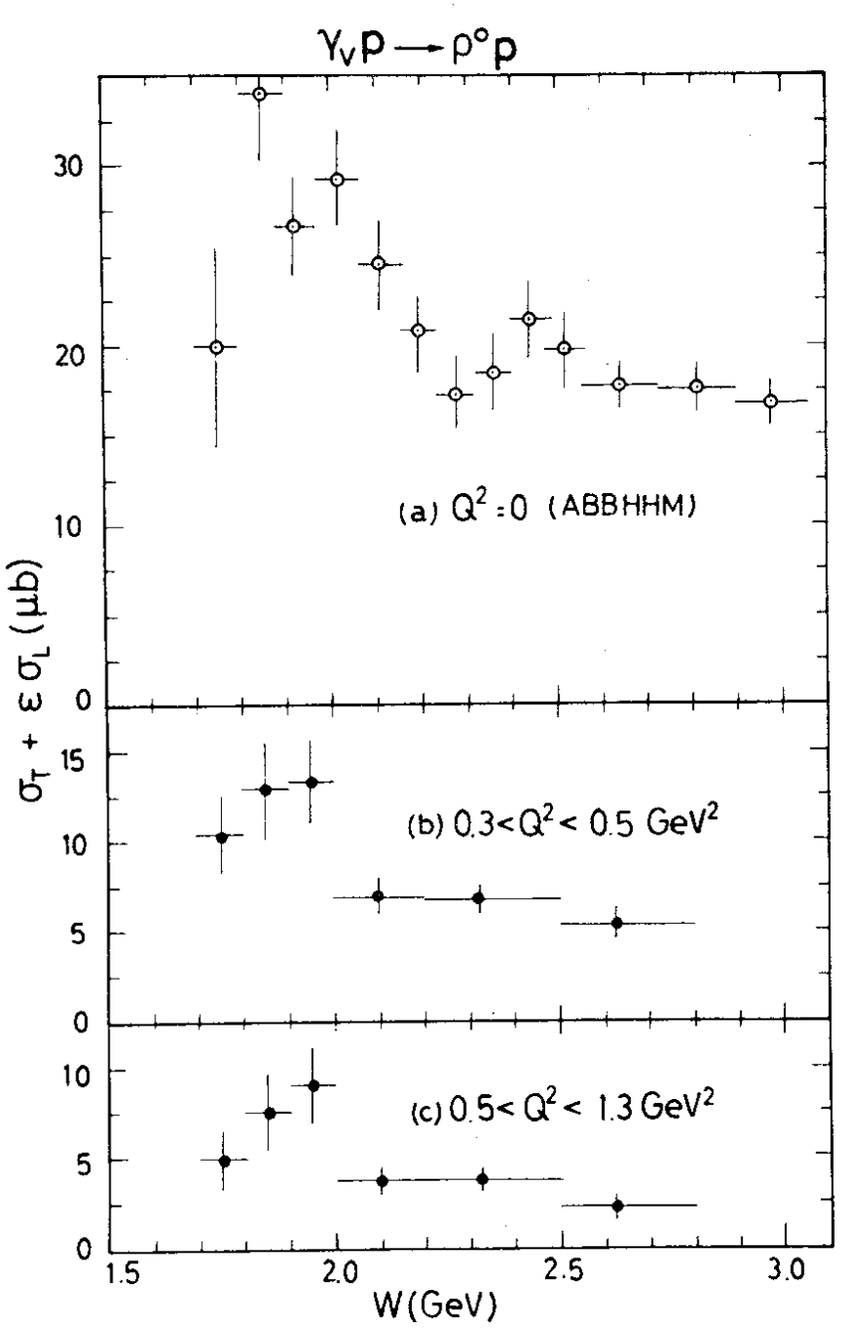

FIG. 2.37 W dependence of the cross section for $\gamma_v p \rightarrow \rho^0 p$ for different Q^2 regions. The ABBHHM data are from Ref.40.

24495

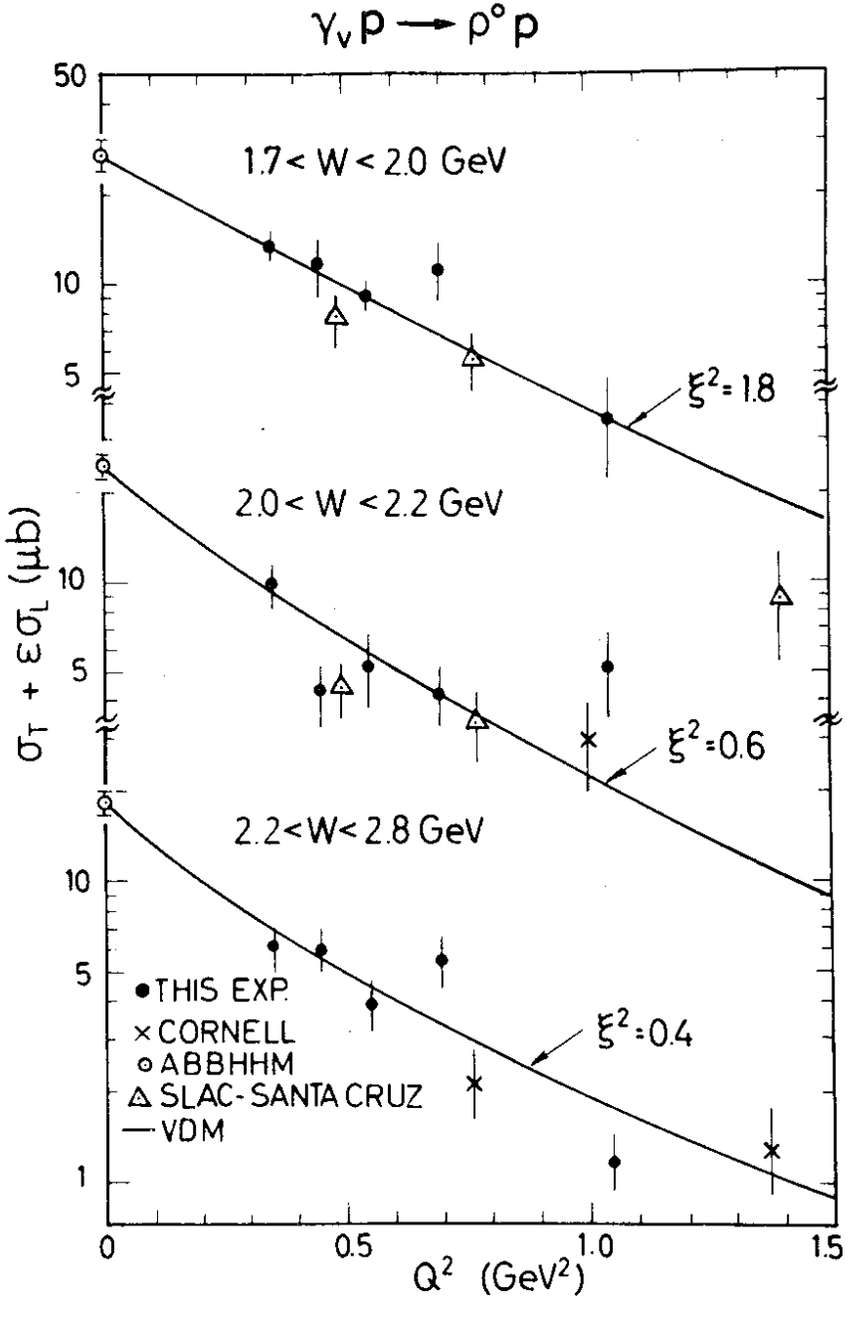

FIG. 2.38 Q^2 dependence of the cross section for $\gamma_v p \rightarrow \rho^0 p$ for different regions of W.

DESY

24501

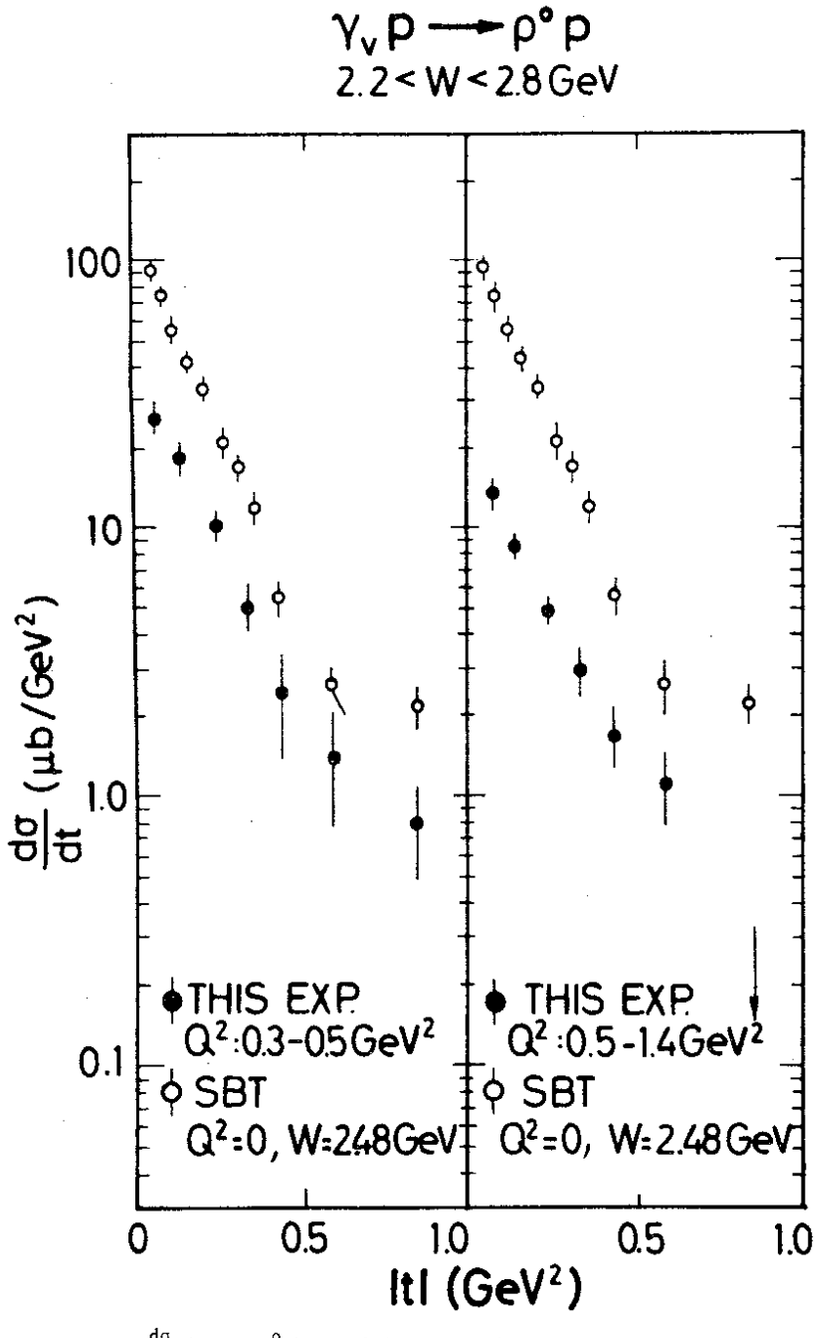

FIG. 2.39 $\frac{d\sigma}{dt}$ ($\gamma_v p \rightarrow \rho^o p$) for $2.2 < W < 2.8$ GeV and two regions of Q^2. The SBT points are from Ref.41.

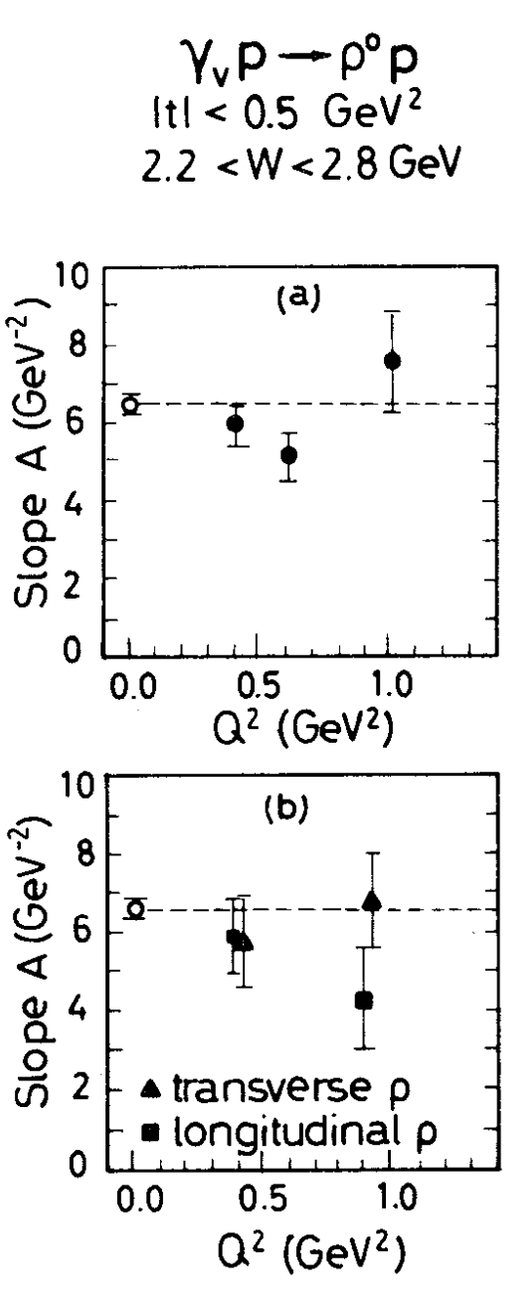

FIG.2.40 a)
The slope parameter A of of $d\sigma/dt \sim \exp\{At\}$ for the reaction $\gamma_v p \rightarrow \rho^o p$ as a function of Q^2 at $2.2 < W < 2.8$ GeV.

FIG.2.40 b)
Same as a) but for transverse and longitudinal rhos separately. The photoproduction point (open circle) is from Ref.40.

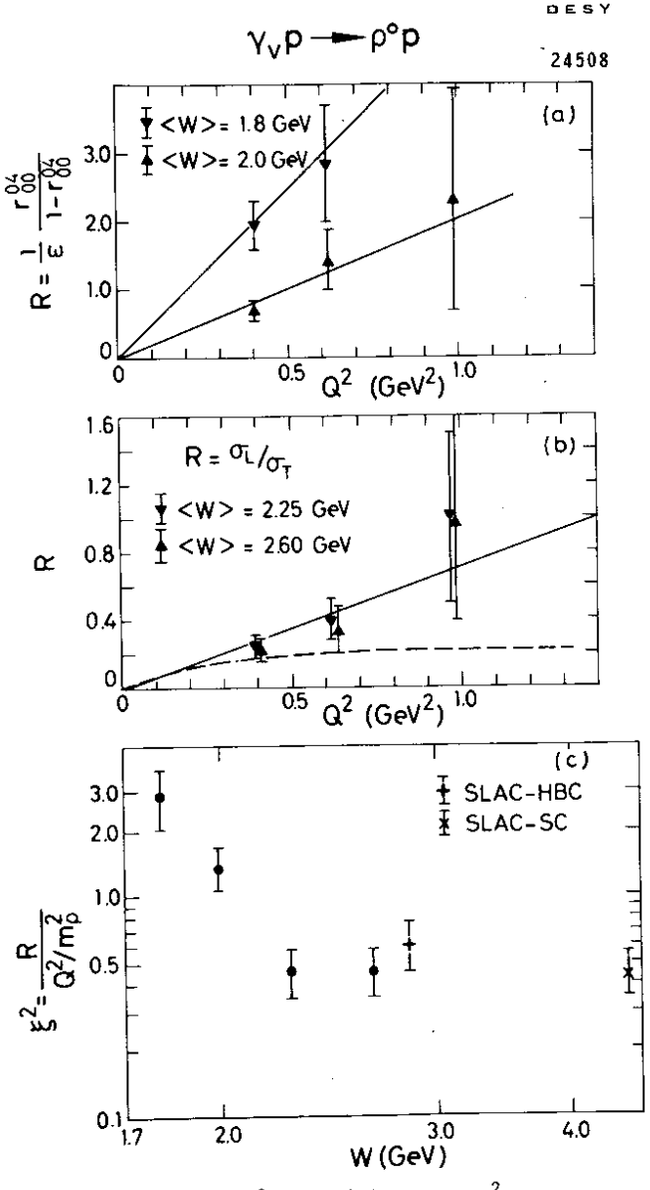

FIG. 2.41 Reactions $\gamma_V p \rightarrow \rho^0 p$ for $|t| < 0.5$ GeV^2.
a) and b) show $R = \sigma_L/\sigma_T$ for different intervals of W. The full lines are fits to $R = \xi^2 Q^2/m_\rho^2$, the dotted line represents $\sigma_L^{tot}/\sigma_T^{tot}$ from Ref.42.
c) The parameter of ξ^2 as a function of W. The points labelled SLAC-HBC and SLAC-SC are taken from Refs.43 and 44, respectively.

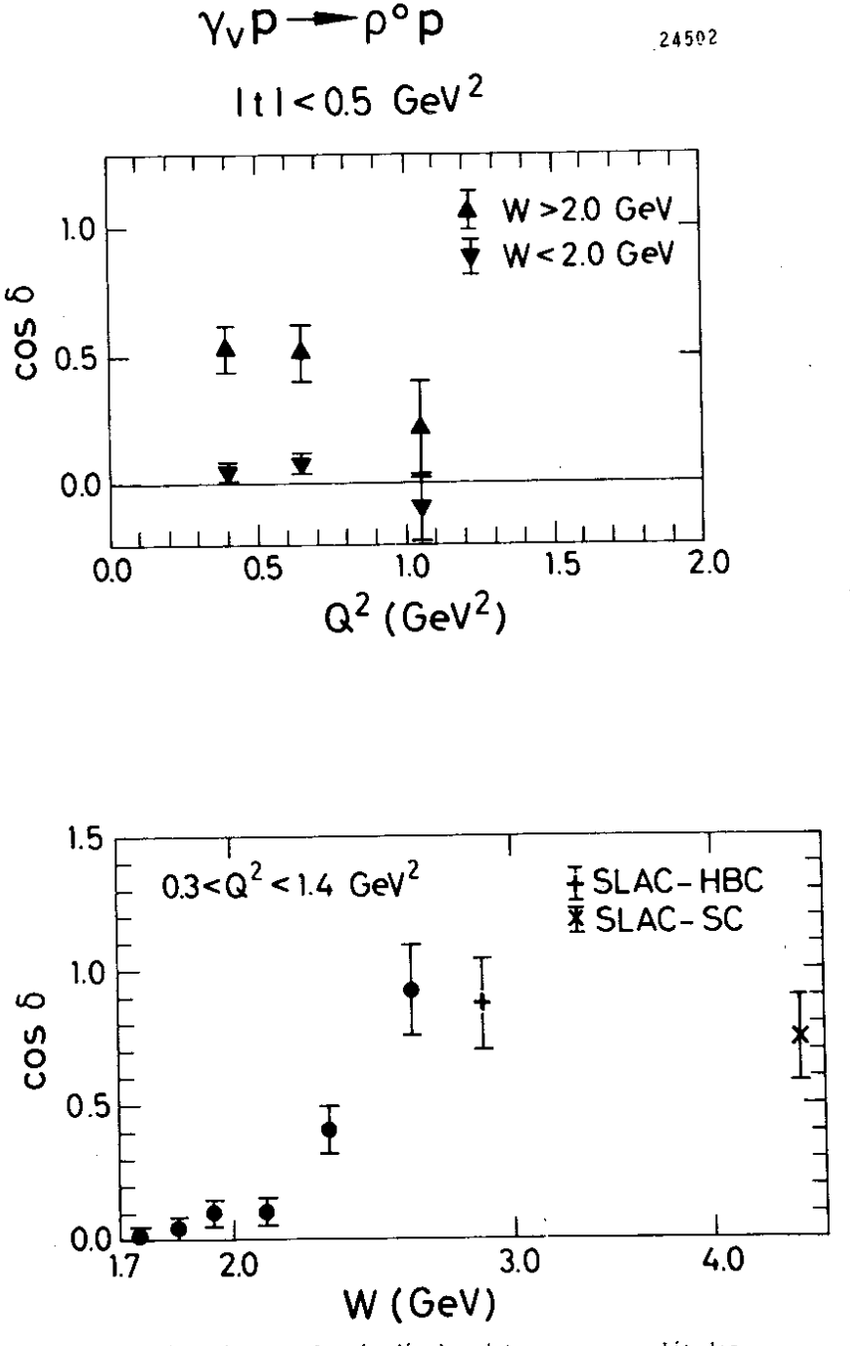

FIG. 2.42 The phase between longitudinal and transverse amplitudes as a function of Q2 and W for $|t| < 0.3$ GeV^2.

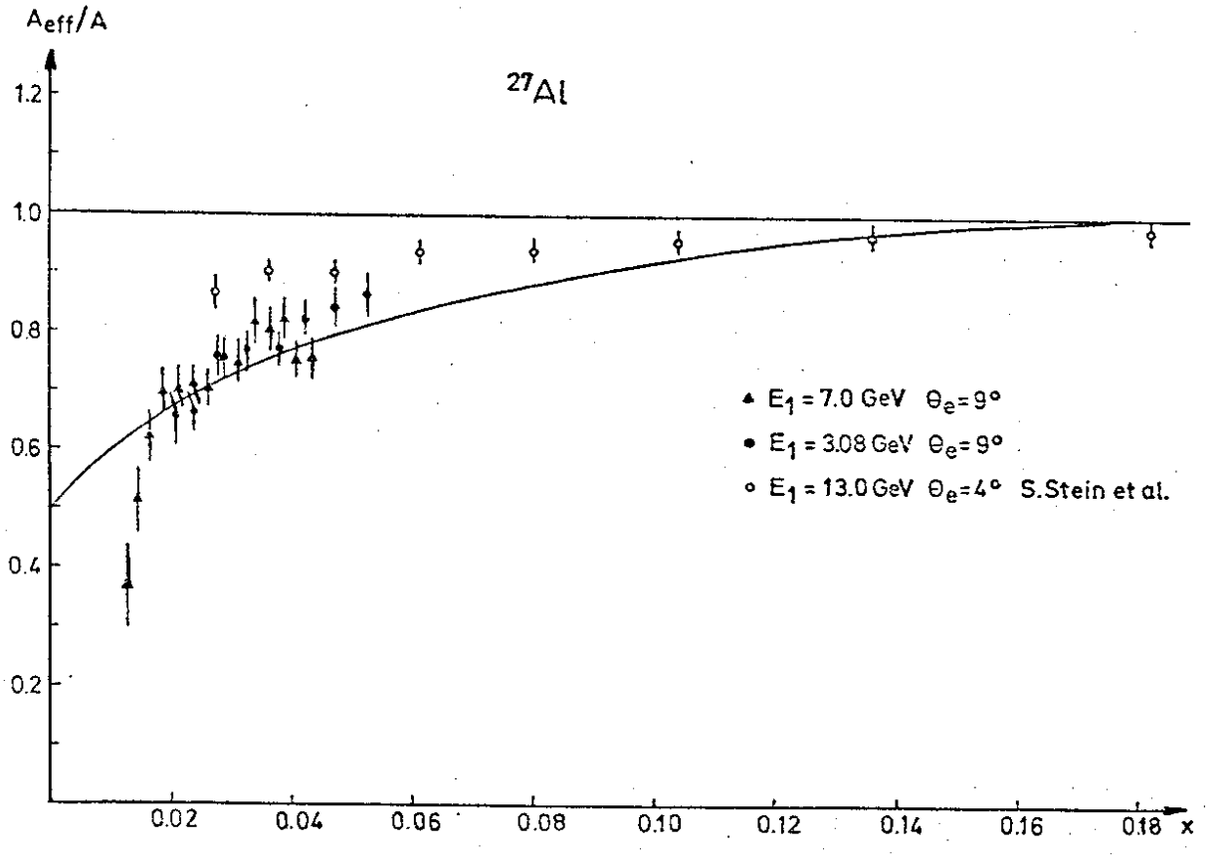

FIG. 2.44 The ratio $A_{eff}/A = \sigma(\gamma_v\ ^{27}Al)/(\sigma(\gamma_v N) \cdot 27)$ as a function of $x = \frac{Q^2}{2M\nu}$. The solid curve is the theoretical prediction of generalized vector meson dominance[48] for ^{207}Pb. The circle are from Ref.49.

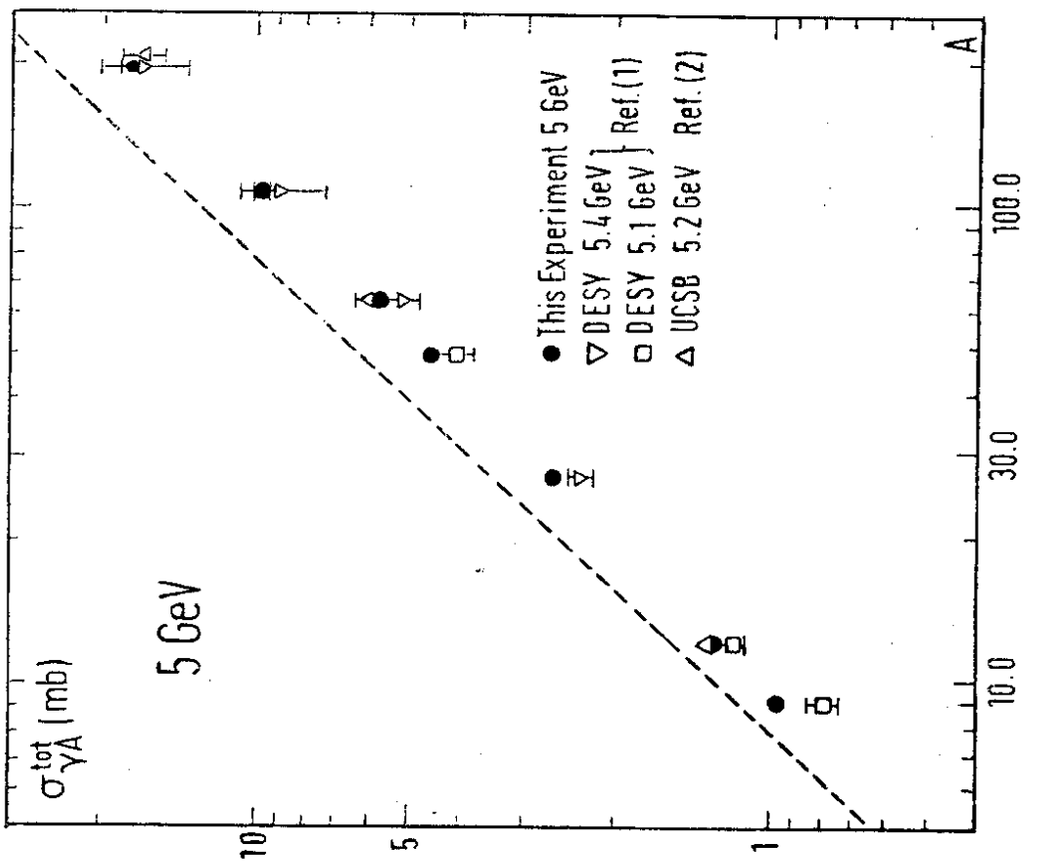

FIG. 2.43 Total photon nucleus cross section as a function of nuclear mass number. The full circles represent the values derived from small angle Compton scattering[46] off nuclei. The dotted line represents σ^{tot} (nucleon) · A, the total cross section expected in the absence of shadowing.

FIG. 3.1 Ratio of hadronic to μ pair cross section in e^+e^- annihilation. The data points are from Refs.55 and 56.

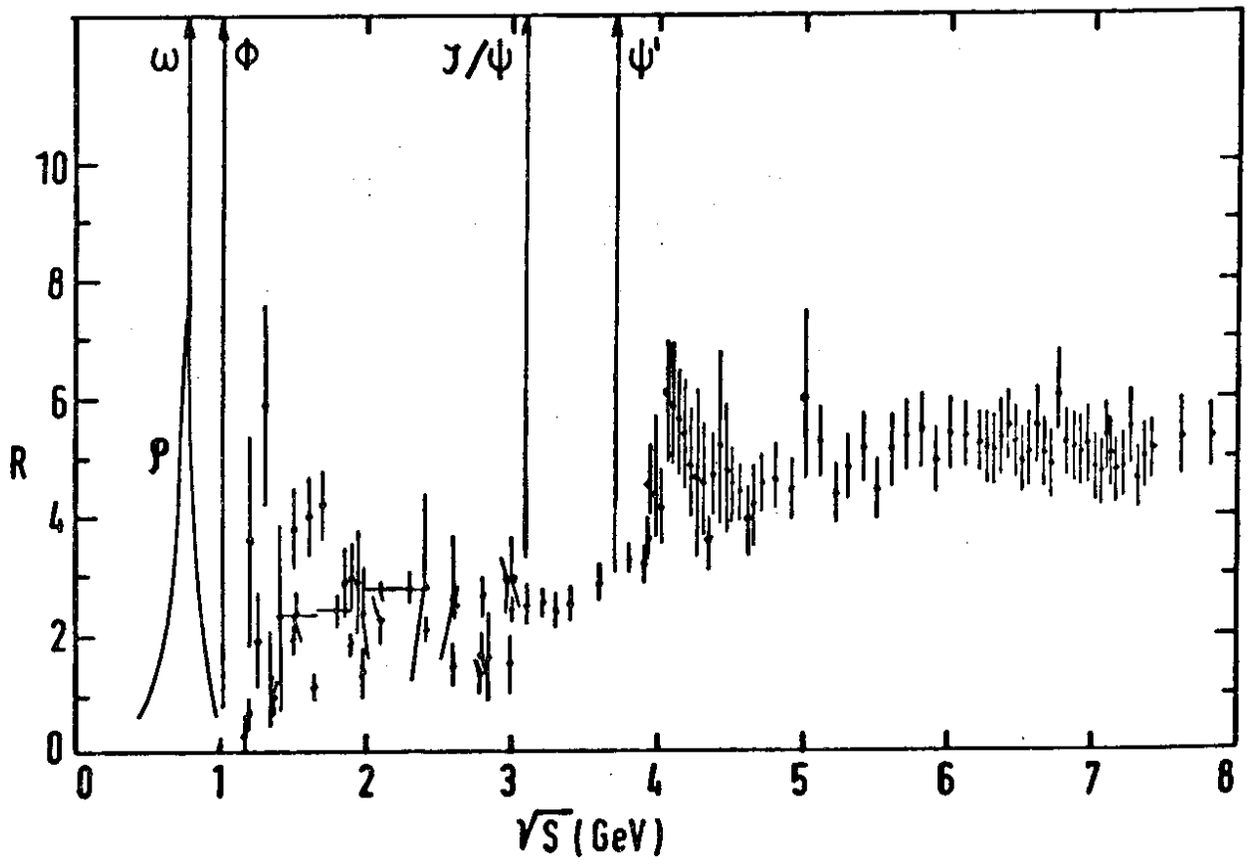

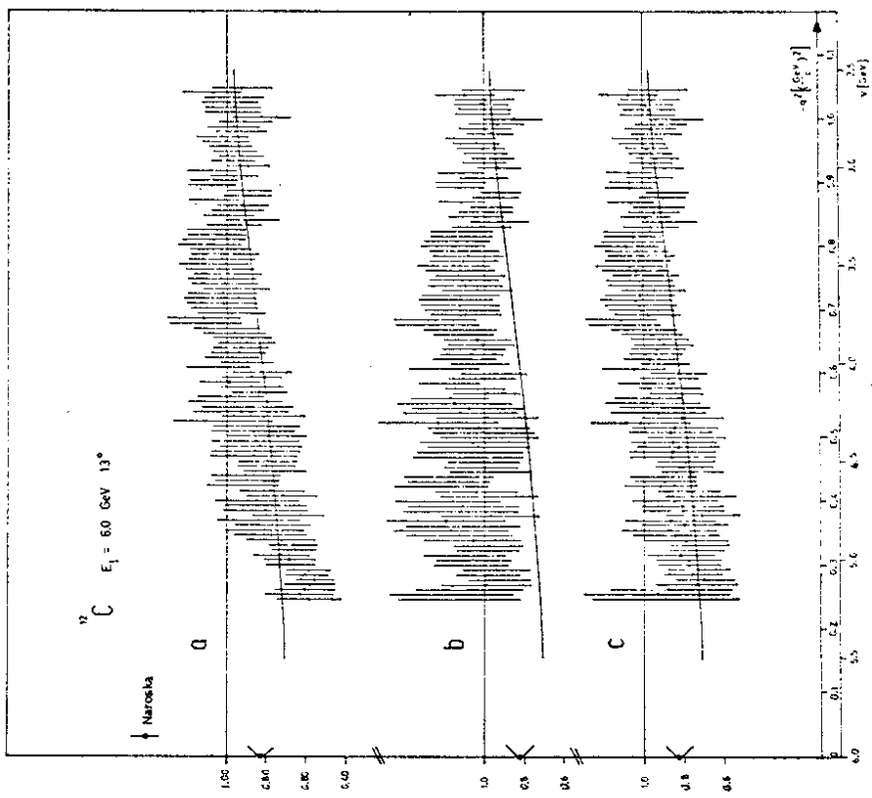

FIG. 2.45 A_{eff}/A as a function of ν for three different treatments of the radiative corrections:

a) only radiative tail from elastic electron nucleus scattering taken into account.

b) only radiative tail due to elastic electron scattering on the free nucleon taken into account.

c) realistic calculation[50], taking quasi-elastic electron nucleon scattering into account.

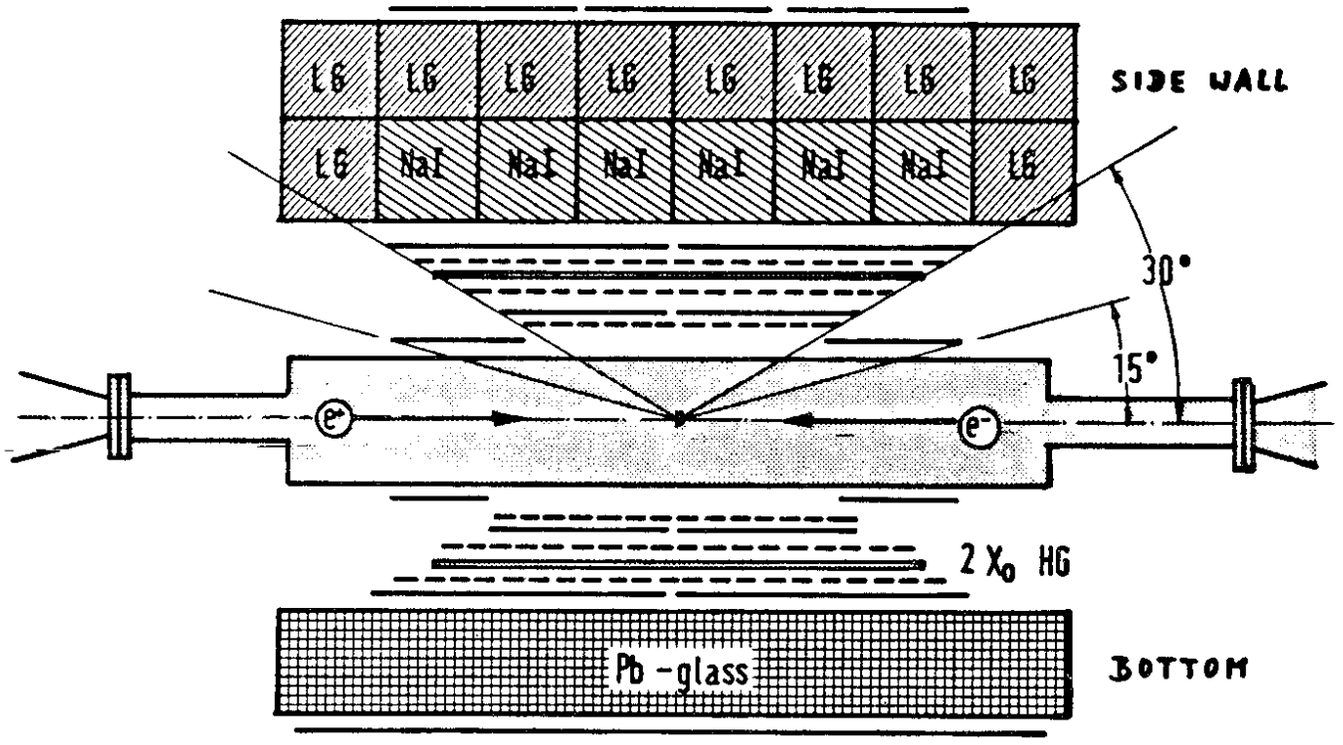

FIG. 3.3 Schematic View of the DESY-Heidelberg non-magnetic detector.

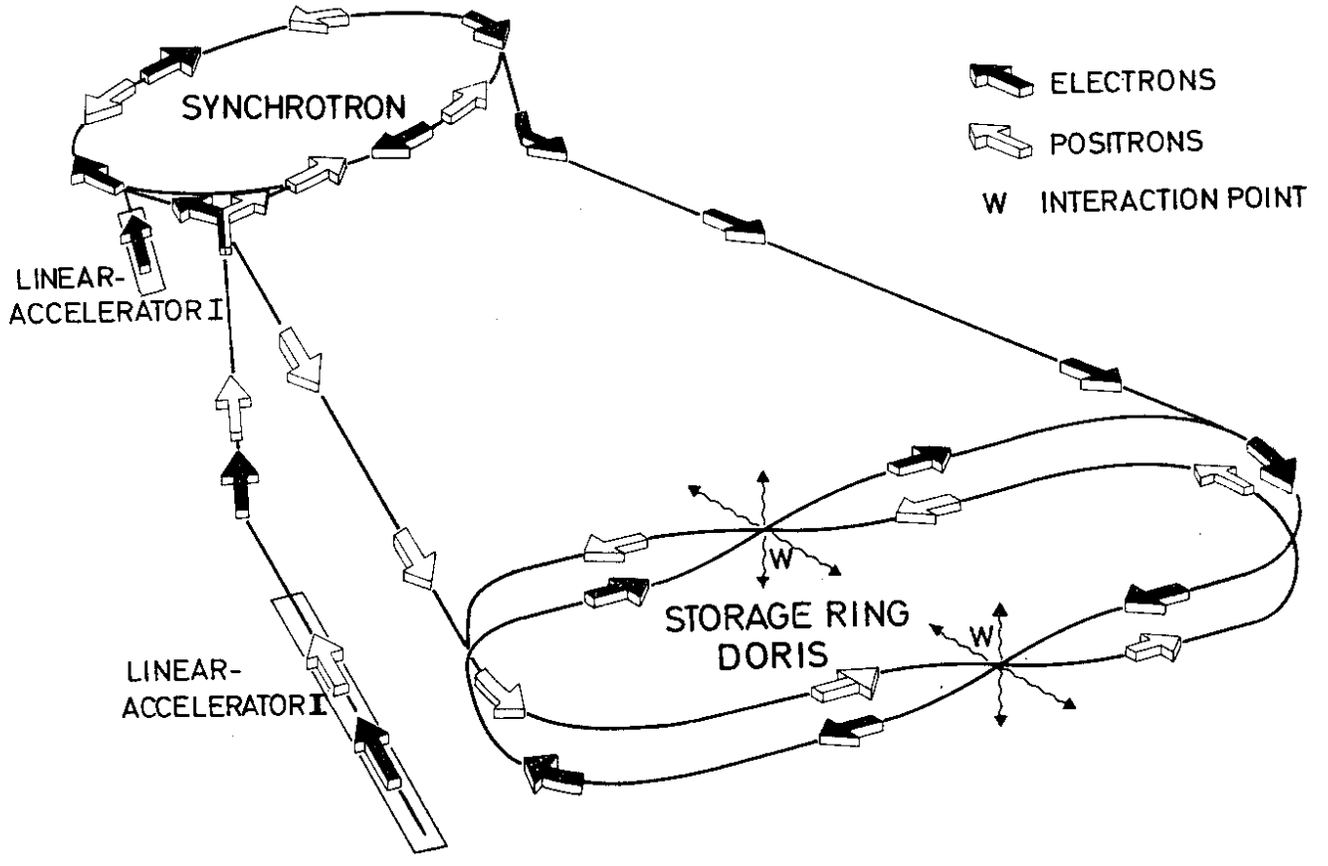

FIG. 3.2 Schematic view of the DORIS storage ring with its injection system.

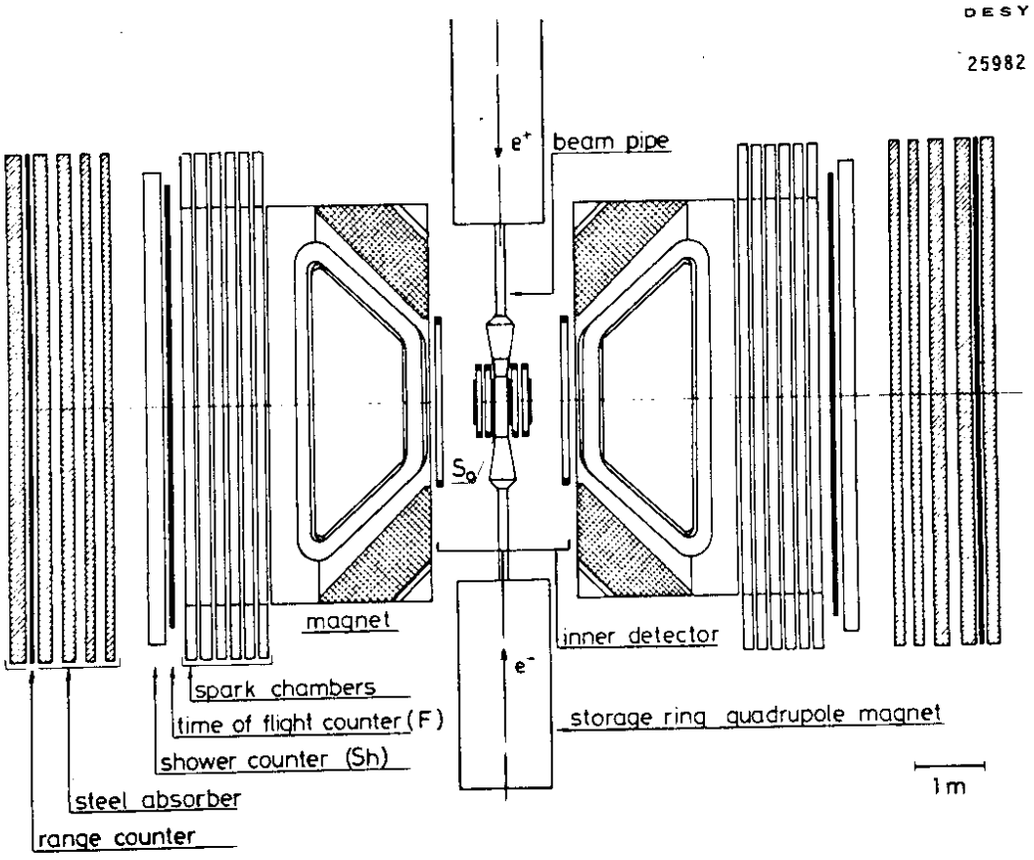

FIG. 3.5 Top view of the double arm spectrometer DASP.

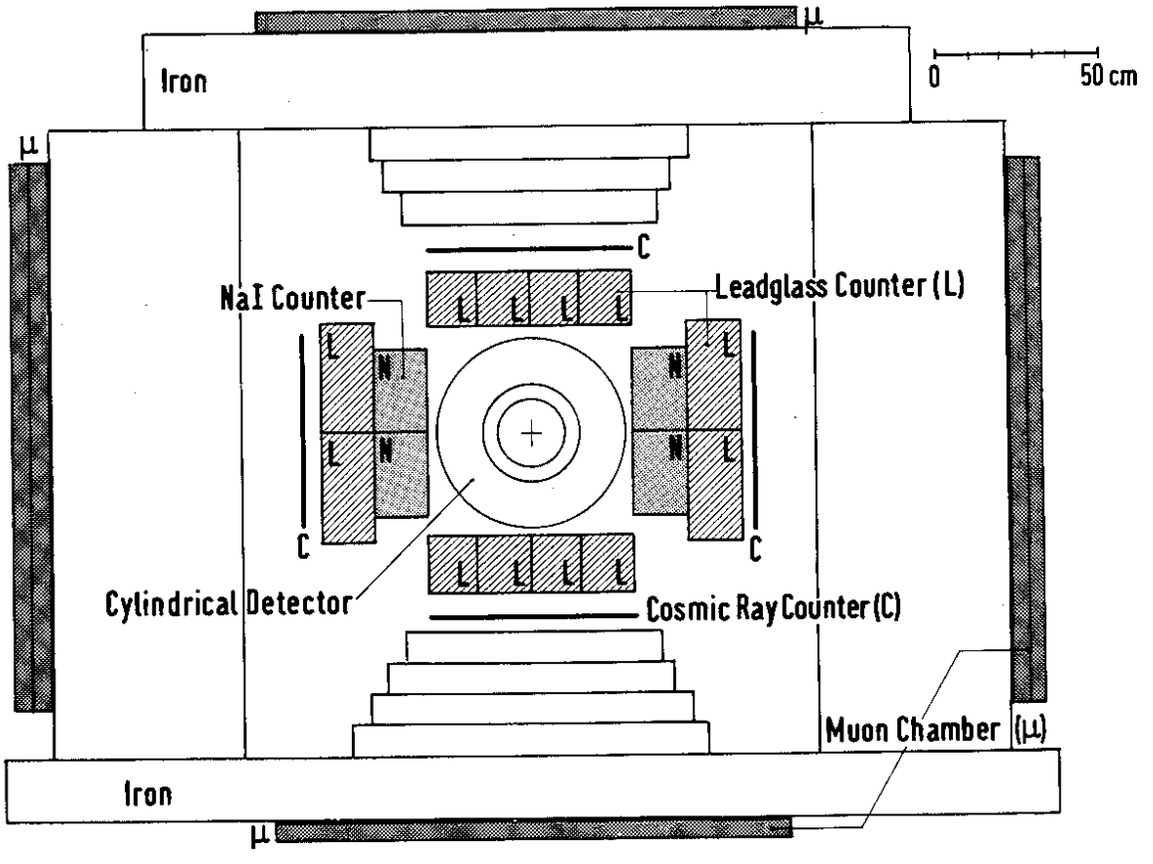

FIG. 3.4 DESY-Heidelberg detector seen along the beam pipe.

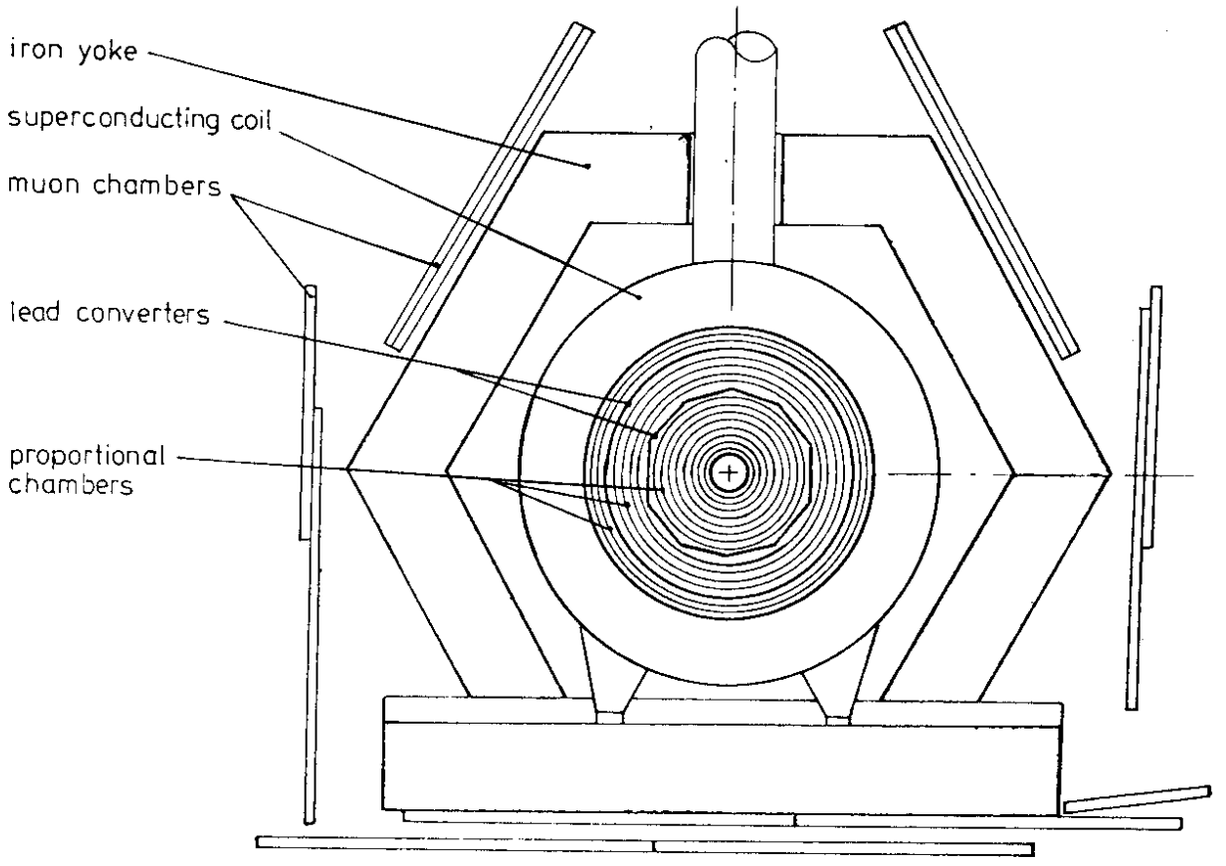

FIG. 3.7 View of the magnetic solenoid detector PLUTO.

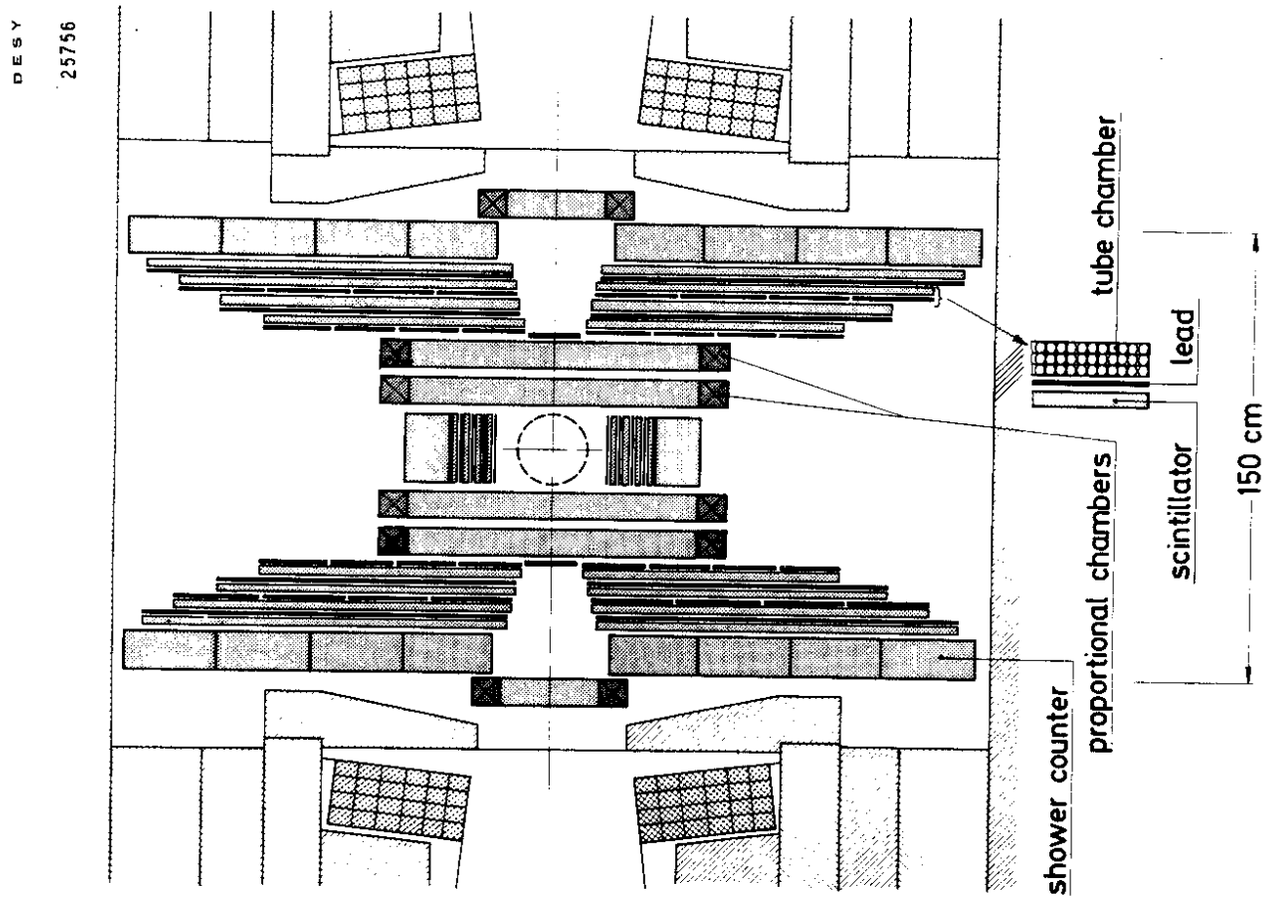

FIG. 3.6 View of the inner detector of DASP.

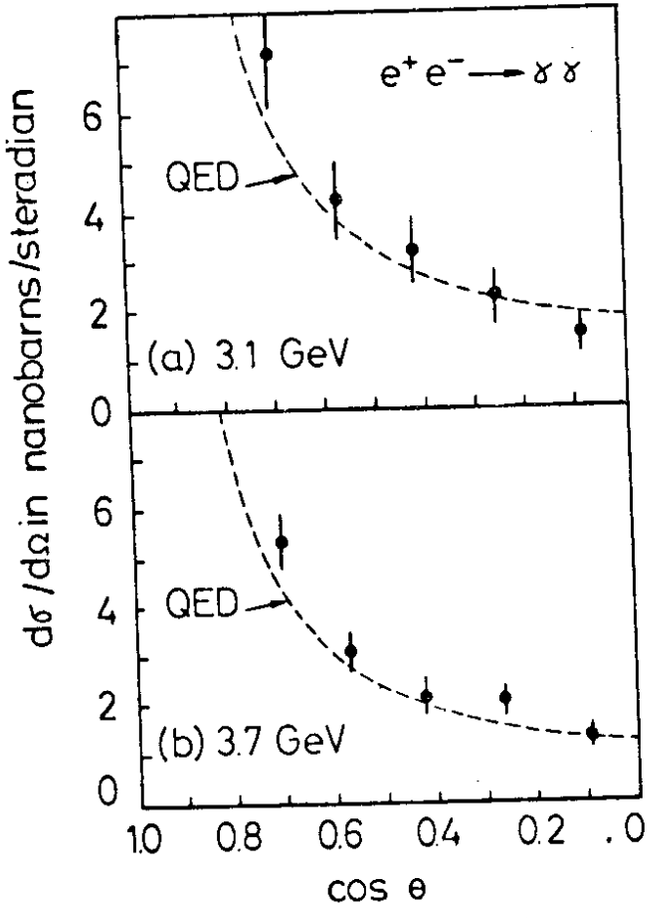

FIG. 3.8 Comparison of measured angular distributions for $e^+e^- \rightarrow \gamma\gamma$ at the J/ψ and ψ' resonances with QED predictions.

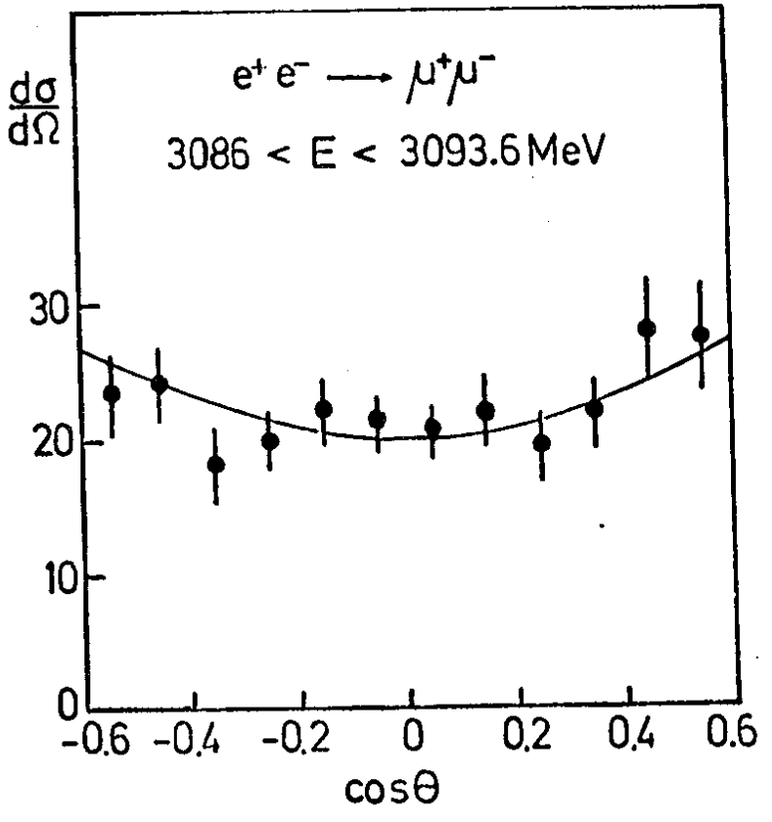

FIG. 3.9 Angular distribution for μ pair production at the J/ψ. The curve shows a $1 + \cos^2\theta$ dependence.

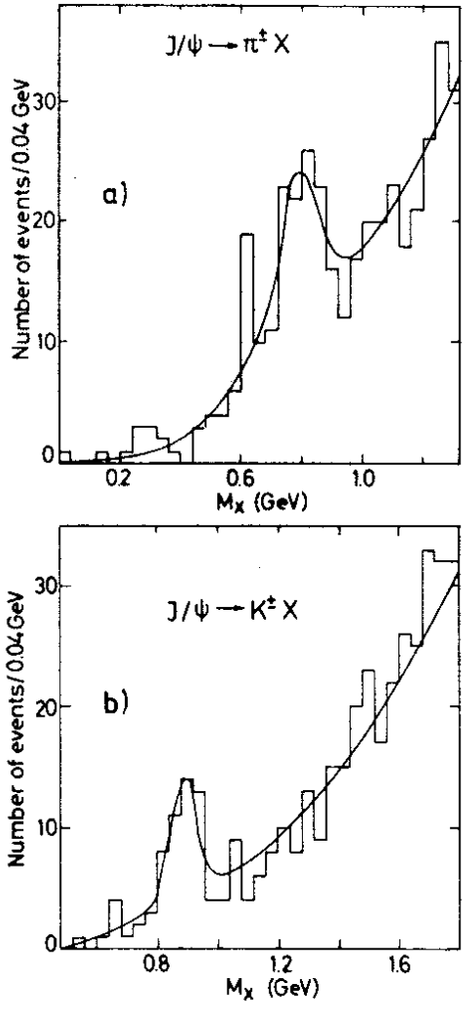

FIG. 3.10 ρ and $K^*(890)$ seen in the recoil spectrum of inclusive π and K measurements at the J/ψ.

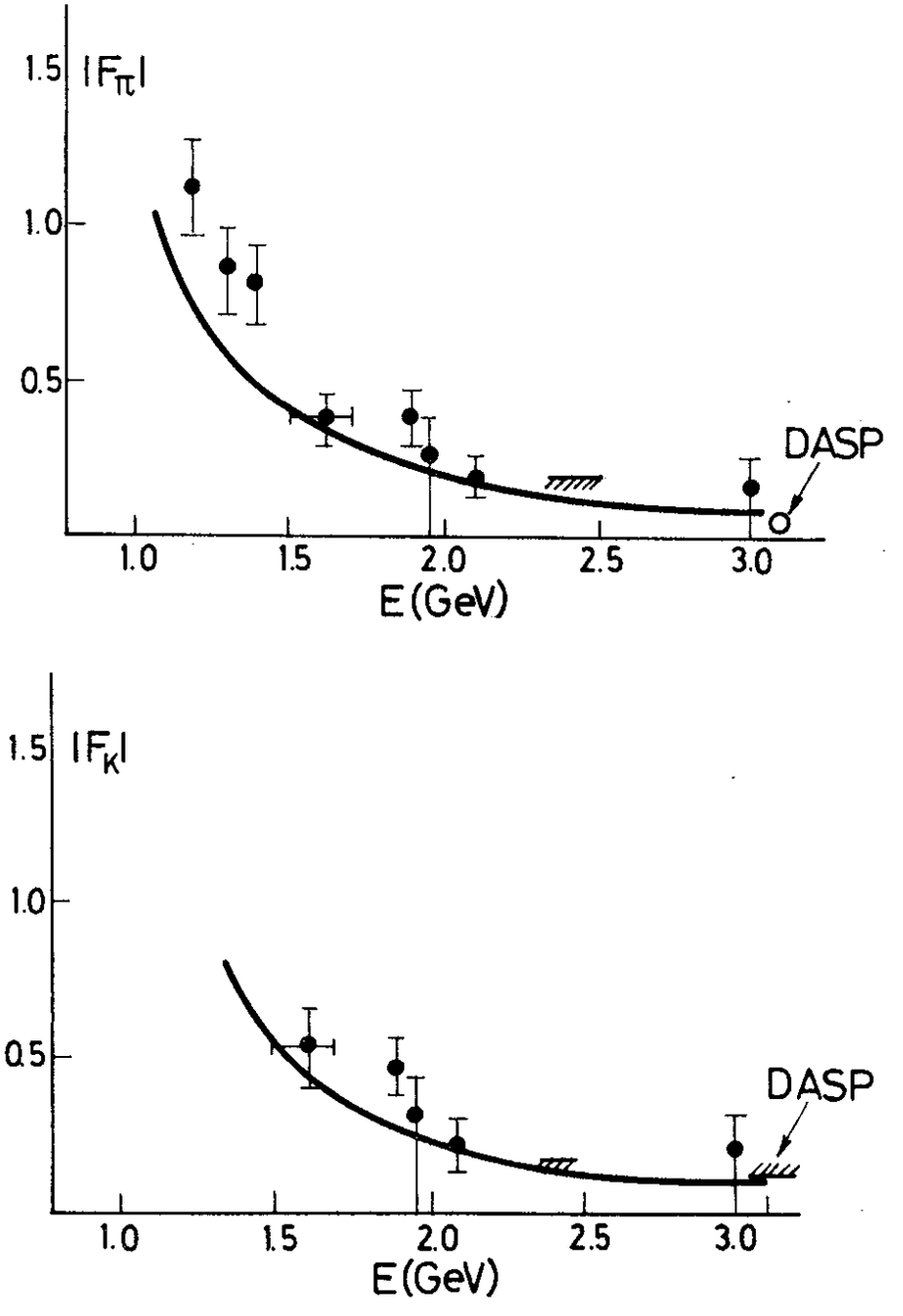

FIG. 3.11 π and K form factors as functions of the c.m. energy W in e^+e^- annihilation. The full circles and the curve are from Ref.64.

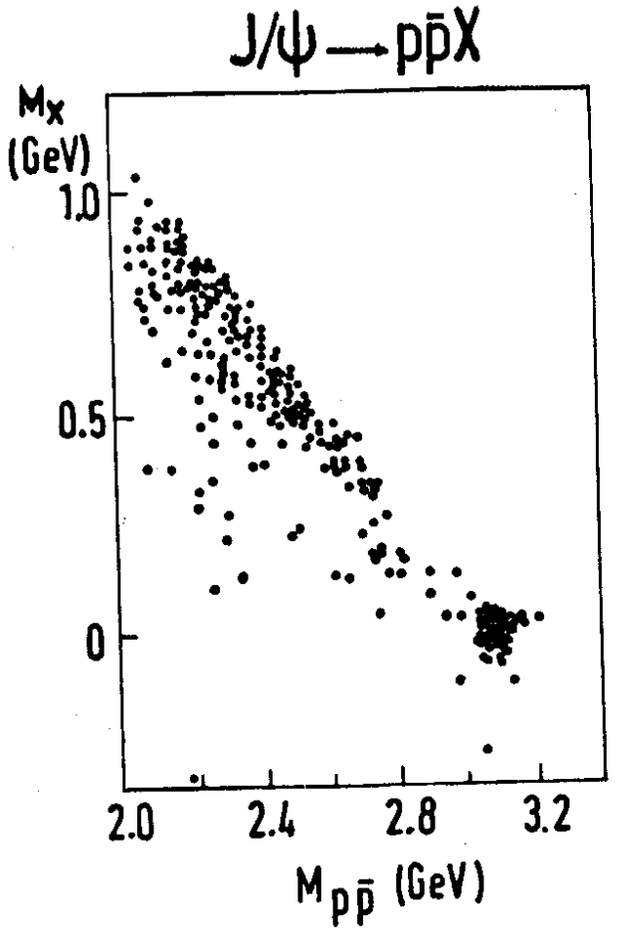

FIG. 3.12 Recoil mass M_x in the decay $J/\psi \to p\bar{p}\,X$ plotted versus the invariant mass $M_{p\bar{p}}$ of the $p\bar{p}$ system.

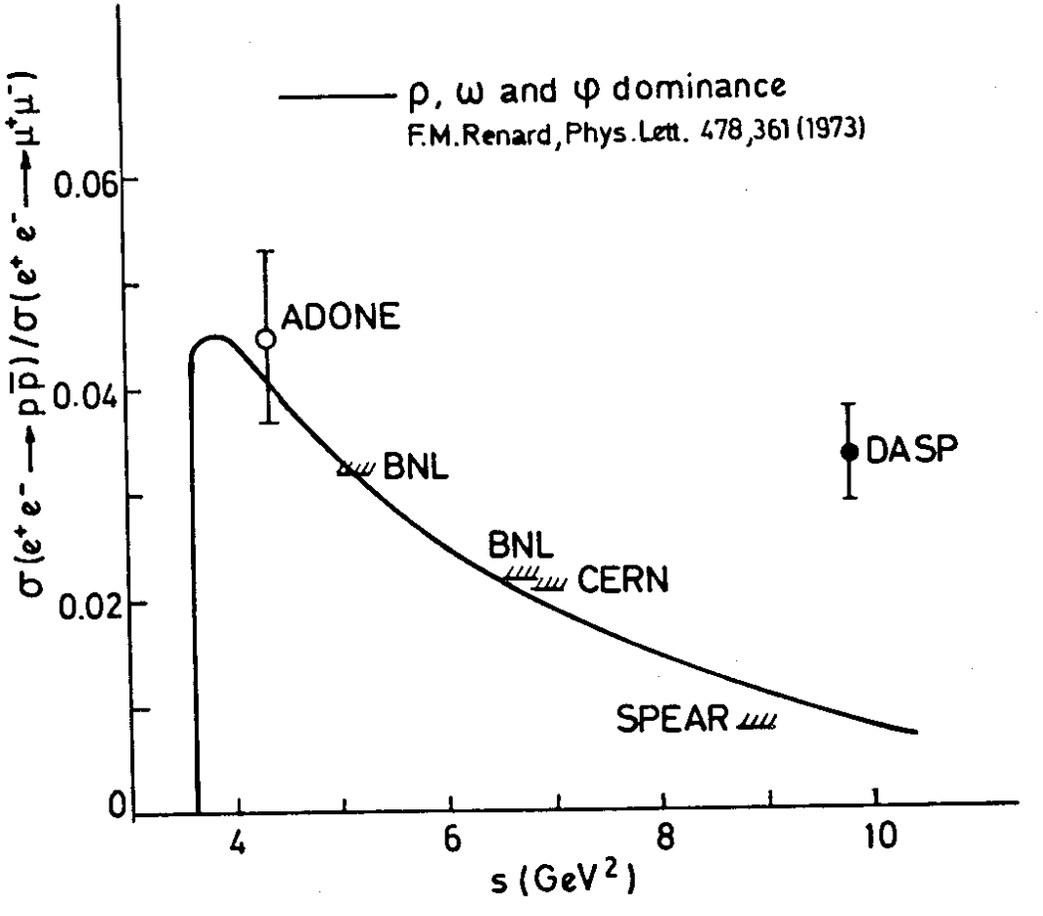

FIG. 3.13 Ratio of $p\bar{p}$ to μ pair cross section. The DASP point at the J/ψ exceeds the value, expected from the upper limits at lower energies (see Refs. 56 and 66) and from the form factor calculation by Renard.

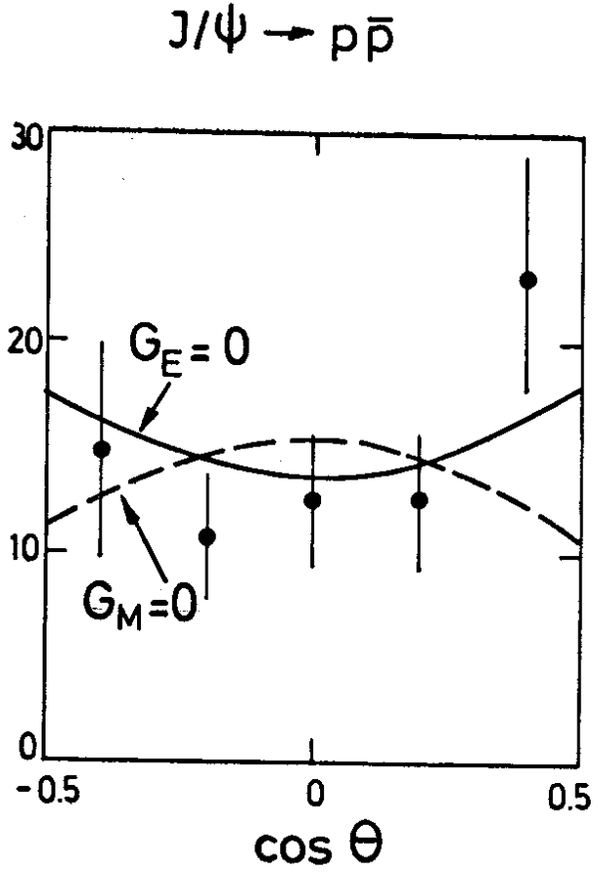

FIG. 3.14 Angular distribution of the decay $J/\psi \to p\bar{p}$. (G_E and G_M are explained in the text).

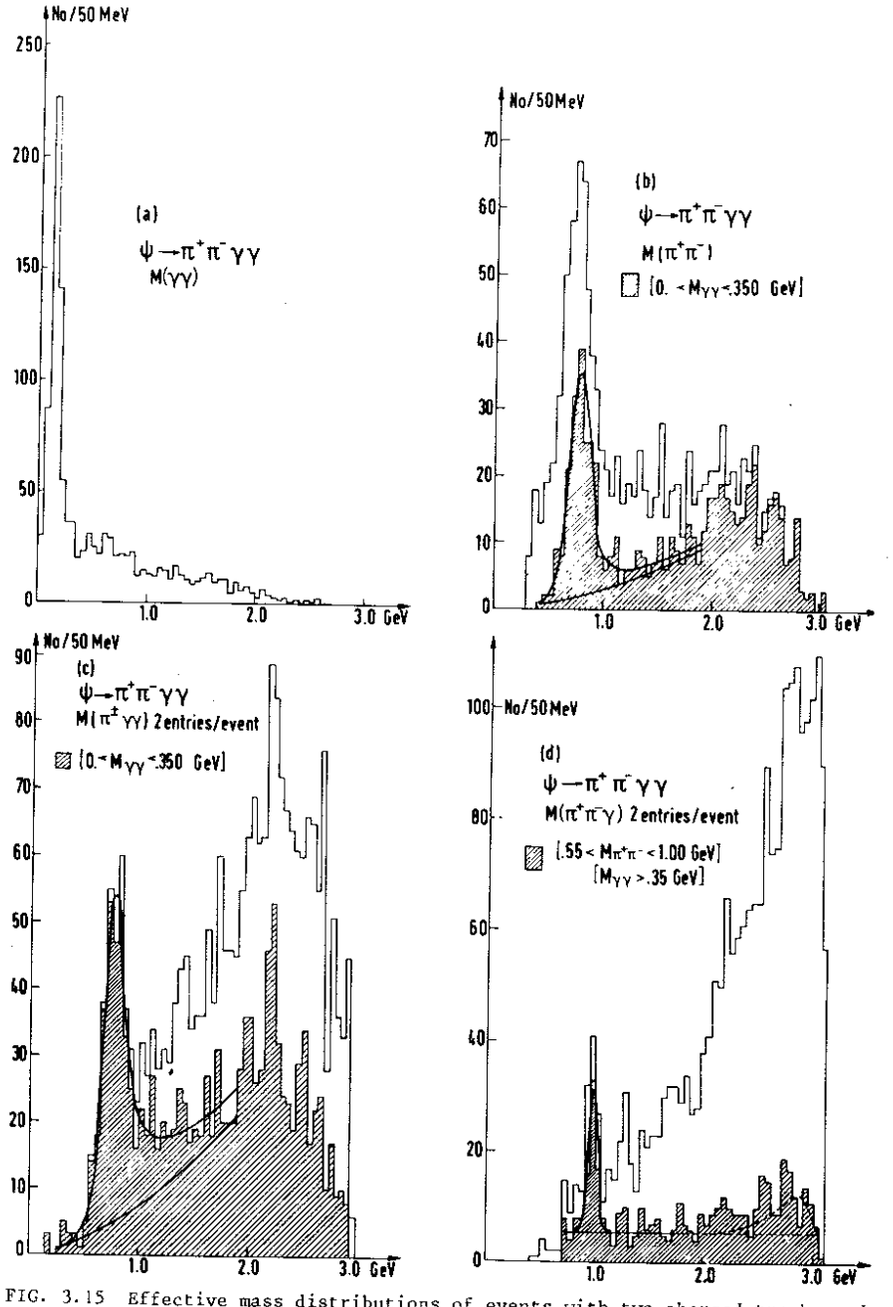

FIG. 3.15 Effective mass distributions of events with two charged tracks and two photons observed in the DESY-Heidelberg detector.

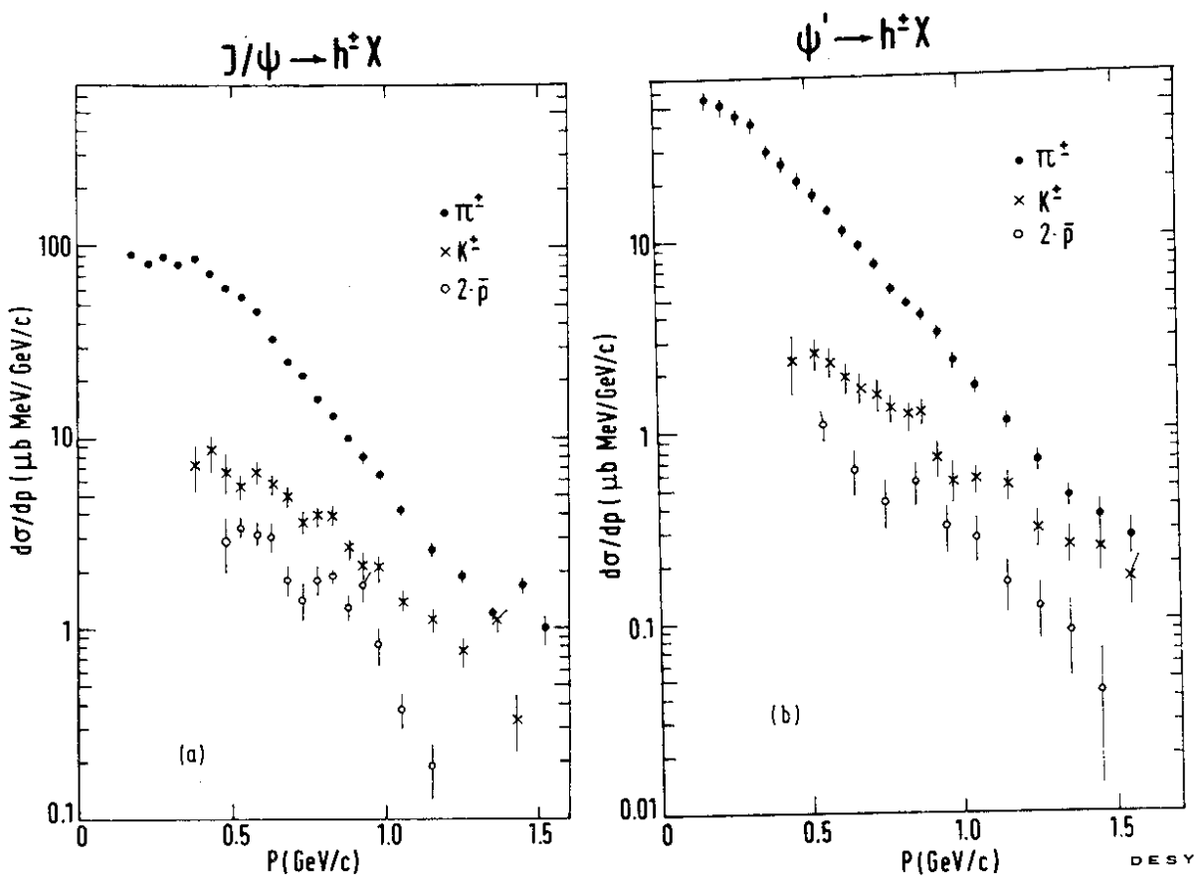

FIG. 3.17 Differential cross section for π, K, and p production as a function of the particle momenta at J/ψ and ψ'.

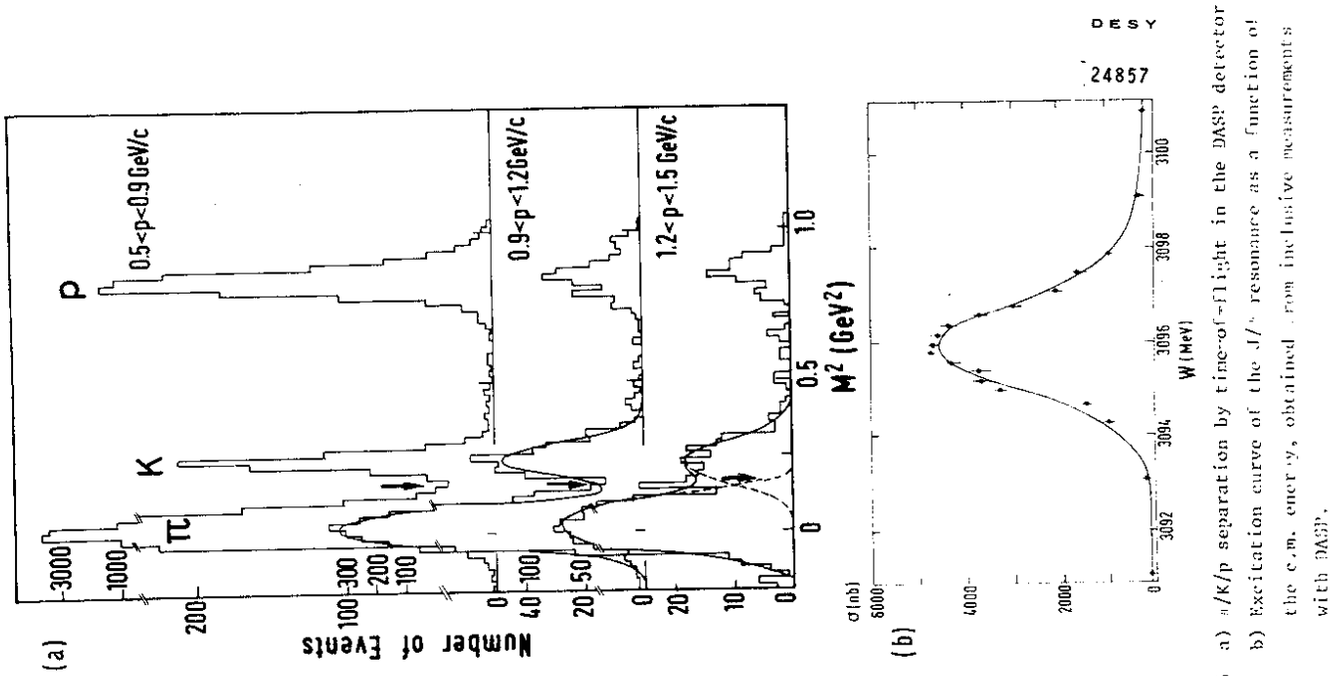

FIG. 3.16 a) π/K/p separation by time-of-flight in the DASP detector
b) Excitation curve of the J/ψ resonance as a function of the c.m. energy, obtained from inclusive measurements with DASP.

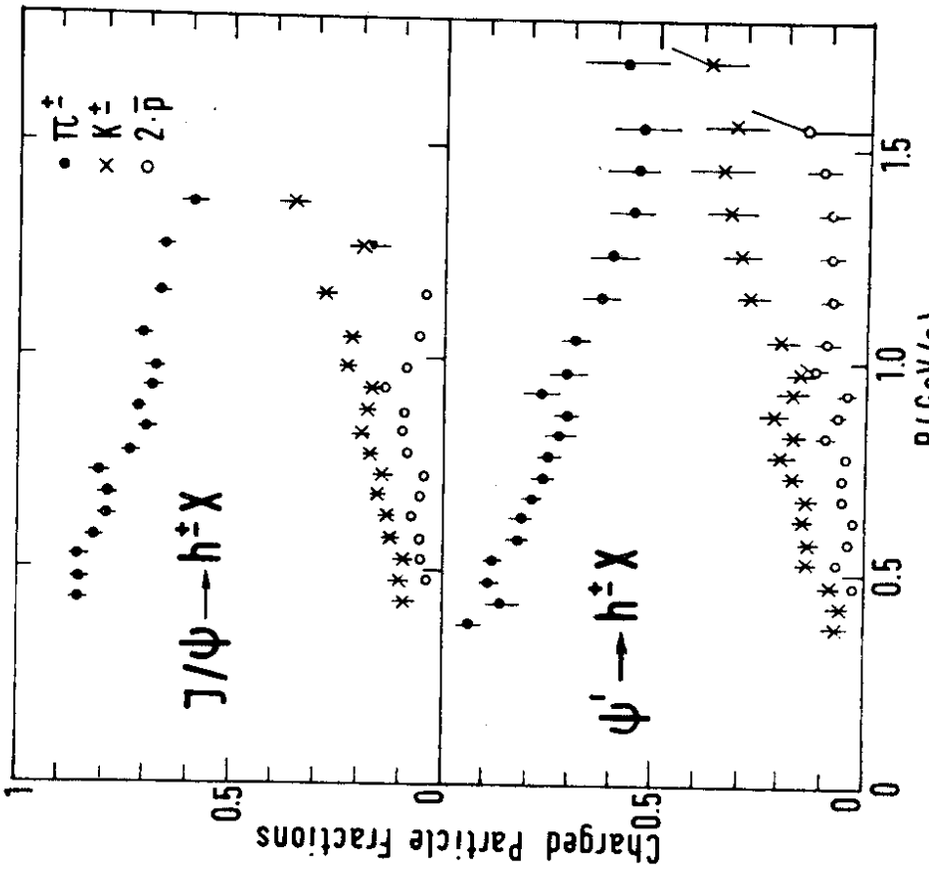

FIG. 3.19 Charged particle fractions at the J/ψ and ψ'.

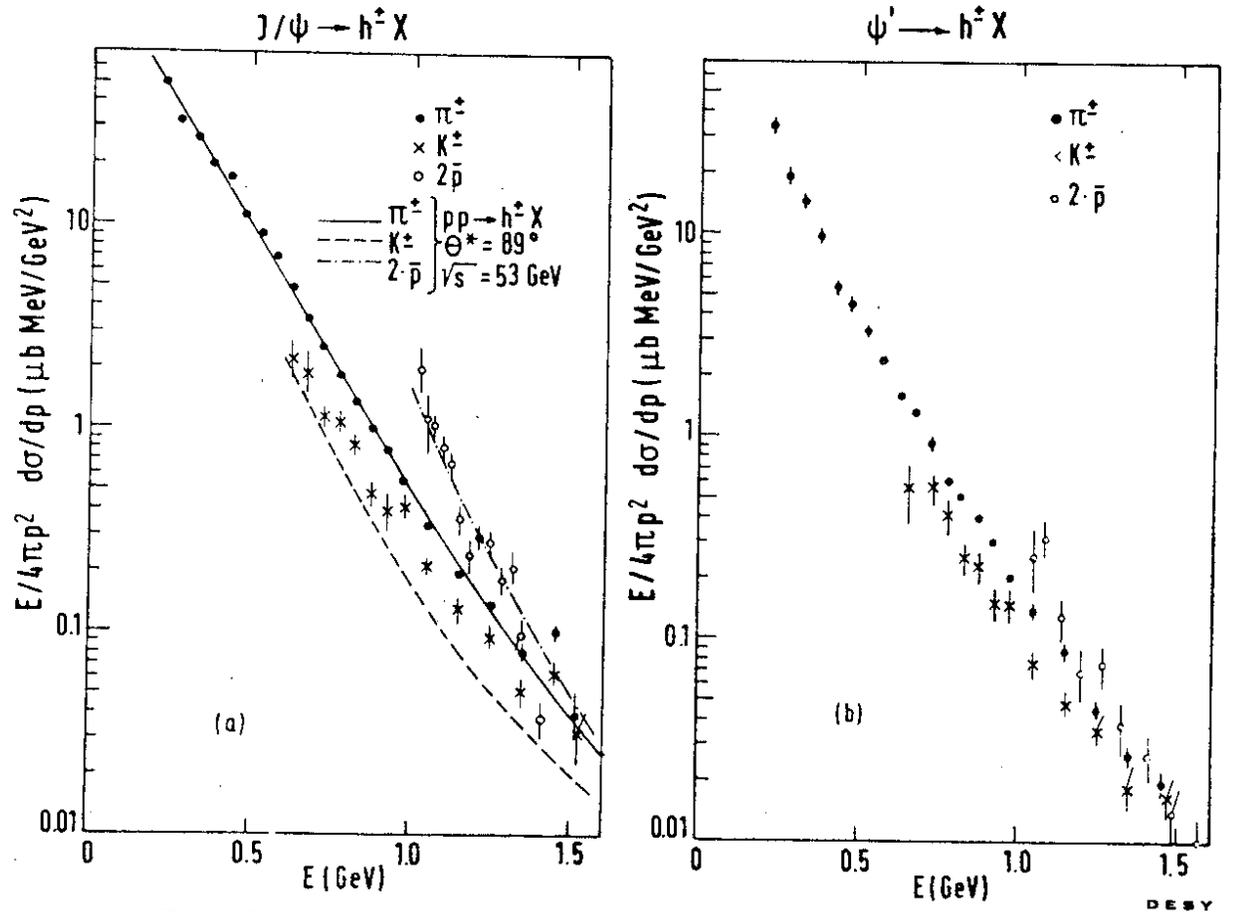

FIG. 3.18 Invariant cross sections as functions of the particle energies. The curves describe the inclusive particle yields from pp → h± X (see Ref.73).

charmonium level scheme

spectroscopic notation $n^{2S+1}L_J$

J^{PC} : $\vec{J} = \vec{S} + \vec{L}$

$P = -(-1)^L$

$C = (-1)^{L+S}$

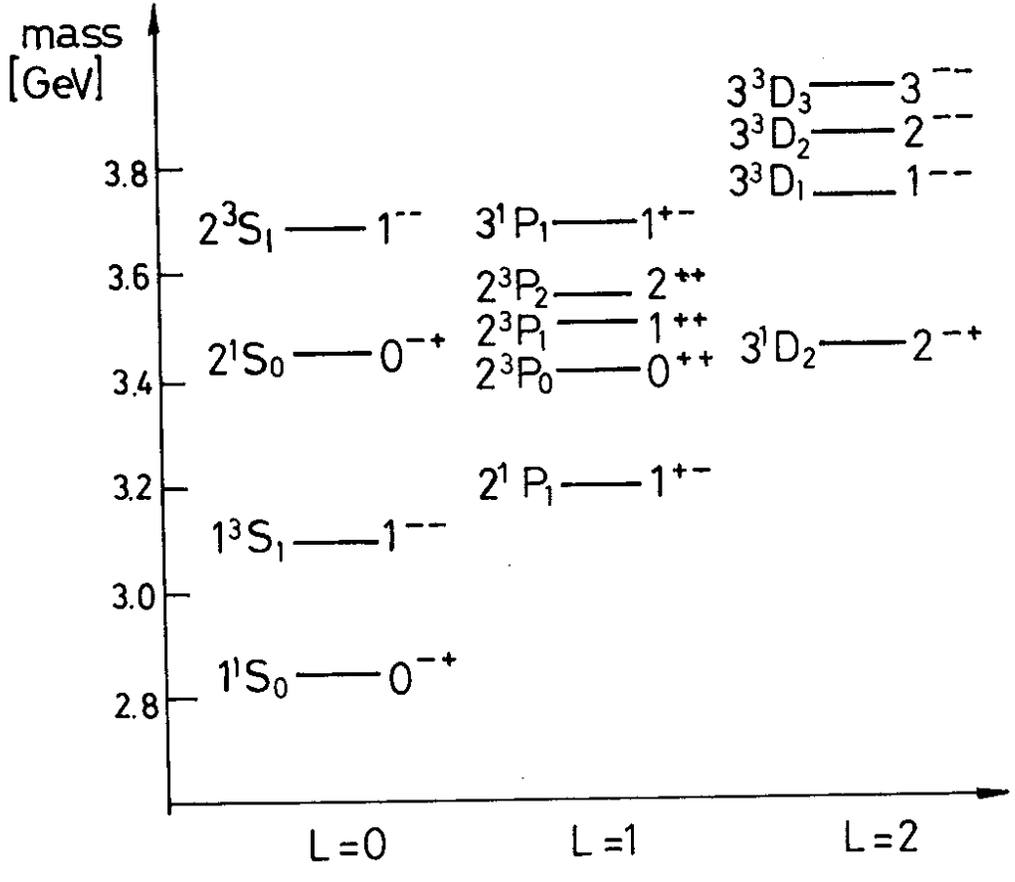

FIG. 3.20 Charmonium level scheme.

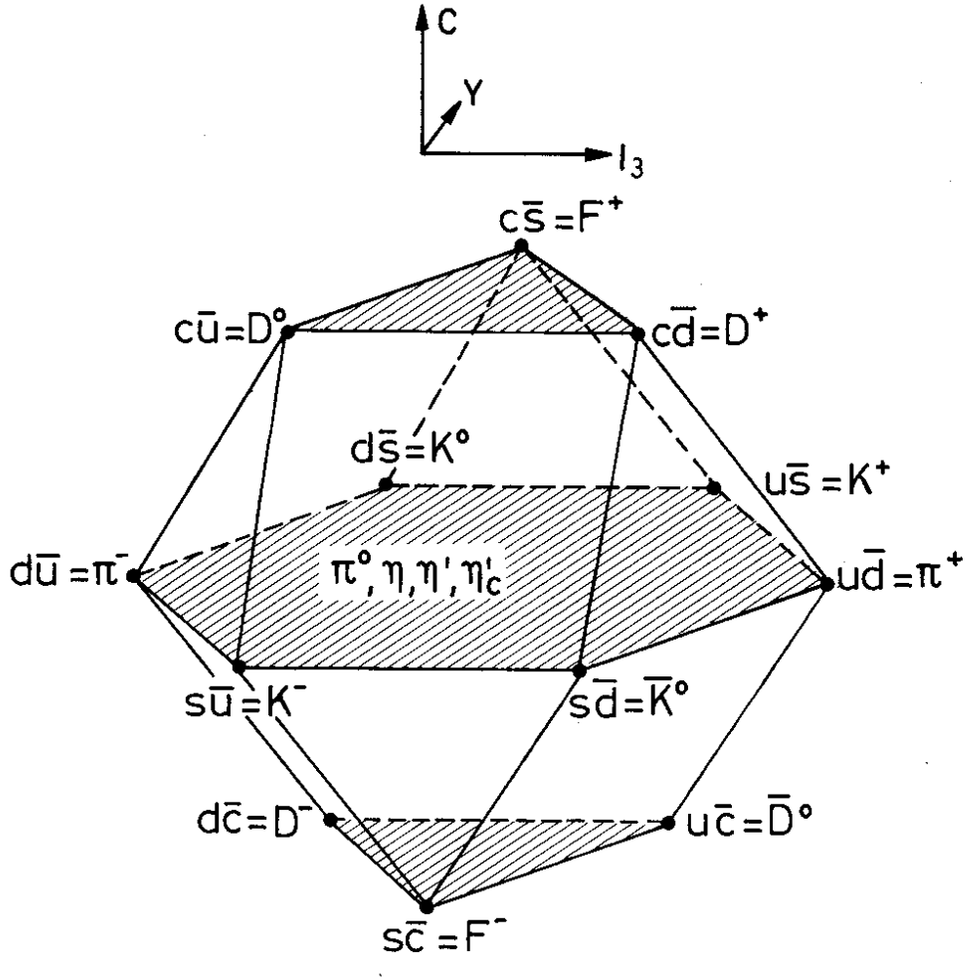

FIG. 3.21 SU(4) multiplet of the pseudoscalar mesons (see Ref.82).

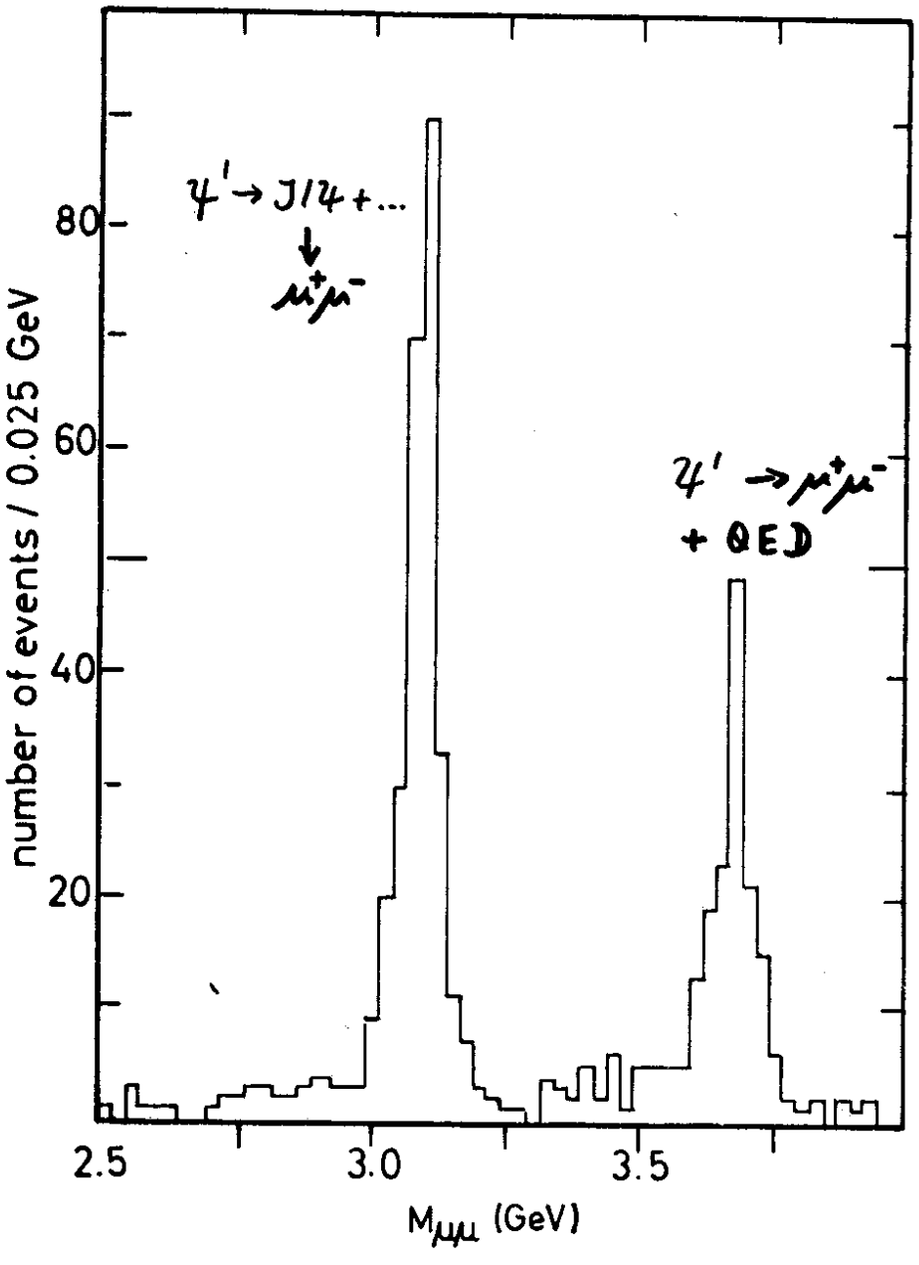

FIG. 3.22 Invariant mass of μ pairs observed in decays of the ψ'.

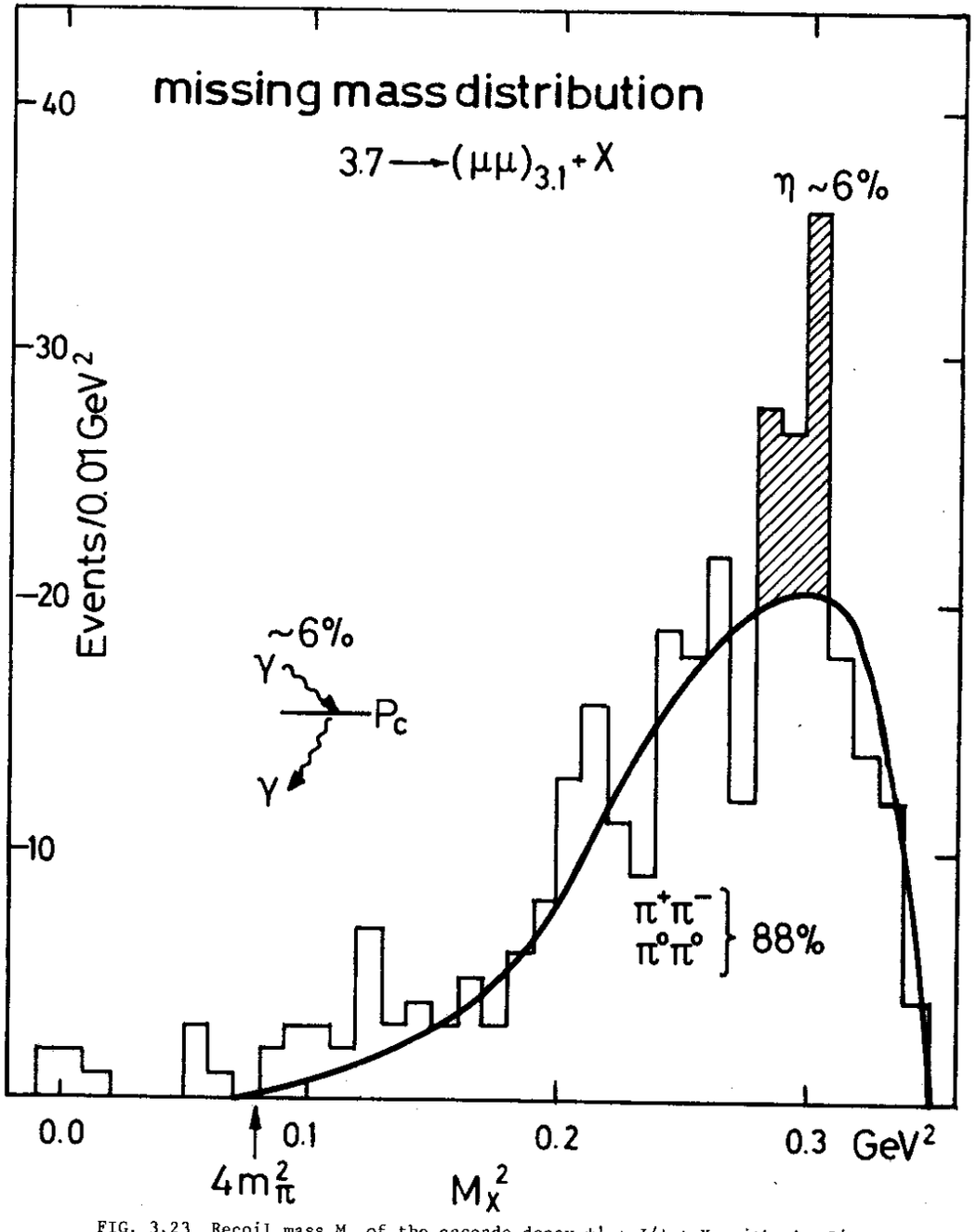

FIG. 3.23 Recoil mass M_x of the cascade decay $\psi' \to J/\psi + X$, with the J/ψ identified by its μ pair decay. The curve represents the spectrum for the $\mu^+\mu^-\pi\pi$ final state.

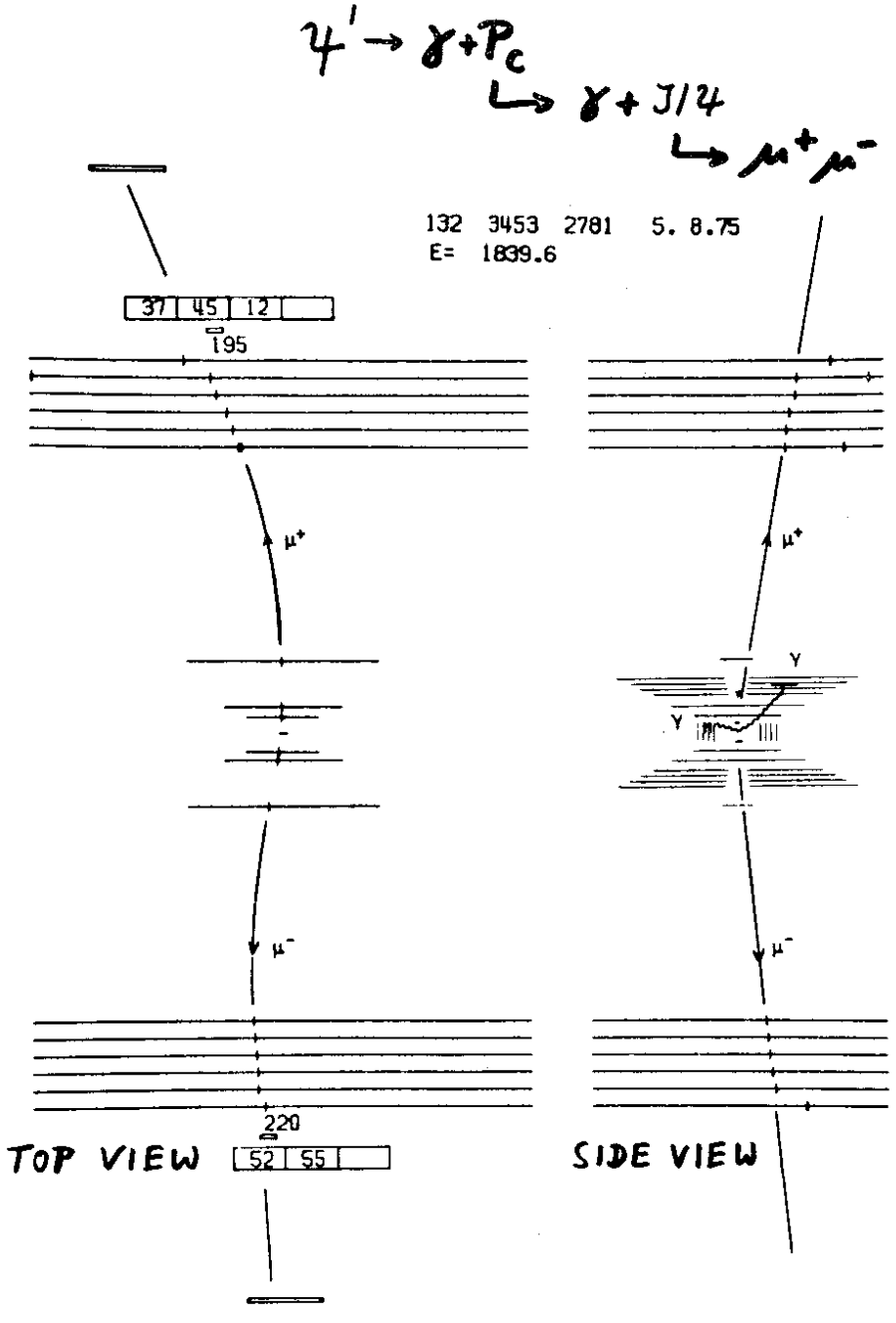

FIG. 3.24 Graphic display of a cascade decay event registered by DASP. The parallel lines are wire chambers and the boxes scintillation counters.

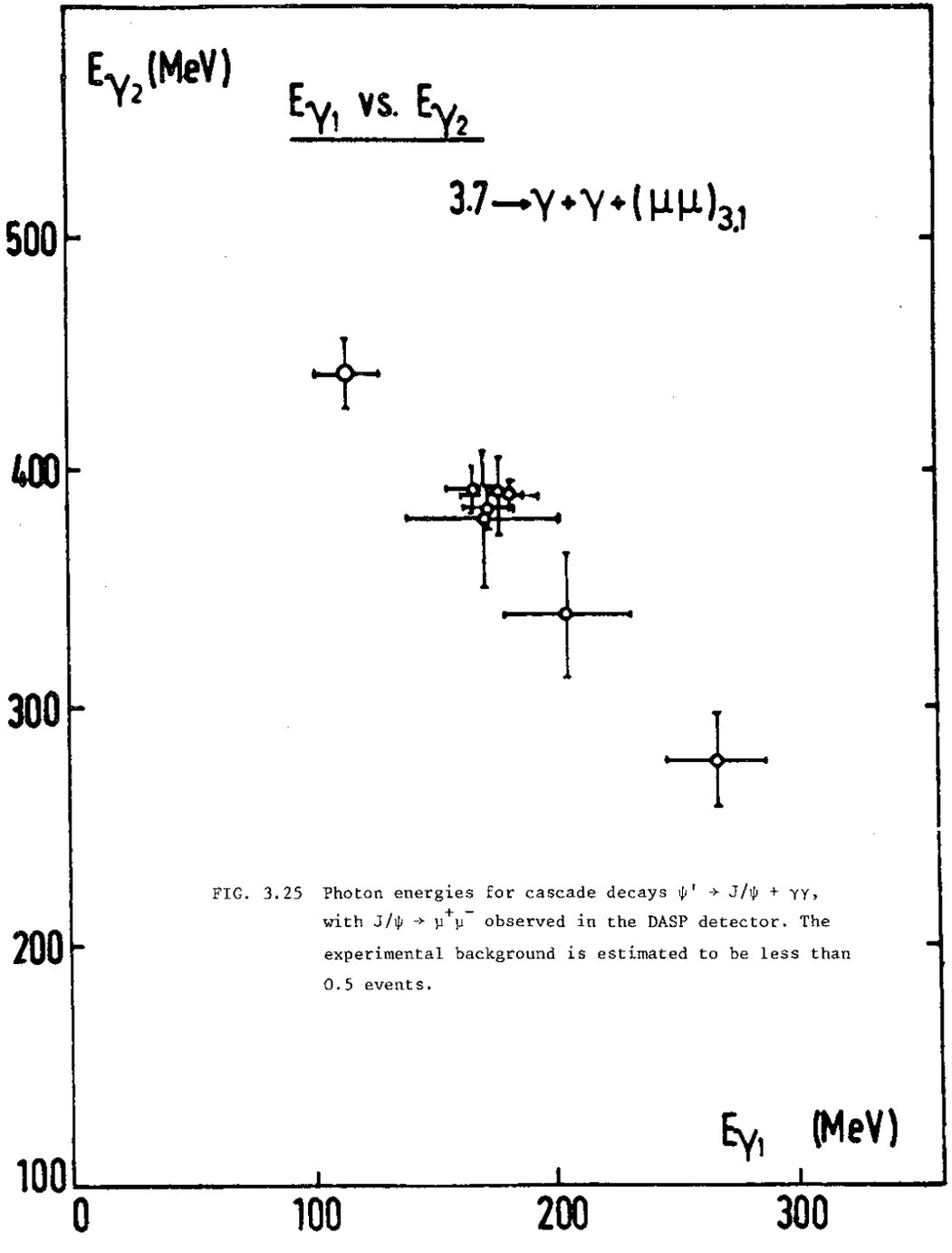

FIG. 3.25 Photon energies for cascade decays $\psi' \to J/\psi + \gamma\gamma$, with $J/\psi \to \mu^+\mu^-$ observed in the DASP detector. The experimental background is estimated to be less than 0.5 events.

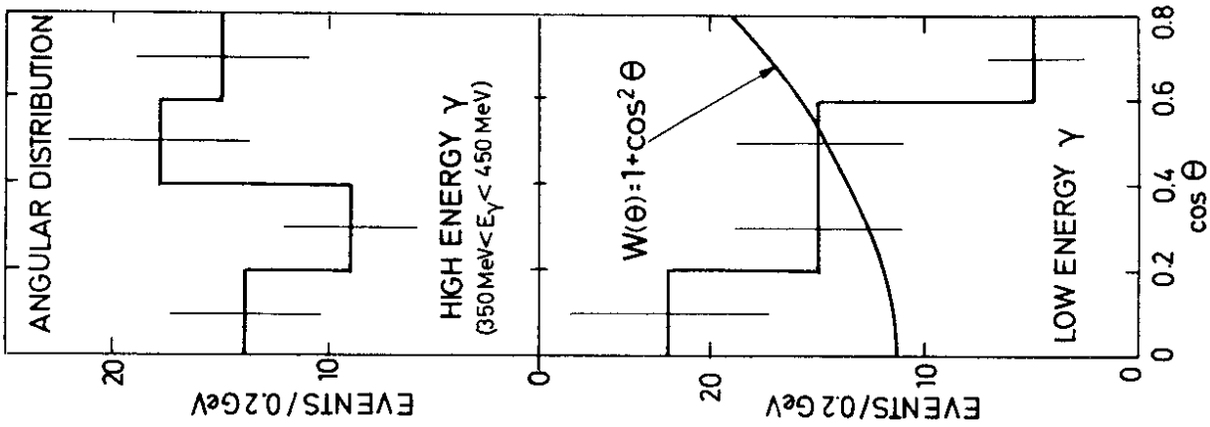

FIG. 3.27 Angular distributions of high and low energy photons for event selected by the shaded area in Fig. 3.26.

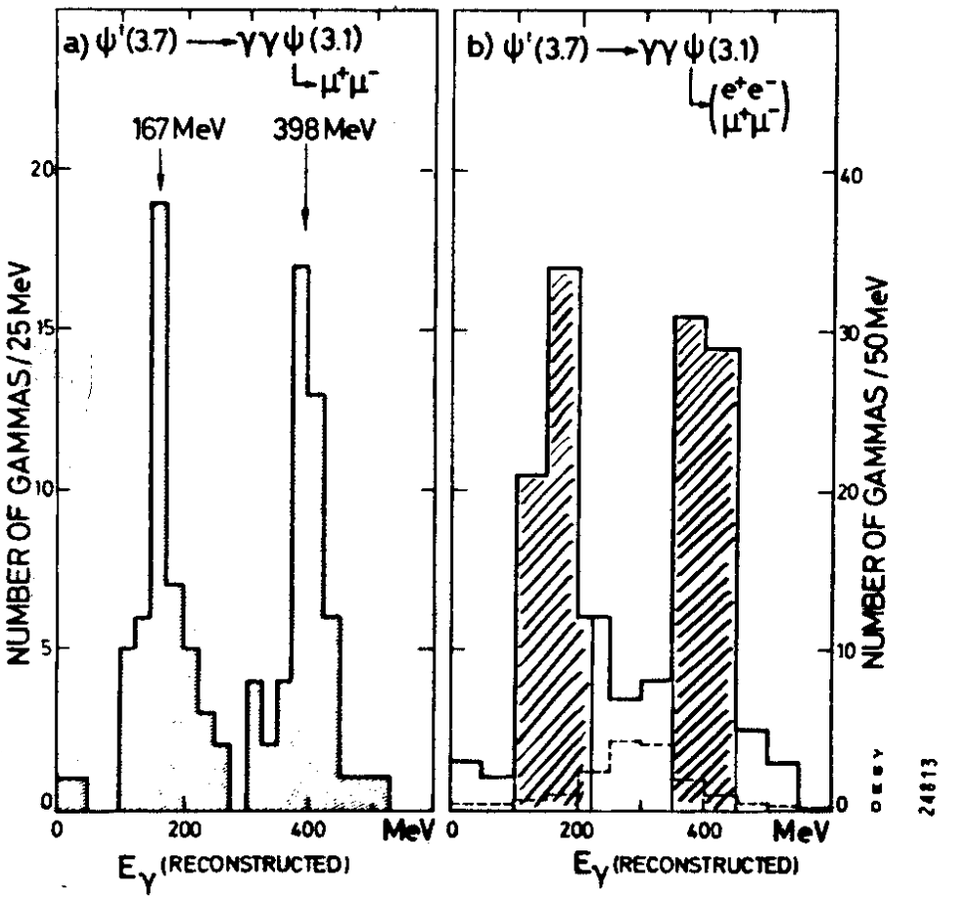

FIG. 3.26 Photon energy spectra of cascade decays. observed in the DESY-Heidelberg detector.

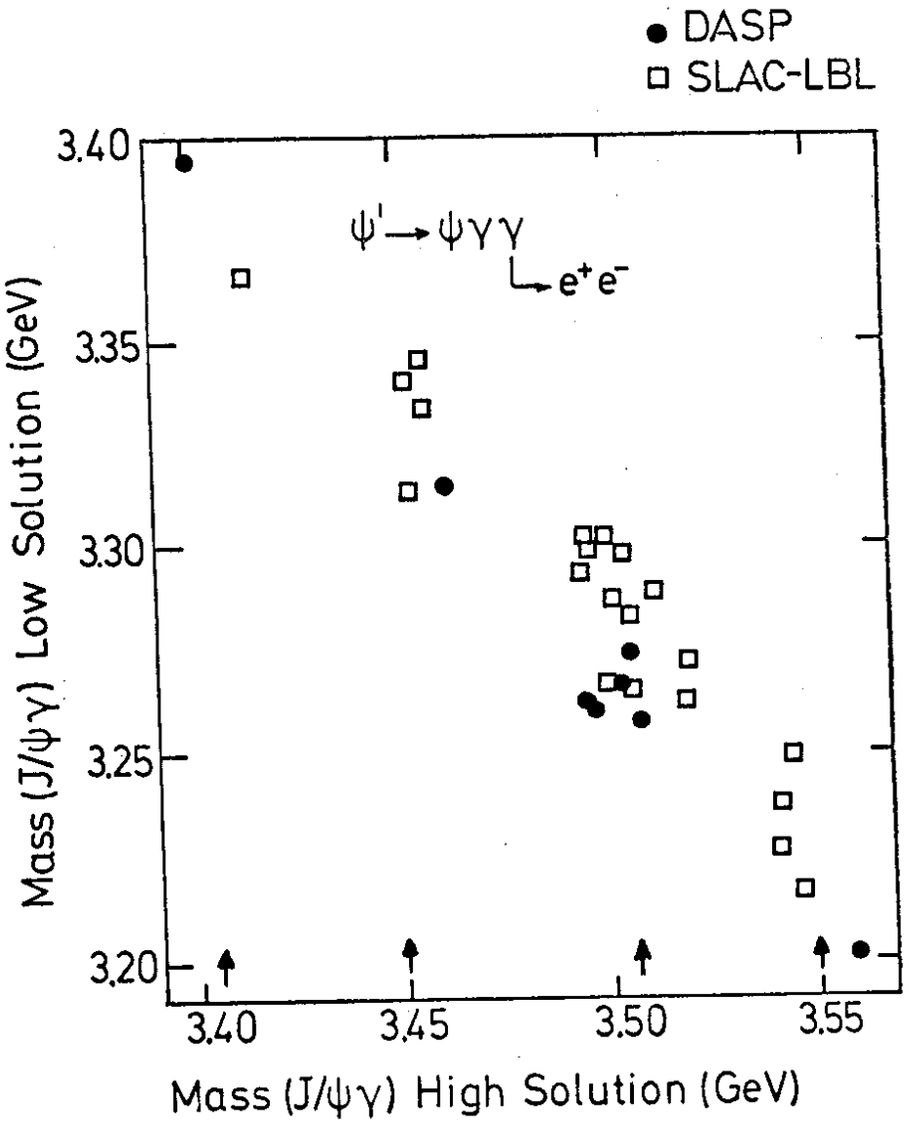

FIG. 3.28 High versus low $J/\psi\gamma$ mass. For the SLAC-LBL points see Ref.51.

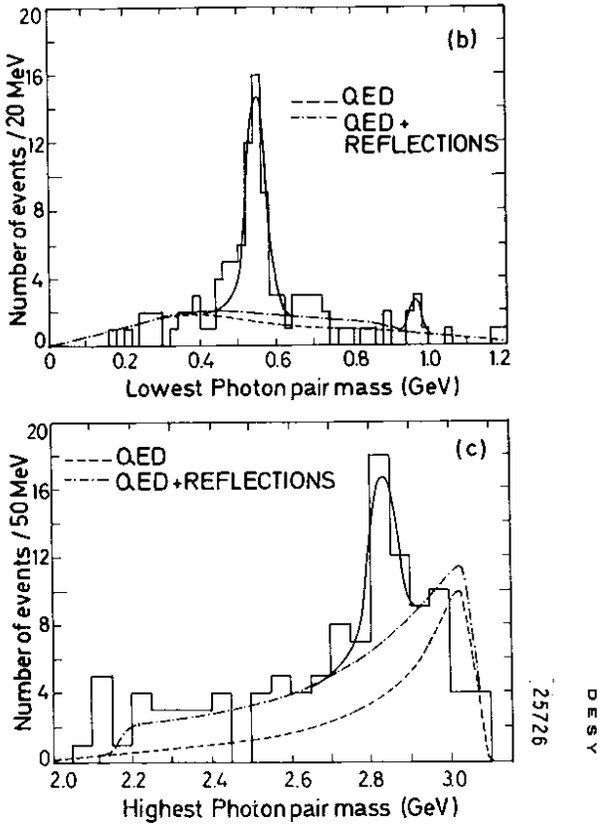

FIG. 3.29 Invariant two photon masses from the decay $J/\psi \to \gamma\gamma\gamma$. Only two combinations are independent, and the lowest and highest masses are plotted. The curves show contributions from the QED process and reflections from resonances in the respective other mass combination.

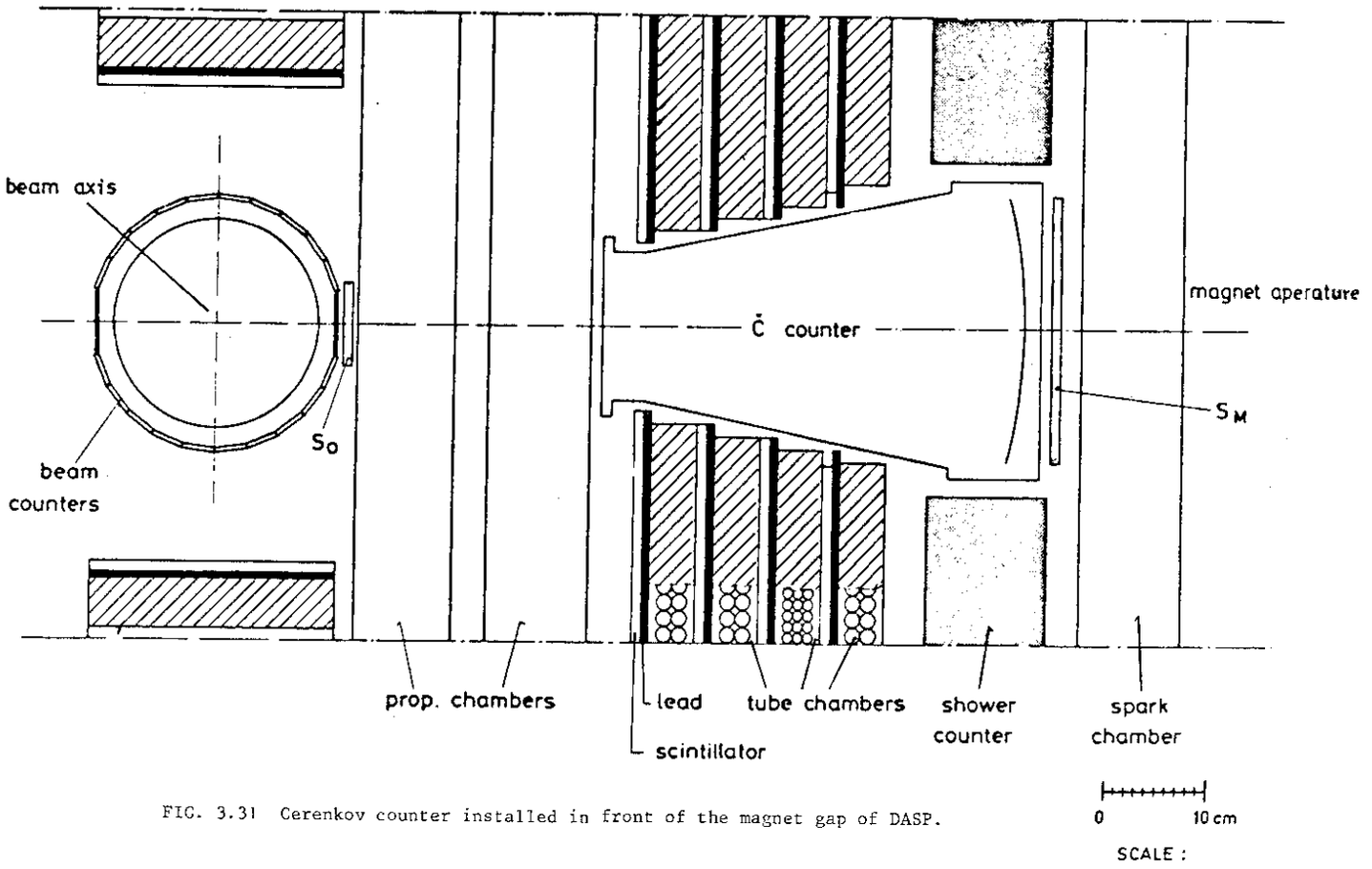

FIG. 3.31 Cerenkov counter installed in front of the magnet gap of DASP.

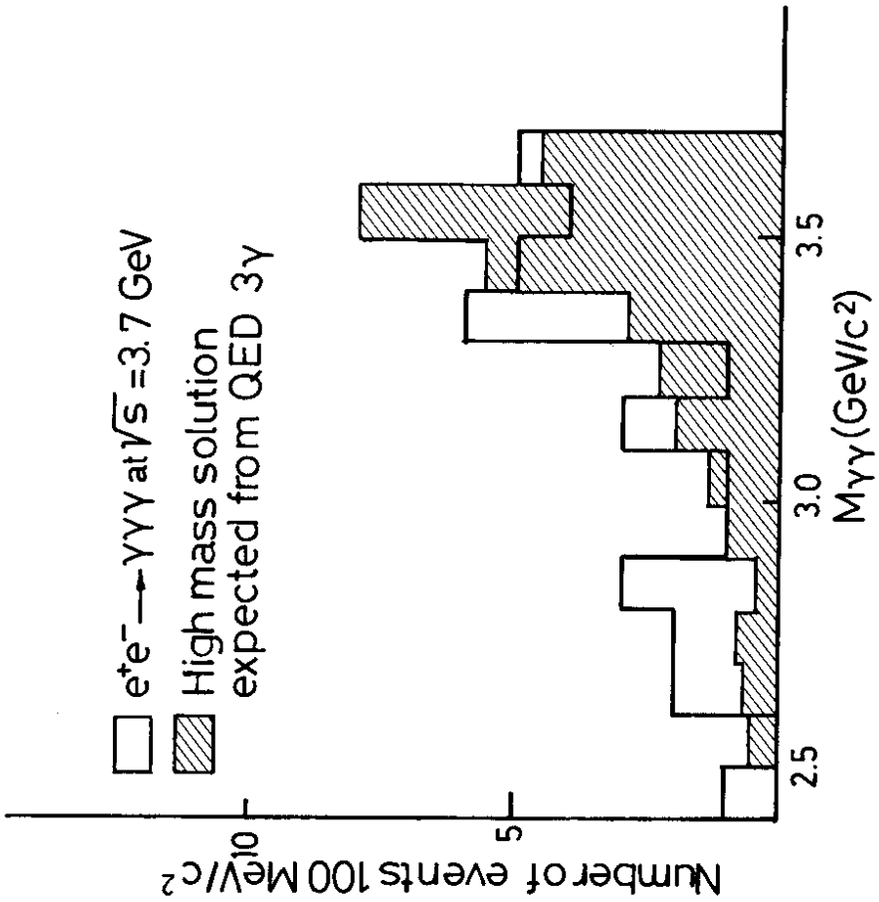

FIG. 3.30 Highest two photon mass for three photon final states at the ψ'. The shaded area shows the expected QED contribution.

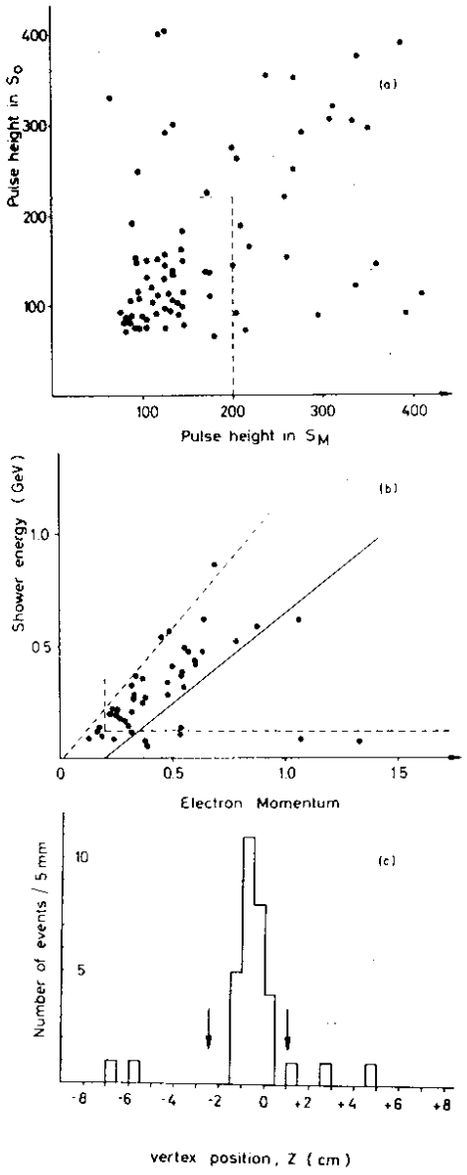

FIG. 3.32 Inclusive electron events observed in the DASP detector:

a) Scatter plot of scintillator pulse heights in front and in back of the Cerenkov counter (see Fig.3.31).

b) Shower counter pulse height versus electron momentum.

c) Distribution of events along the beam axis. Arrows show the limits of the acceptable region.

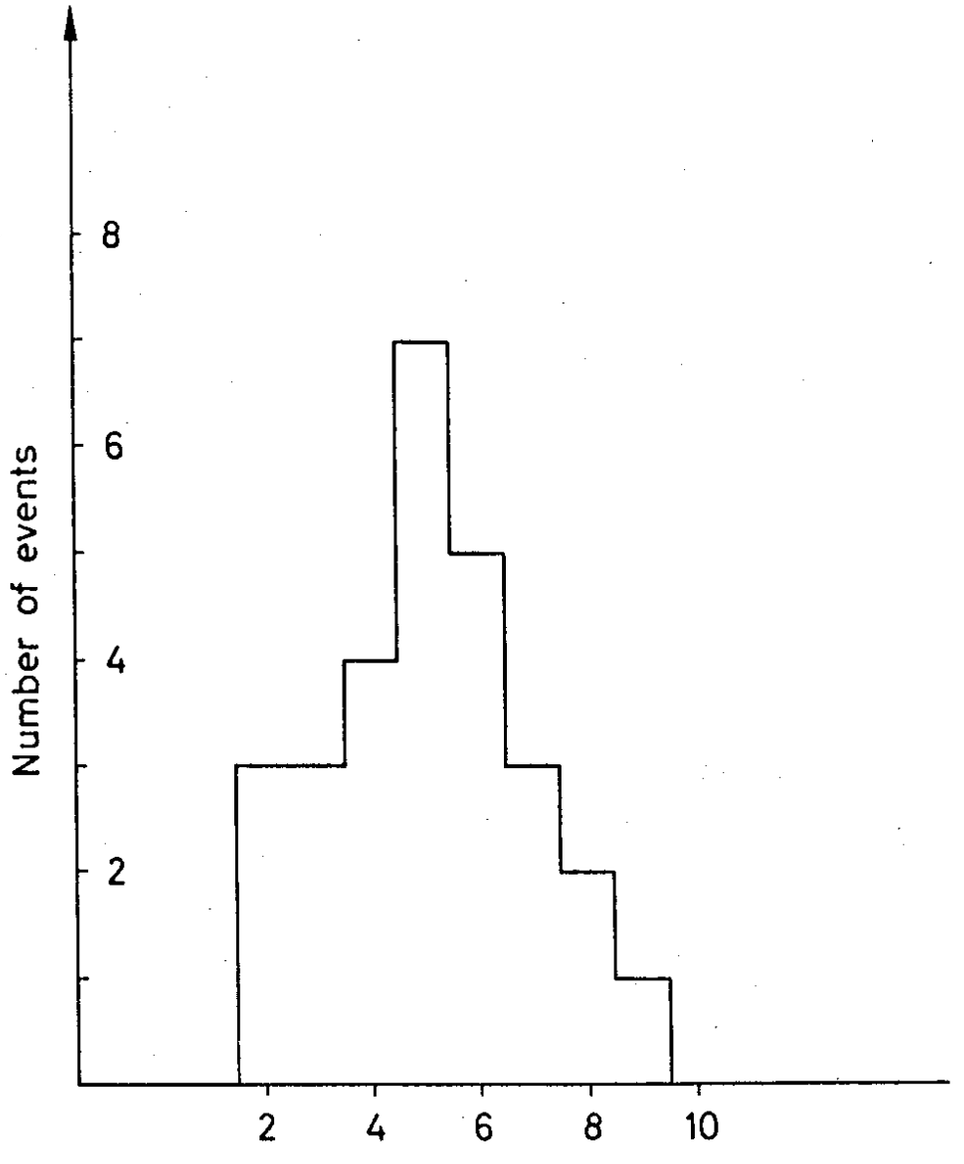

FIG. 3.33 Number of observed charged and neutral tracks for inclusive electron events.

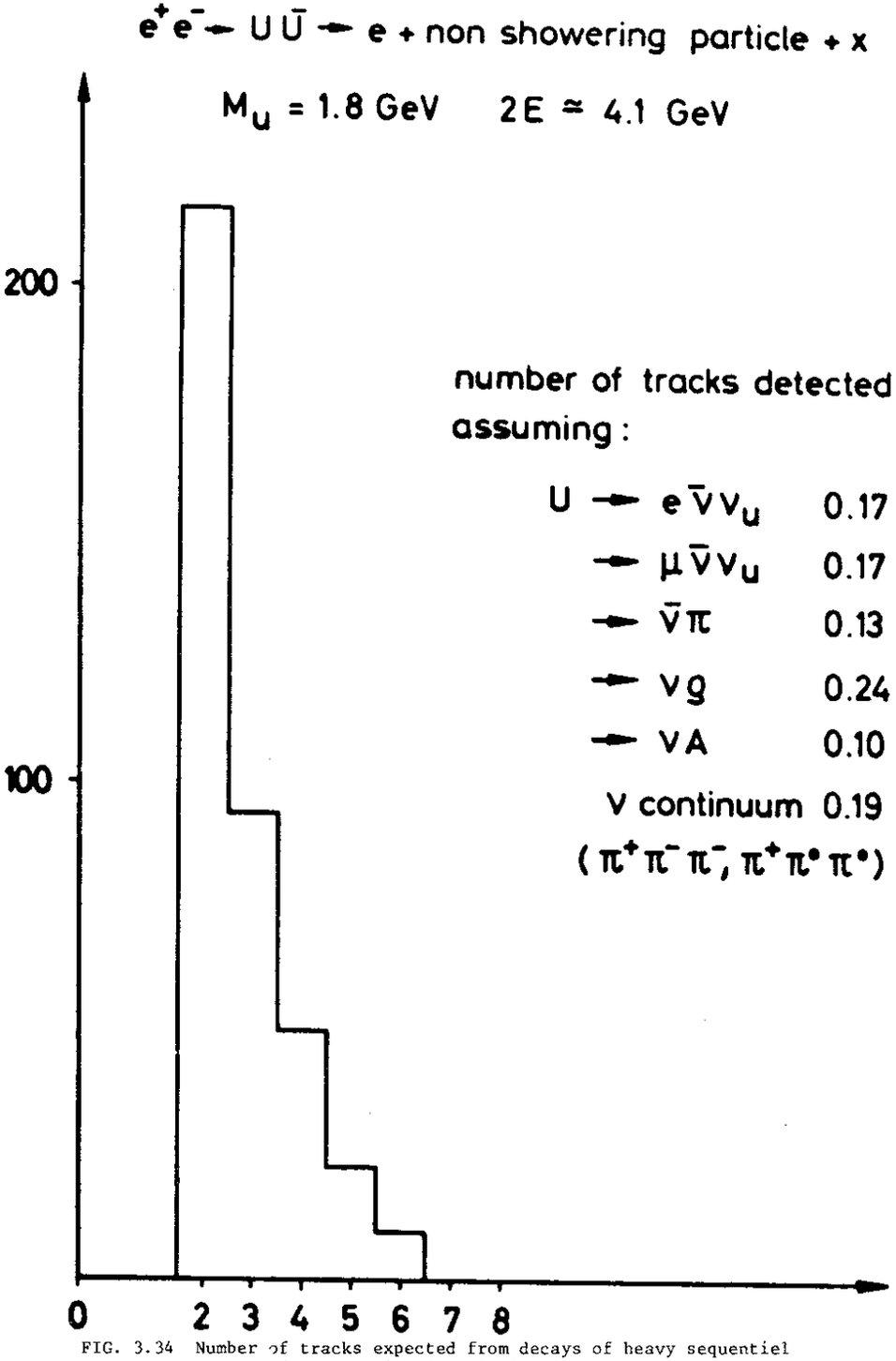

FIG. 3.34 Number of tracks expected from decays of heavy sequentiel leptons (compare with Fig. 3.33).

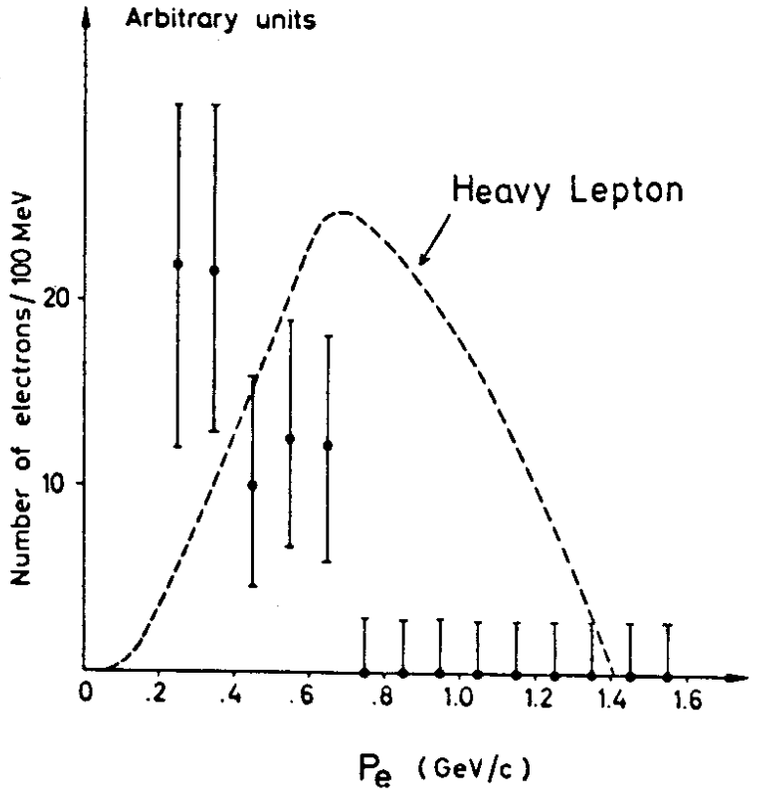

FIG. 3.35 Momentum distribution of inclusive electron events with at least four tracks. The curve was calculated for the decay of leptons of mass 1.9 GeV (see Ref.93).

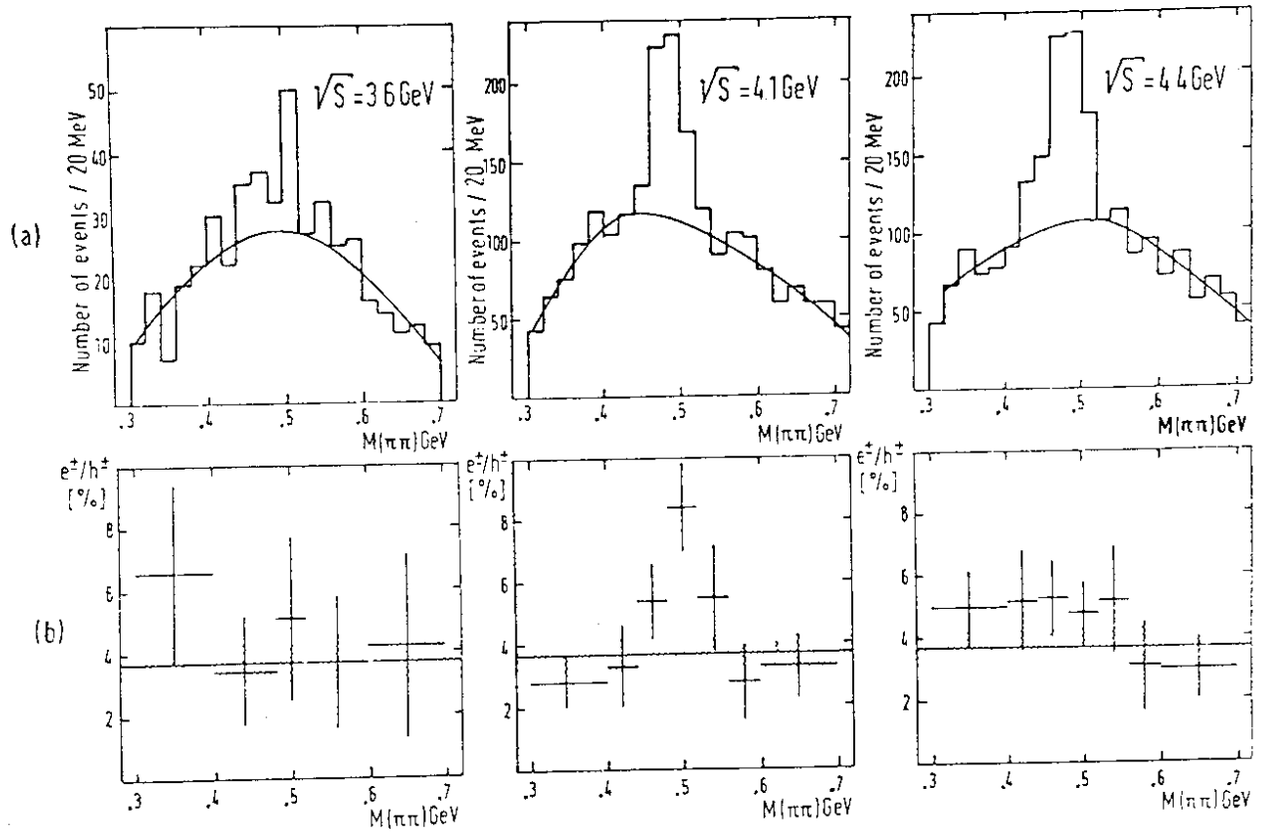

FIG. 3.37 a) Invariant mass of two charged tracks from a common vertex at a minimum distance from the interaction point (PLUTO). K^0 signal on top of a hand-drawn background (curve).

b) Events with an electron in coincidence with K^0's. The straight line is the expected background.

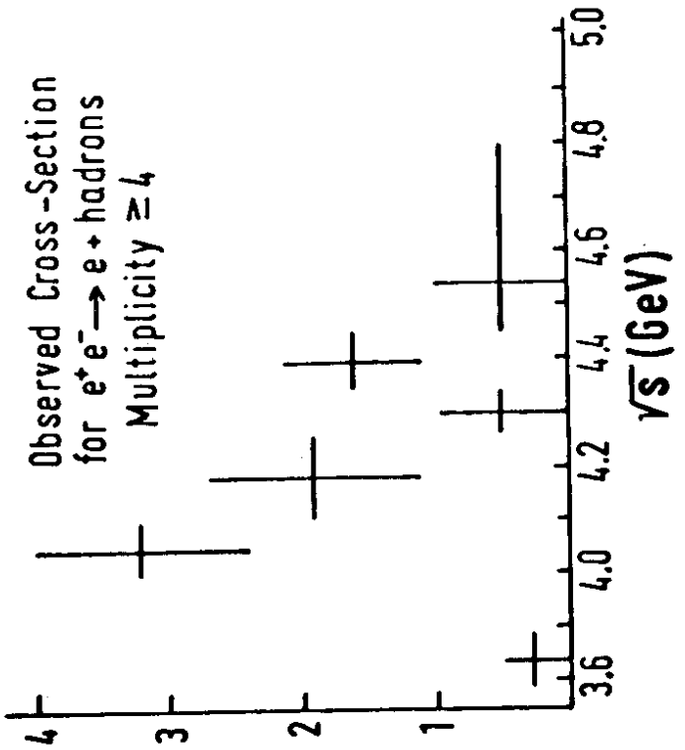

FIG. 3.36 Observed cross section for inclusive electron data in arbitrary units.

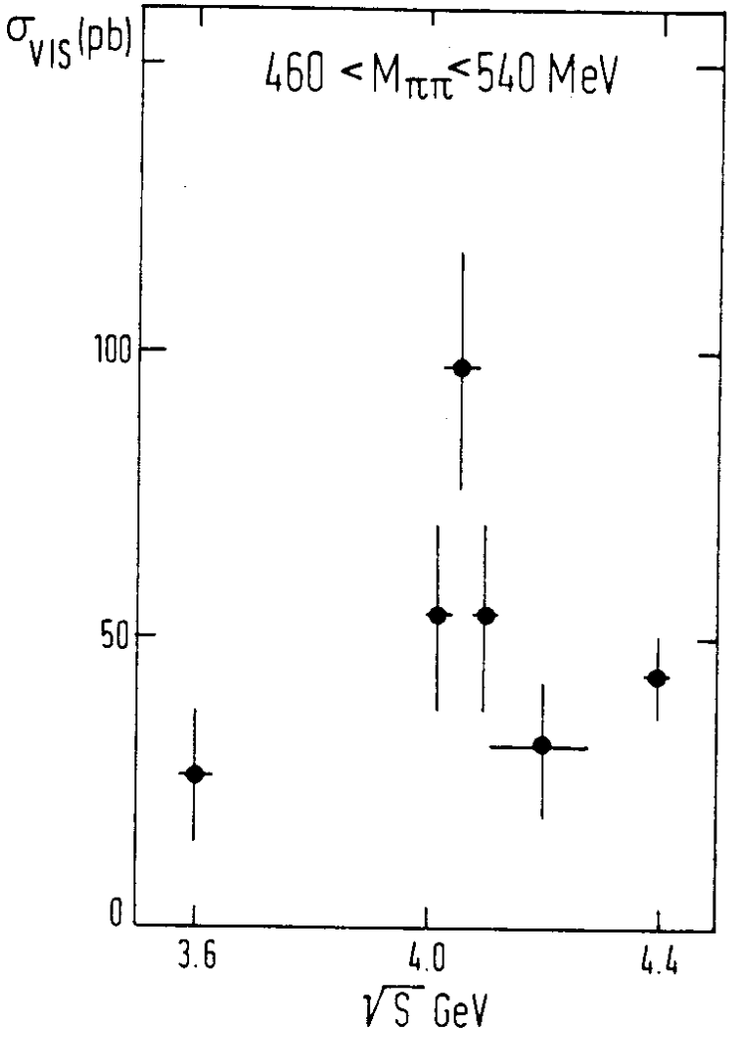

FIG. 3.38 Visible cross section for $e^+e^- \to e^{\pm}K^0_s$ + anything.

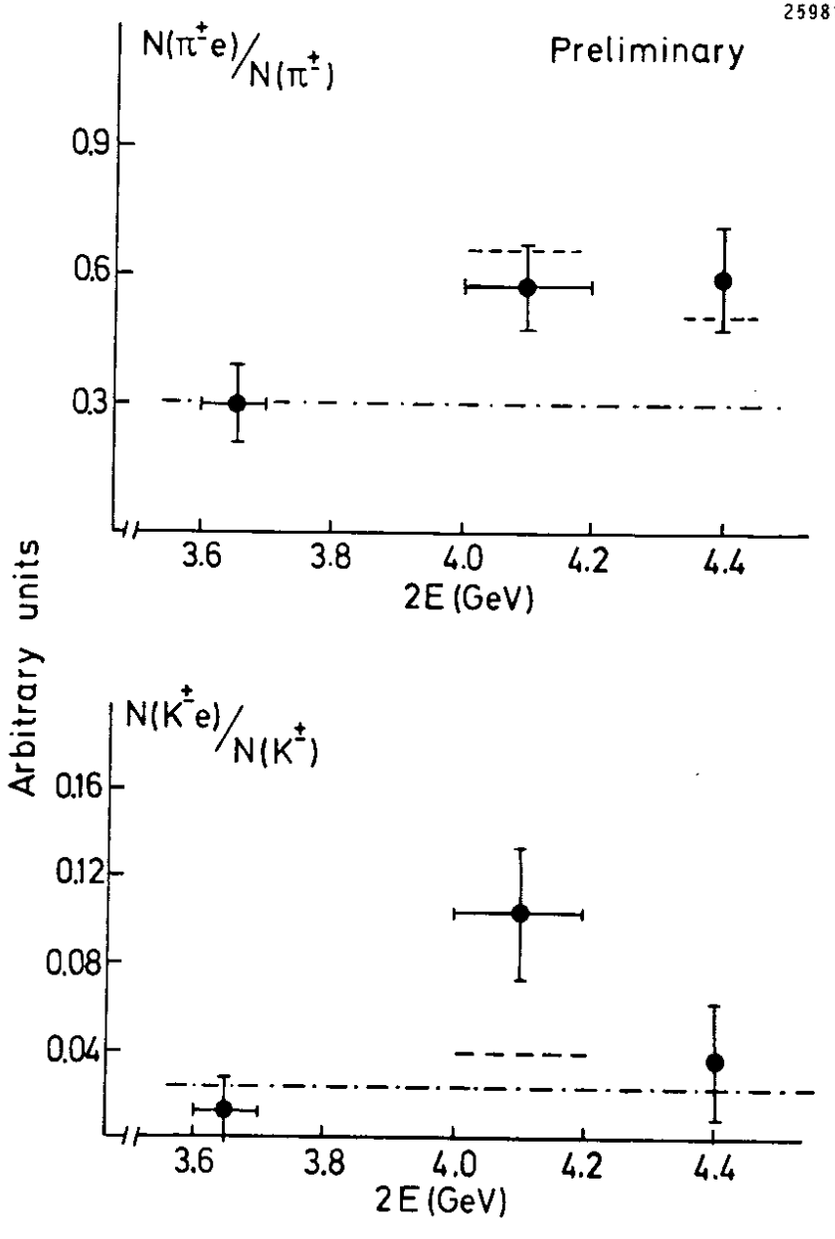

FIG. 3.39 π and K inclusive events (DASP) with an additional electron observed in the inner detector. The dash-dotted line is the estimated background, and the dashed lines give the expected increase of uncorrelated electron hadron events (see text).

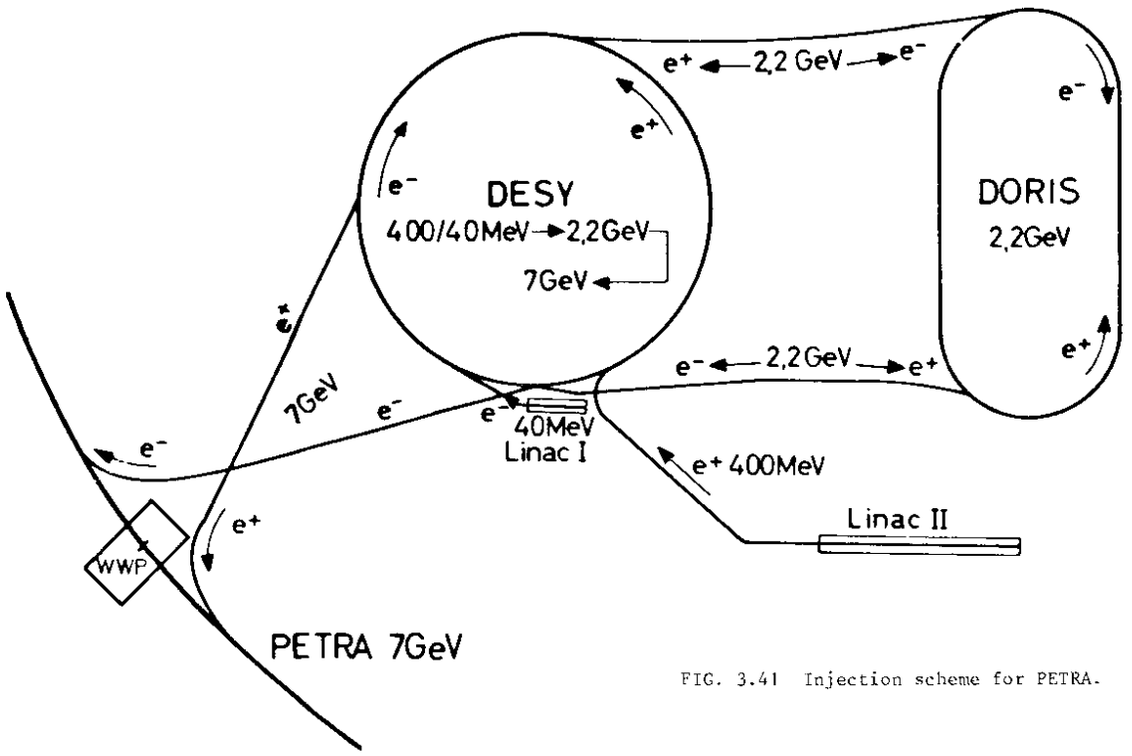

FIG. 3.41 Injection scheme for PETRA.

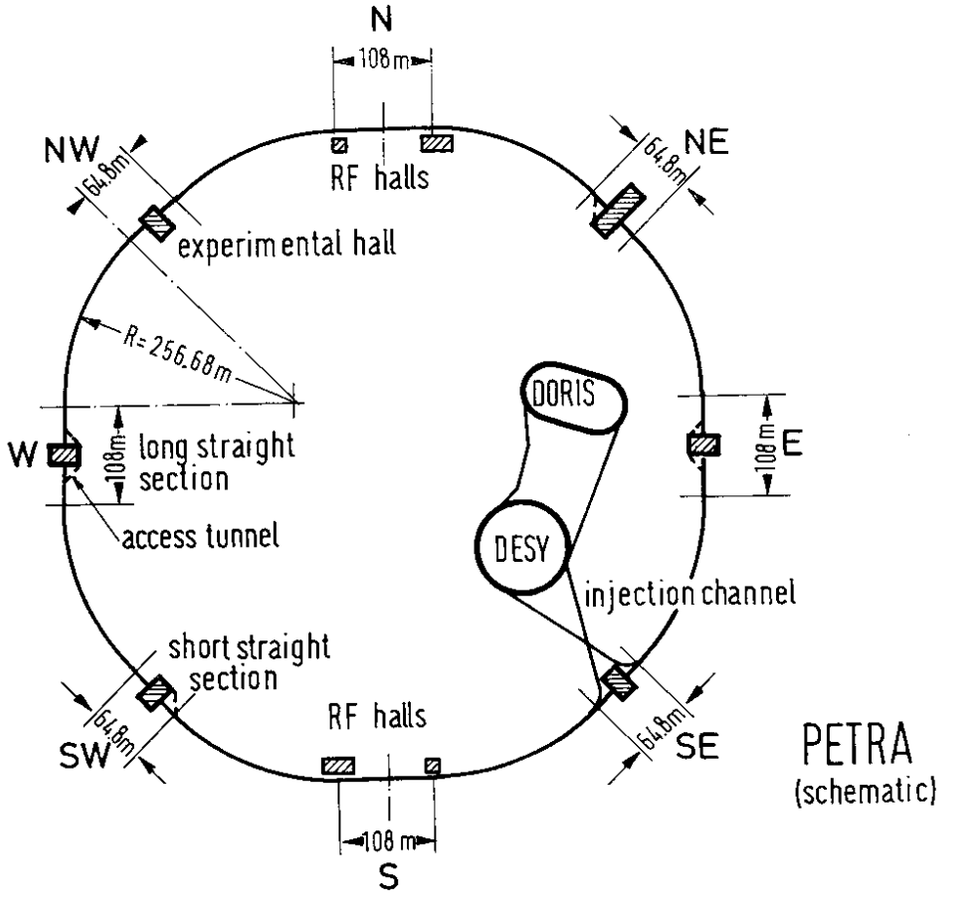

FIG. 3.40 Schematic view of the 2 x 19 GeV storage ring PETRA. On the inside of this new ring, the synchrotron DESY and the 2 x 4.5 GeV storage ring DORIS.

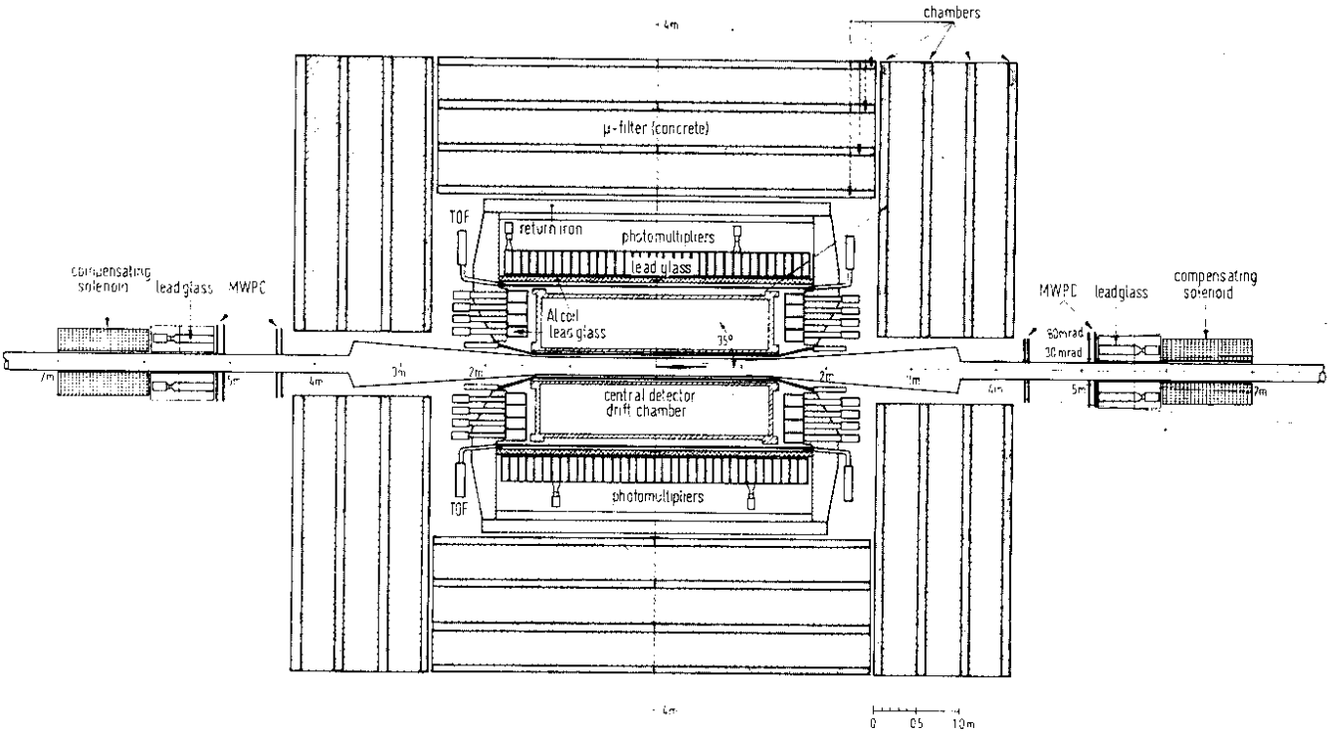

FIG. 3.43 Planned set-up of the JADE Collaboration.

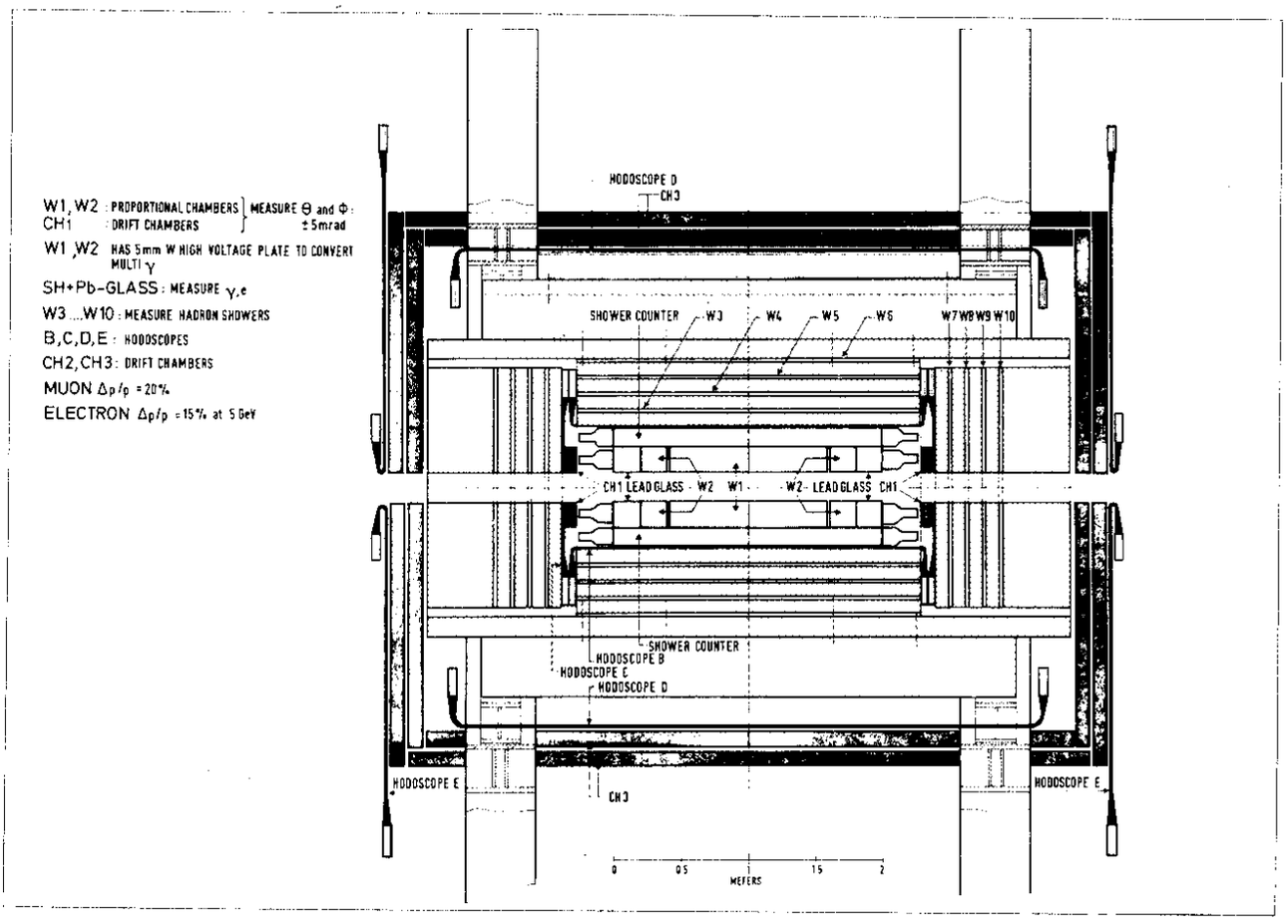

FIG. 3.42 Planned set-up of the MARK J Collaboration.

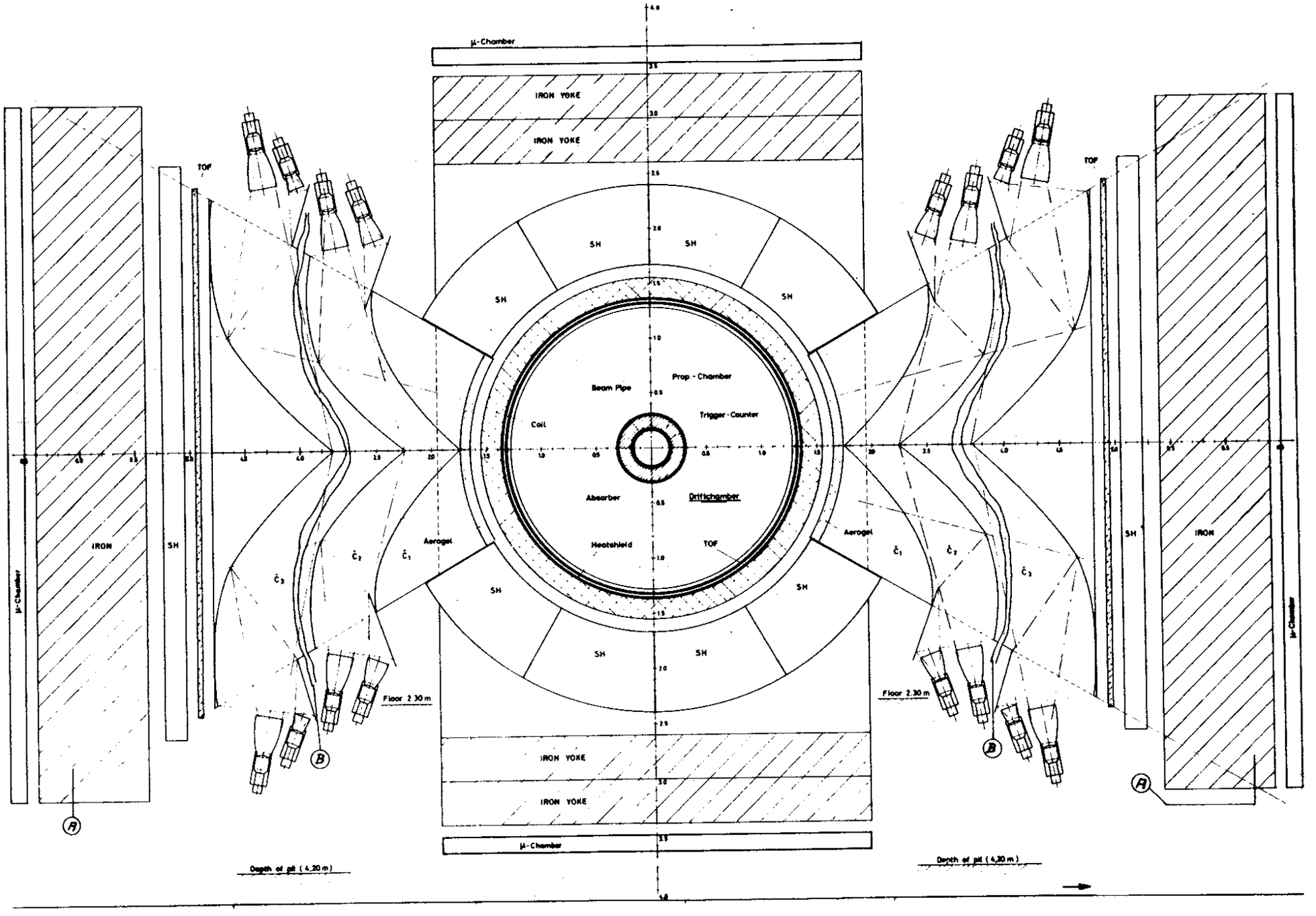

FIG. 3.44 Planned set-up of the TASSO Collaboration.